UNIVERSITY OF CALIFORNIA
IRVINE

Two Photon Decay Widths of Charmonium Resonances Formed in Proton-Antiproton Annihilations

DISSERTATION

submitted in partial satisfaction of the requirements for the degree of

DOCTOR OF PHILOSOPHY

in Physics

by

Michelle Dawn Stancari

Dissertation Comittee:
Professor Jonas Schultz, co-Chair
Professor Mark A. Mandelkern, co-Chair
Professor Myron Bander

1999

The dissertation of Michelle Dawn Stancari is approved,

and is acceptable in quality and form

for publication on microfilm:

Committee co-Chair

Committee co-Chair

University of California, Irvine

1999

Contents

List of Figures

List of Tables

Acknowledgement

The E835 collaboration is a group of gifted scienists, who are also a joy to work with. All of you have become dear to me as friends as well as colleages. In particular, I would like to give a special thanks to Rosanna Cester and Stephen Pordes for their leadership and commitment to the experiment, and especially for their concern for the students.

To my advisors, Professor Jonas Schultz and Professor Mark Mandelkern, I want to say a huge thank you. I cannot imagine two better professors to work with. I appreciate your wisdom, knowledge and guidance almost as much as your compassion and friendship. I have learned so much these last six years. Thank you for the wonderful opportunity.

To George Zioulas, you have been a supportive friend and a great teacher, with the added gift of knowing which role is needed at any given time. Thanks.

To Keith Gollwitzer, I am FINALLY done, and I owe much of it to your help. You have sacrificed much of your personal time to make E835 work. Thank you for guidance and friendship.

To Nadia Pastrone, your smile and energy makes the trailers a different place. You have helped me so many times with questions and numbers, and always with joy. Your hospitality and friendship are so special.

To Todd Pedlar, we actually made it! I have enjoyed working with you tremendously, and your encouragement helped me through some tough things. Thanks for the listening ears.

To Wander Baldini, our supplier of parmigiano reggiano and other Italian goodies, and one of the sweetest people I know, thanks for being such a good friend. I hope that you did not suffer too many cavities watching Giulio and I fall in love.

To the Ferrara group, who has adopted me as their own, you are wonderful. I have really enjoyed getting to know all of you.

To everyone I missed in this list . . . many apologies and thanks.

To my family, your support is unfailing. You are among the few people who see me as a person first and a physicist tenth. For this, I will always be grateful and needful. Much of this thesis belongs to you.

Most importantly, to my husband Giulio, who has stood by me through the writing of this thesis, and countless other things, thank you. Your have put up with mood swings, a dusty house, and dinner alone with the dudes more times that I can remember. You continue to give me encouragement daily, and remind me what is important and what is not. I hope to learn from your example. You are infinately precious to me.

Curriculum Vitae

1993	B.S. in Mathematics University of California, Irvine
1994–1995	Teaching Assistant, Department of Physics, University of California, Irvine
1995–1999	Research Assistant, Department of Physics, University of California, Irvine
1999	Ph.D. in Physics, University of California, Irvine Dissertation: Two Photon Decay Widths of Charmonium Resonances produced in $\overline{p}p$ Annihilations Professor Jonas Schultz, co-Chair Professor Mark Mandelkern, co-Chair

Publications

M. Ambrogiani et al., Measurements of the magnetic form factor of the proton in the timelike region at large momentum transfer, Phys. Rev. D60, 032002 (1999).

M. Ambrogiani et al., Study of the χ_{c0} ($1^3\mathrm{P}_0$) state of charmonium formed in $\overline{p}p$ annihilations, submitted to Phys. Rev. D (1999).

Abstract of the Dissertation

Two Photon Decays Widths of Charmonium Resonances Formed in Proton-Antiproton Annihilations

by

Michelle Dawn Stancari

Doctor of Philosophy in Physics

University of California, Irvine, 1999

Professor Jonas Schultz, co-Chair

Professor Mark Mandelkern, co-Chair

E835 is an experiment dedicated to the precision study of charmonium formed in $\overline{p}p$ annihilations at the Fermilab Antiproton Accumulator. E835 has measured the resonance parameters of the η_c resonance: $M(\eta_c) = 2985.4 \pm 2.1$ MeV, $\Gamma(\eta_c) = 21.1 \pm^{7.5}_{6.2}$ MeV, and $\Gamma(\eta_c \to \gamma\gamma) = 3.9 \pm^{1.5}_{1.3} \pm^{1.8}_{1.1}$. Also reported is the two photon width of the χ_2, $\Gamma(\chi_2 \to \gamma\gamma) = 0.29 \pm 0.06 \pm 0.04$. A search for the η_c' resonance has resulted in an upper limit for the product of the branching ratios $B(\eta_c' \to \overline{p}p) \times B(\eta_c' \to \gamma\gamma) < 12 \times 10^{-8}$. An upper limit $\Gamma(\chi_0 \to \gamma\gamma) < 2.7$ keV is set.

Chapter 1

Introduction to Charmonium

In 1970, Glashow, Iliopoulos and Maiani[51] proposed the existence of a fourth quark to explain the suppression of strangeness-changing neutral currents in weak interactions using the quantum number of charm, which was first proposed by Bjorken and Glashow in 1964[34]. At the same time, the theory of QCD, based upon the color SU_3 gauge group, was being developed to describe hadron interactions and dynamics. This theory incorporated many new and untested ideas. The new, and completely hidden, quantum property of color required three versions of each quark. The coupling constant, α_s, changed with distance, to accommodate the new concepts of quark confinement and asymptotic freedom, introduced to explain the absence of free quarks at low energies and the increasing weakness of the quark coupling at higher energies respectively. Theorists were eagerly seeking the physical manifestations of these ideas that would validate QCD.

In November 1974, a narrow resonance was discovered simultaneously in e^+e^- collisions at SLAC[20] and $pBe \rightarrow e^+e^- + X$ interactions at Brookhaven[19]. Figure 1.1 shows the enhanced e^+e^- signal from both experiments. A second narrow resonance was quickly found near the first. At the time, Thomas Applequist and David Politzer were theoretically investigating the binding of a charmed and an anticharmed quark.

Figure 1.1: Initial evidence for the J/ψ. (a) $pBe \to e^+e^- + X$ interactions at Brookhaven[19] and (b) $e^+e^- \to hadrons$ at SLAC.[20]

They found that QCD predicted a series of bound states with very narrow widths, analogous to the e^+e^- bound states known as positronium[11]. The resonances, later named the J/ψ and ψ', were interpreted as bound states of this type and immediately theoretical predictions for the entire $\overline{c}c$ spectrum surfaced, followed by a flurry of experimental work to observe and study the remaining states. E835 is an experiment in Fermilab's Antiproton Accumulator dedicated to precision measurements of these states produced $\overline{p}p$ annihilation.

1.1 Charmonium Spectroscopy

The charmonium spectrum as known today is shown in figure 1.2. The *open charm* threshold at 3.73 GeV is the energy above which the charmed and anticharmed quark have enough energy to separate, create a $\overline{q}q$ pair, and form two charmed mesons as in figure 1.3(a). Below the open charm threshold however, the quarks are forced to decay to light mesons via annihilation into gluons, figure 1.3(b). The OZI-rule (Okubo, Zweig, and Iizuka)[68] states that this annihilation is suppressed because there are no charmed quarks in the final state. Since the dominant decay modes are either suppressed or forbidden, the widths of the $\overline{c}c$ states below the open charm threshold are narrow, 50-100 times narrower than other heavy resonances.[1] With the states well separated in energy, the energy range between the η_c and the open charm threshold is an ideal place for spectroscopic work.

Early experiments formed charmonium states with e^+e^- annihilations, which proceeds through an intermediate photon. The quantum numbers of the charmonium state directly produced are thus limited to $J^{PC} = 1^{--}$ and all other states must be studied through the radiative decays of the 1^{--} states. One advantage is the high yield. With a hadronic background smaller than one percent of the J/ψ and ψ' production rates, the hadronic decays of the J/ψ and ψ' provide a clean signal. Hadronic decays constitute over 80% of the J/ψ width and over 95% of the ψ' width, so precise measurements of the mass and width of the J/ψ and ψ' are easily obtained from the energy of the electron and positron beams. However, the remaining states below the open charm threshold must be studied through the radiative decays of the ψ' and J/ψ, their production rates reduced by the radiative branching ratio. More impor-

[1] Above the $\overline{D}D$ threshold, two narrow states are also expected, since a decay to $\overline{D}D$ is forbidden and the energy needed to produce $\overline{D}D^*$ is not available.

The Charmonium Spectrum

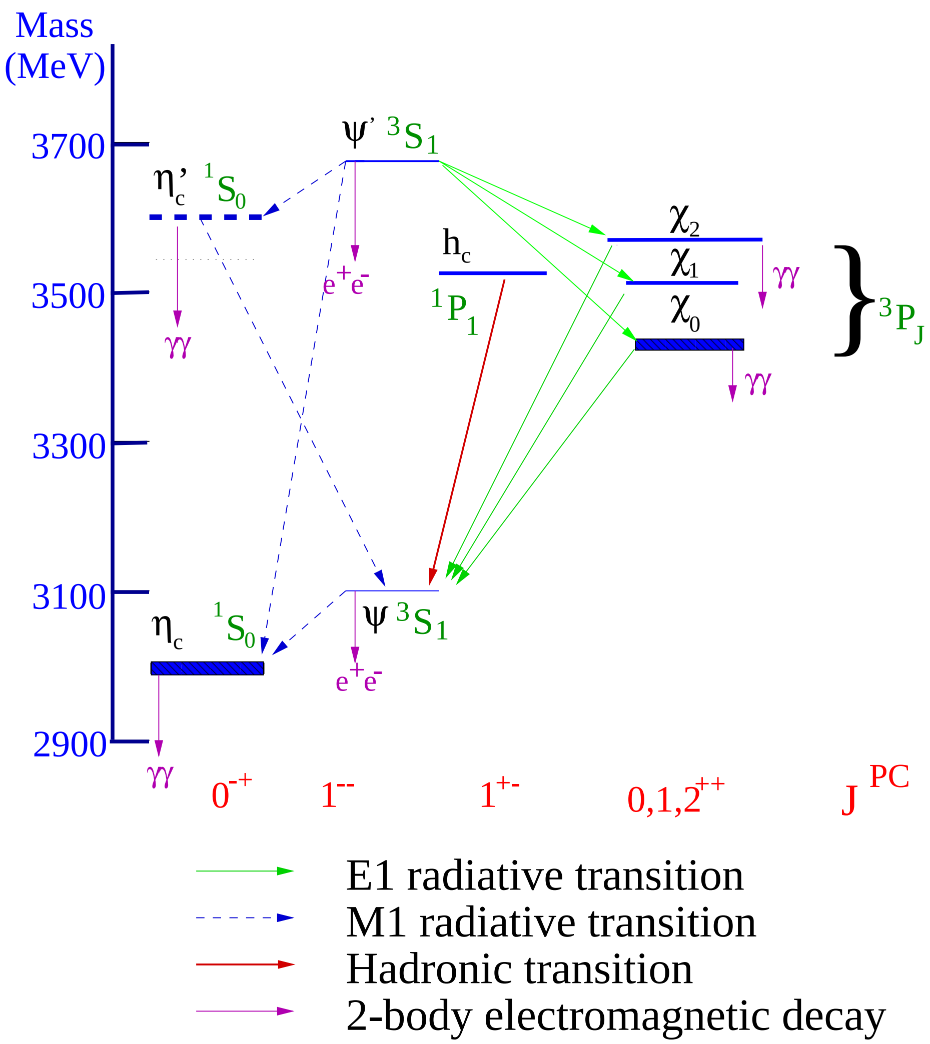

Figure 1.2: The charmonium spectrum. In order to simplify the diagram, only the transitions studied in E760 and E835 are explicitly shown. The horizontal axis is ordered with the notation J^{PC}, and the alternate spectroscopic notation, ${}^{2S+1}L_J$, is displayed next to the resonance name. The thickness of the line marking each state is proportional to the width of the state. The dashed line of the η_c' resonance indicates that the initial measurement has not yet been confirmed.

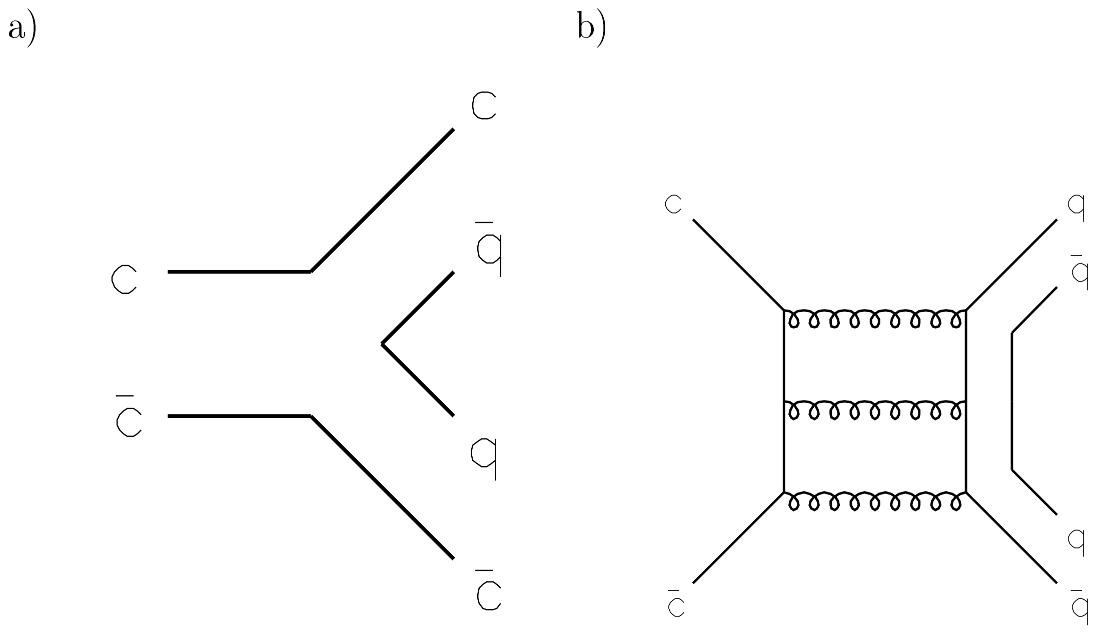

Figure 1.3: An illustration of the OZI-rule, which implies that fragmentation into charmed mesons (a) is preferred and that annihilation through gluons (b) is suppressed.

tantly, the mass and width measurements for the intermediate charmonium states are limited by the detector energy resolution, typically a few percent.

Perhaps the most comprehensive experiment performed at a e^+e^- collider, Crystal Ball[35], measured the inclusive photon spectrum at the ψ' formation energy. Figure 1.4 is the photon spectrum seen by the Crystal Ball detector. The upper insets show the signals, background subtracted, in the η_c and η_c' region. The magnetic dipole (M1) radiative transition rates from the ψ' and J/ψ to these singlet S-wave states are suppressed, resulting in a signal so small that statistical errors dominate even though over 10^6 ψ's were produced. This was the first observation of the η_c, although there had been many false candidates from previous experiments. The signal in the η_c' region is the only experimental evidence for the η_c' resonance to date.

After Crystal Ball's successful run, new measurements became increasingly diffi-

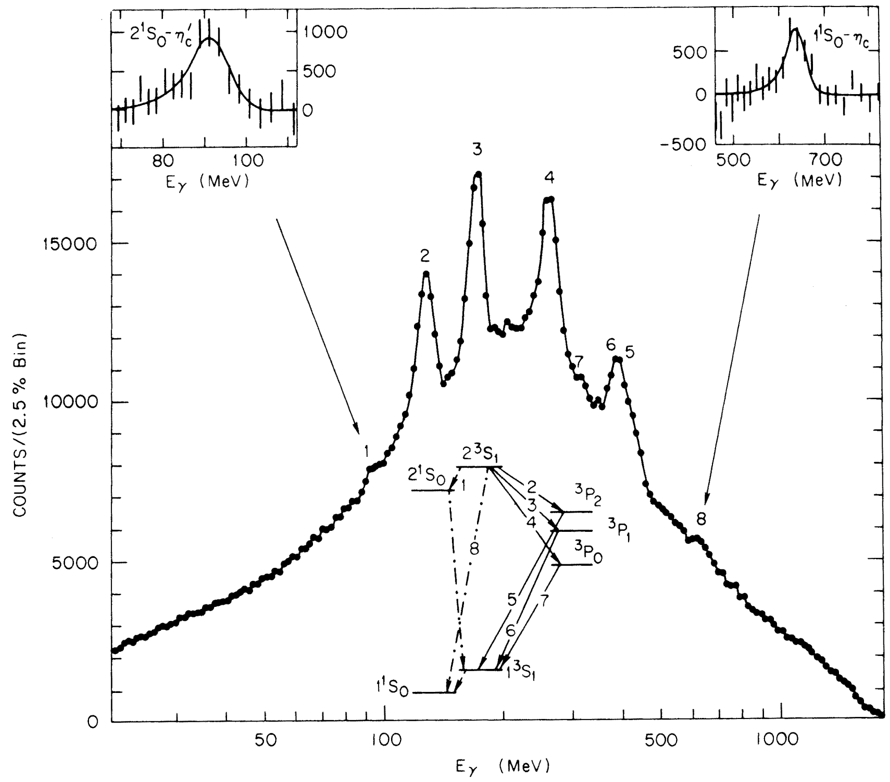

Figure 1.4: The inclusive photon spectrum seen by the Crystal Ball detector. The detector energy resolution is quoted as $\sigma_E = 0.0255E^{0.75}$ in reference [35].

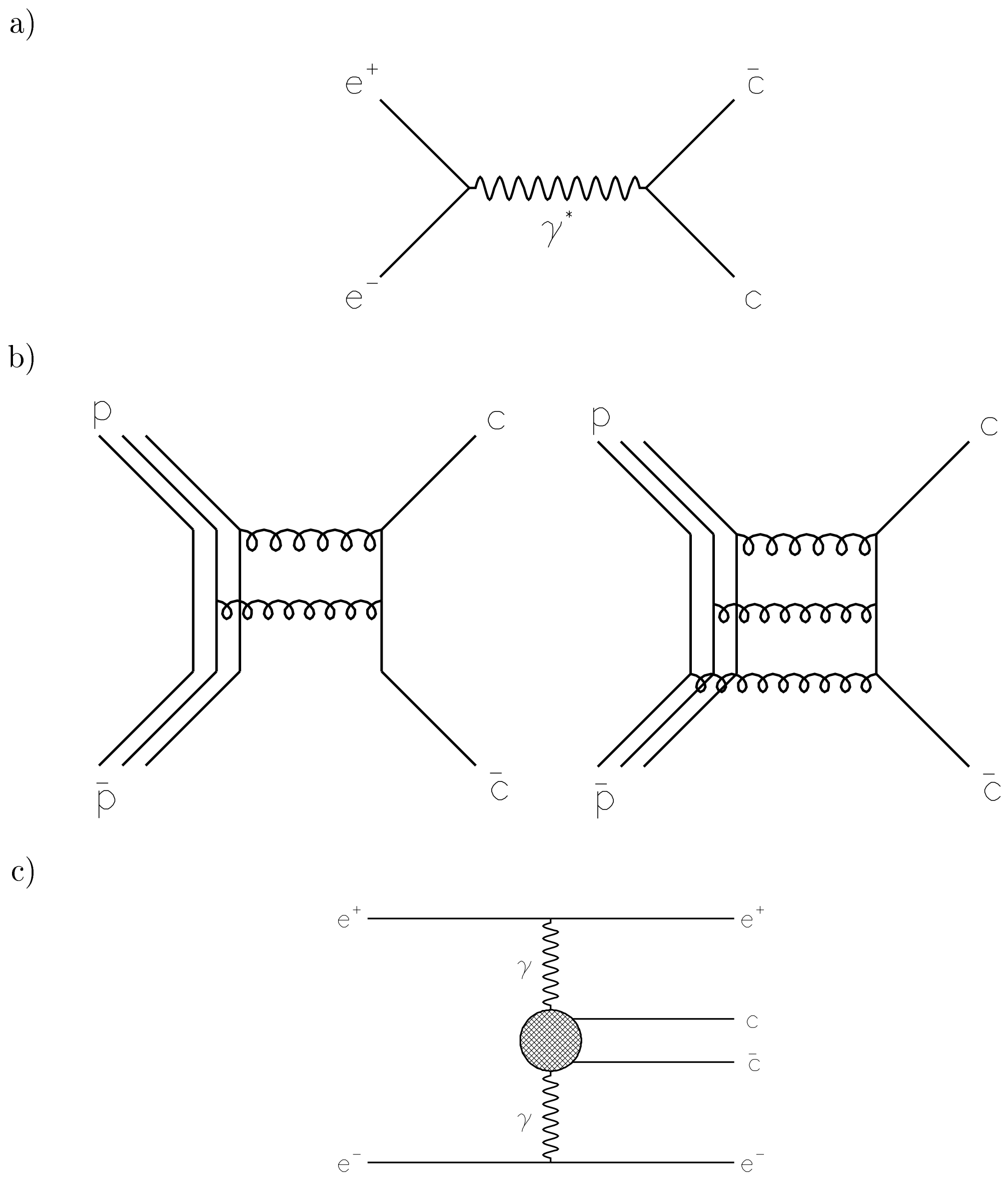

Figure 1.5: The three methods of charmonium production used to date in experiments.

cult at e^+e^- colliders. No evidence existed for the $h_c(^1P_1)$, and almost no hope of finding it with the decay $\psi' \to \gamma\eta_c' \to \gamma\gamma h_c$ involving sequential transitions. The narrow widths of the χ_1 and χ_2 states were too small to extract from the data, even with Crystal Ball's impressive energy resolution.

With the advent of stochastic cooling, the accumulation of antiprotons in a circular ring became possible and $\overline{p}p$ collisions emerged as another option for charmonium formation. When the proton and antiproton coherently annihilate into $2(C = +)$ or $3(C = -)$ gluons, figure 1.5(b), all of the charmonium states can be formed directly. With direct formation of the states, the mass resolution depends not upon the detector, but on the knowledge of the momentum distribution of the beam(s). The detector is instead used only to identify the charmonium decays. Experiment R704[21] pioneered a technique for $\overline{p}p$ formation of charmonium states in the ISR storage ring at CERN, using a stochastically cooled antiproton beam and a hydrogen gas-jet target. Unlike e^+e^- collisions, $\overline{p}p$ annihilation is accompanied by an immense hadronic background, measured in mb. R704 not only demonstrated that charmonium signals can be extracted from this background by selecting only electromagnetic final states, but also made the first measurement of the width of the χ_2, and improved the measurements of the χ_1 and χ_2 masses. With this technique proven, experiment 760 was designed for operation in the Antiproton Accumulator at Fermilab. After collecting and analyzing ~ 30 pb^{-1} of data, evidence for the h_c state was reported[12] and precise measurements of the χ_1, χ_2[14] and η_c[16] resonance parameters published. Figure 1.6 is the excitation curve of the η_c resonance measured by E760. Even with the advantages of $\overline{p}p$ production, the η_c remained elusive.

Interactions involving e^+e^- at higher energies can also produce the even J states through two virtual photons, figure 1.5(c). The production rate, however, decreases by a factor α^2 from the rate for a single photon. Despite the low event rate, there

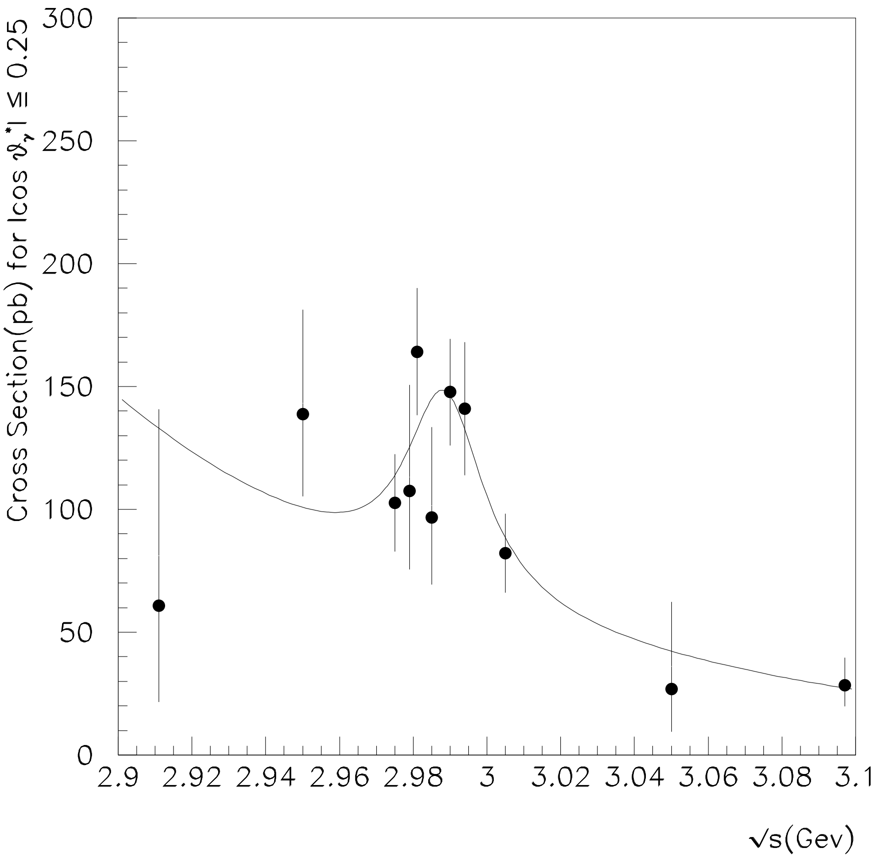

Figure 1.6: The η_c resonance seen in the reaction $\overline{p}p \to \eta_c \to \gamma\gamma$ by E760 at Fermilab.

have been many recent experiments at e^+e^- colliders where a measurement of the $\gamma\gamma$ widths of the $\overline{c}c$ states with even values of J is feasible because of the large amount of integrated luminosity collected.

E835 has taken over 150 pb^{-1} of data. The large increase over E760 facilitates the most thorough measurement of the η_c resonance parameters to data, an extended search for the η_c' and an improved measurement of the two-photon decay width of the χ_2. E835 has also observed the first direct production of the χ_0 resonance in $\overline{p}p$ annihilations.

1.2 Theoretical Predictions

The discovery of the J/ψ and the promise of a system of charmonium states analogous to those of the hydrogen atom and positronium provided exactly the testing ground for QCD that the theorists had been seeking. The similarity of charmonium to positronium was quickly exploited. Calculations of the partial widths $\Gamma_{e^+e^-}(J/\psi)$, $\Gamma_{ggg}(J/\psi)$, $\Gamma_{\gamma\gamma}(\eta_c)$, and $\Gamma_{gg}(\eta_c)$ were as simple (to zeroth order) and m_e with m_c as replacing α with α_s where necessary in the corresponding positronium calculations, and multiplying by a color factor in the case of the gluonic final state. The immediate prediction in one paper[11] of the $\overline{c}c$ ground state at 3 GeV with a width of 6 MeV is surprisingly close to today's measurements. However, it was quickly realized that the similarity to positronium merely concealed a complex quark interaction quite unlike the simple Coulomb one.

A non-relativistic model, proposed by Applequist, Politzer and others, describes the $\overline{c}c$ system by a wave function $\phi(r)$ satisfying a Schrödinger equation for some appropriate potential $V(r)$. One such potential is the Cornell potential[45], inspired by the QCD ideas of quark confinement and asymptotic freedom:

$$V(r) = -\frac{4}{3}\frac{\alpha_s}{r} + ar \tag{1.1}$$

There are various potentials in the literature, all able to describe the spin-averaged charmonium spectrum quite well, since they exhibit similar r dependences in the range from 0.1 fm to 1.0 fm[39].

In order to calculate the fine structure ($^3P_{0,1,2}$ splittings) and the hyperfine structure (^{3}S$-^1$S and ^{3}P$-^1$P splittings), the spin-dependent interactions must be incorporated into the potential. This was first done independently by Schnitzer[76] and Pumplin, et al.[72] in 1975. They postulated that there are two dominant terms in the potential, due to vector and scalar exchange, $V(r) = V_v(r) + V_s(r)$. This assumption is motivated by the existence of pseudoscalar and vector charmonium states. A second assumption, that heavy quark binding is due to single gluon exchange, allowed them to follow the map drawn by successful positronium calculations, and use the Breit-Fermi Hamiltonian[2] to include the spin dependent terms.

For a system of two particles with the same mass, the Hamiltonian, expanded perturbatively to first order in v^2/c^2, is given by

$$\begin{aligned} H = H_0 + H_1 \quad &= \quad \left[2m + \frac{p^2}{m} + V_s(r) + V_v(r)\right] + \\ &\quad \left[-\frac{p^4}{4m^3} + H_{SI} + H_{SO} + H_T + H_{SS}\right] \end{aligned} \tag{1.2}$$

where m is the mass of the charmed quark. The term H_1 includes a spin-independent term:

$$\begin{aligned} H_{SI} \quad &= \quad \frac{1}{4m^2}\left[\frac{2L(L+1)}{r}V_v' + \left[p^2, V_v - rV_v'\right]\right. \\ &\quad \left. +2\left(V_v - rV_v'\right)p^2 + \frac{1}{2}\left(\frac{8}{r}V_v' + V_v'' - rV_v'''\right)\right] \end{aligned} \tag{1.3}$$

a spin-orbit interaction term:

$$H_{SO} = \vec{L}\cdot\left(\vec{S_1} + \vec{S_2}\right)\frac{1}{2m^2 r}\left(3V_v' - V_s'\right) \tag{1.4}$$

a tensor interaction term:

$$H_T = \left[\left(\vec{S_1}\cdot\hat{r}\right)\left(\vec{S_2}\cdot\hat{r}\right) - \frac{\left(\vec{S_1}\cdot\vec{S_2}\right)}{3}\right]\frac{1}{m^2 r}\left(V_v' - rV_v''\right) \tag{1.5}$$

and a spin-spin interaction term:

$$H_{SS} = \left(\vec{S_1}\cdot\vec{S_2}\right)\frac{2}{3m^2}\nabla^2 V_v \tag{1.6}$$

[2] A derivation of the Breit-Fermi Hamiltonian appears in many texts on QED, including reference [32], which also covers the application of the Breit-Fermi Hamiltonian to the positronium system.

where $\vec{L}, \vec{S_1}, \vec{S_2}$ are the orbital and spin angular momenta, m is the quark mass, and primed quantities denote the derivative d/dr. The mass difference between the $^1S_0$ (η_c and η_c') and the $^3S_1$ (J/ψ and ψ') states arises from the spin-spin interaction term, since the spin-orbit and tensor terms vanish for the $J = 0$ states. The mass splitting that results is

$$\Delta E = \frac{2}{3m_c^2}\langle \nabla^2 V_v \rangle \tag{1.7}$$

where the angle brackets indicate the expectation value, evaluated with respect to the unperturbed wave functions. Measurements of this splitting provide a test of the chosen potential form.

As more charmonium states were discovered and measurement quality improved, the potentials were refined. A Coulomb-like potential is most often assumed for V_v in the form $V_v = -4/3(\alpha_s/r)$. With this form for the potential, the S-state hyperfine splitting is given by

$$\Delta E = \frac{32\pi\alpha_s}{9m_c^2} \mid \psi_S(0) \mid^2 \tag{1.8}$$

where $\mid \psi_S(0) \mid^2$ is the square of the wavefunction at the origin. The direct relation of the hyperfine splitting, ΔE, to the quantities m_c and α_s provides a sensitive test of lattice QCD methods[61]. The relation can also be used to calculate phenomenological values for m_c and α_s, unknowns in potential model calculations.

In addition to the mass splittings, annihilation rates into two or three gluons and two photons for the various states have been predicted. The analogy to positronium provides zeroth order estimates for these rates. The first perturbative calculations were based upon the assumption that the decay rates can be factored into a non-perturbative part involving the wavefunction and a perturbative part that can be expanded in powers of α_s. Bodwin, Braaten and Lepage[36] offer this conceptual description of factorization

> Factorization occurs in the annihilation decay rates because the heavy quark and antiquark can annihilate only when they are within a distance of order $1/M$, where M is the heavy quark mass. Since, in the meson rest frame, the heavy quark and antiquark are nonrelativistic ... this is much smaller than the size of the meson, which is on order $1/Mv$. Factorization involves separating the relativistic physics of annihilation (which involves momenta $p \sim M$) from the nonrelativistic physics of quarkonium structure (which involves $p \sim Mv$).

The long distance (nonperturbative) effects must be either calculated with some non-perturbative method, such as lattice QCD, or absorbed into a small set of parameters that can be determined phenomenologically.

An early paper by Kwong et al.[62] calculates the gluonic and $\gamma\gamma$ partial widths to first order in α_s using this assumption. In the ratios of these widths, unknown terms such as the wavefunction and/or the mass of the charmed quark, often cancel, reducing the ambiguities when comparing theory and data. For example, the predictions for the η_c are

$$\Gamma(\eta_c \to \gamma\gamma) = \frac{12\pi e_q^4 \alpha^2}{m_q^2} |\psi(0)|^2 \left[1 - \alpha_s \frac{3.4}{\pi}\right] \tag{1.9}$$

$$\Gamma(\eta_c \to gg) = \frac{8\pi \alpha_s^2}{3m_q^2} |\psi(0)|^2 \left[1 + \alpha_s \frac{4.8}{\pi}\right] \tag{1.10}$$

The ratio of these two partial widths depends only on α_s, thus α_s can be inferred by a measurement of the branching ratio $B(\eta_c \to \gamma\gamma)$.

The factorization method was placed upon a firm theoretical foundation with the recent development of Nonrelativistic QCD by Bodwin, Braaten and Lepage[36], a theoretical breakthrough in part credited to the results published by E760[37]. NRQCD is an effective field theory of QCD that includes perturbative and relativistic corrections in a rigorous way, resolving the infrared divergences in previous calculations. It is the starting point for all recent papers on charmonium annihilation rates that use a nonrelativistic approach. Braaten points toward measurements of the $\gamma\gamma$

	$\Gamma(\eta_c \to \gamma\gamma)$ (keV)	$\Gamma(\eta_c' \to \gamma\gamma)$ (keV)
Chao *et al.*[41]	6-7	2
Kroll[60]	7.21	0.13
Gupta *et al.*[53]	10.94	-
Münz[66]	3.5 ± 0.4	-
Ackleh and Barnes[4]	4.8	3.7

	$\Gamma(\chi_0 \to \gamma\gamma)$ (keV)	$\Gamma(\chi_2 \to \gamma\gamma)$(keV)
Chao *et al.*[56]	3.72 ± 1.11	0.49 ± 0.15
Gupta *et al.*[53]	6.38	0.57
Münz[66]	1.39 ± 0.16	0.44 ± 0.14
Bodwin *et al.*[36]	$11.3 \pm^{4.7}_{4.0}$	0.82 ± 0.23

Table 1.1: Some of the recent theoretical predictions for two photon decays of charmonium.

decay rates of the χ_2, χ_0, and η_c as places to compare their results with experiment and test the new formalism[37].

The unification of the non-relativistic approach facilitates its comparison with the relativistic approaches attempted by some authors, such as Münz[66] and Ackleh and Barnes[4]. They have developed relativistic calculations, which are used to predict the $\gamma\gamma$ decay rates for light quarkonia as well. Münz also suggests that measurements of the $\gamma\gamma$ decay rates of the χ_0, and η_c will give a quantitative evaluation of his results. Their predictions are listed in table 1.2. The numbers of Bodwin et al.[36] are obtained from the predicted branching ratios using the experimental total widths $\Gamma_{\chi_2} = 2.0 \pm 0.2$ MeV[52] and $\Gamma_{\chi_0} = 16.6 \pm^{5.2}_{3.7}$ MeV[9]. Measurements of these partial widths are presented in this dissertation.

Chapter 2

Experimental Apparatus

2.1 Experimental Technique

The charmonium states are studied by decelerating the antiproton beam in small steps through the expected resonance and measuring the cross section at each step. A model of the resulting excitation curve is shown in figure 2.1. The curve is the convolution of the Breit-Wigner cross section for the resonance with the energy distribution function of the beam,

$$\sigma(E_{cm}) = \int_0^\infty \sigma_{BW}(E')G(E' - E_{cm})dE' \tag{2.1}$$

where $G(E)$ is the normalized beam-energy distribution function in the center-of-mass frame and

$$\sigma_{BW}(E) = \frac{4\pi}{k^2}\frac{2J+1}{(2S_1+1)(2S_2+1)}\frac{\Gamma_{in}\Gamma_{out}}{4(E - M_R c^2)^2 + \Gamma_R^2} \tag{2.2}$$

where J is the spin of the resonance, k is the center-of-mass momentum for the collision, and $\Gamma_{in(out)}$ is the partial decay rate of the resonance into the initial(final) state. If $G(E)$ is known, then the resonance parameters M_R, Γ_R, and the product of the branching ratios, $B_{in}B_{out}$, can be extracted from the measured curve. This technique is advantageous since the energy in the center-of-mass frame (the horizontal

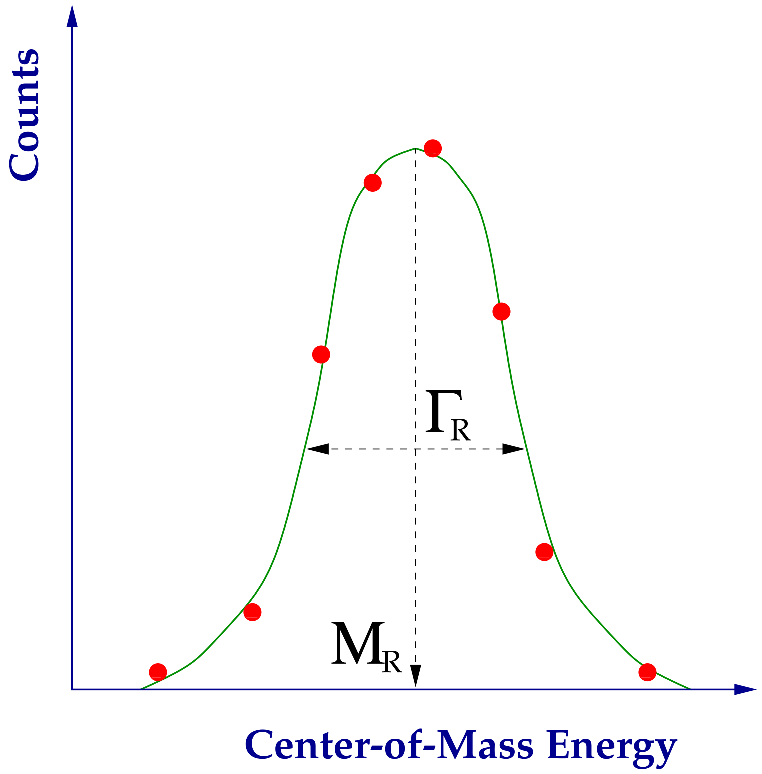

Figure 2.1: A model of a resonance scan.

axis in figure 2.1) is obtained by measuring the beam energy distribution instead of measuring the energy of the particles in the final state with the detector.

2.2 Antiproton Accumulator

The ability of E835 to make precision measurements depends crucially upon the high quality beam of antiprotons provided by the Fermilab Antiproton Accumulator. A diagram of the antiproton source at Fermilab is shown in figure 2.2. 120 GeV protons are extracted from the Main Ring, in pulses separated by ∼2 seconds, and directed toward the target at AP0. The target is a stack of nickel disks. The disks rotate about their common axis to prolong the life of the target. The cone of secondary

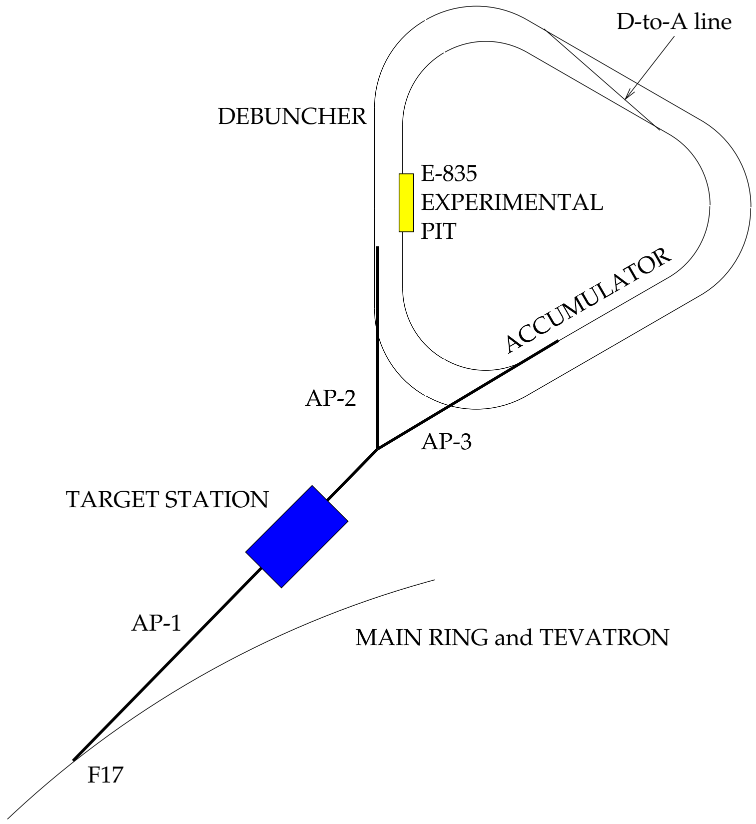

Figure 2.2: The layout of the antiproton source.

particles produced is then focused with a lithium lens, a cylinder of lithium subjected to an intense longitudinal current. The resulting azimuthal magnetic field quickly focuses the beam in both the horizontal and vertical planes simultaneously. A dipole magnet bends the focused beam into the AP2 line, and eventually the Debuncher. Secondaries which are not antiprotons, are either bent out of the beam pipe by the dipole or decay before reaching the Debuncher. The entire process yields a single antiproton in the debuncher for every 50,000 initial protons.

The Debuncher and Accumulator are two rings which share the same tunnel, shown in figure 2.2. The antiprotons are collected in the Debuncher as a bunched beam. The Debuncher has a large momentum aperture, $\frac{\Delta p}{p} \sim 0.04$, in order to collect as many antiprotons as possible. A single pulse is collected, the beam is debunched and then transferred to the Accumulator so the Debuncher can accept the next pulse. Together, the debunching of the beam and the stochastic cooling in the Accumulator reduce the momentum spread to about 0.1%. The antiprotons are stacked in the accumulator for several hours, until the desired beam density is reached, usually $\sim 50 \times 10^{10}$ antiprotons. A typical stacking rate during the E835 run was 3×10^{10} $\overline{p}$/hour.

Precise knowledge of the beam energy distribution is crucial for the measurements made by E835. The precision of the measurement of a resonance mass depends upon the precision of the average beam energy measurement. The precision of the beam energy width measurement affects how well the width of a narrow resonance can be determined. The beam energy is related to the revolution frequency and the orbit length

$$\beta c = fL \tag{2.3}$$

where βc is the speed of the antiprotons, f is the revolution frequency and L is the orbit length. The mean revolution frequency, ~ 0.6 MHz, is measured with an accuracy less than 1 Hz and the orbit length to ~ 0.5 mm, determining the mean center-of-mass energy ($\sqrt{s}$) to less than 100 keV, dominated by the error in the measured orbit length.

Since the orbit length varies slightly with the beam momentum, it is easier to measure changes in the orbit length from some reference orbit, characterized at the beam momentum corresponding to the ψ' resonance, whose mass is known to 90 keV. The reference orbit length for E835 is $L_0 = 474050 \pm 1$ mm. Changes in the orbit length at different beam momenta are measured with BPMs (Beam Position Monitors). There are 48 horizontal and 42 vertical BPMs positioned around the Accumulator. There are 38 dipole magnets that bend the beam horizontally around the ring. The orbit displacement created by each individual magnet is measured by at least one BPM. Using a computer model of the accelerator lattice and the BPM measurements, the orbit length can be determined to ± 0.5 mm[50].

The revolution frequency distribution is measured from the Schottky noise spectrum. Schottky noise bands are present at integer multiples of the beam frequency, and their amplitude is related to the number of antiprotons traveling at that frequency. A spectrum analyzer records the power spectrum, $P(f)$, essentially the particle density of the beam in frequency space. From the relation,

$$P(f) = 2\pi(ef)^2 \frac{dN}{df} \tag{2.4}$$

the frequency spectrum of the beam is determined. The momentum distribution can then be obtained from the relation

$$\frac{dp}{p} = -\frac{1}{\eta}\frac{df}{f} \tag{2.5}$$

where $\eta \equiv 1/\gamma_t^2 - 1/\gamma^2$ is the slip factor, with $\gamma = E_{beam}/m_p$. [1] The value of γ at transition, γ_t, is a characteristic of the accumulator lattice. For $\gamma = \gamma_t$, the beam is very unstable, and decelerating the beam through this point is done carefully and with smaller beam currents to minimize losses. The χ_0 resonance mass is unfortunately very near to this point, limiting the amount of data taken by E835 at this resonance.

2.3 Hydrogen Gas-Jet Target

A hydrogen gas-jet target was chosen for E760 and E835 because it uses the coasting antiproton beam efficiently without increasing the size or momentum spread

[1] A complete discussion of accelerator physics can be found in reference [44].

Figure 2.3: Formation of the stream of hydrogen gas clusters, due to the expansion of the gas inside the nozzle.

of the beam. The nozzle of the gas-jet is trumpet-shaped. As the trumpet widens, the gas adiabatically expands, and condenses into clusters at the trumpet axis, as shown in figure 2.3. The dense cluster stream is selected from the remaining gas by two skimmers, the second of which determines the radius of the jet at the interaction region (see figure 2.5). The skimmers also reduce the amount of background gas, which can spoil the vacuum in the accumulator. A system of pumps eliminates the remaining background gas, so that 95% of the gas in the beam pipe is contained in the 7 mm wide cylindrical jet[7]. Figure 2.4 shows the profile of the gas-jet in the interaction region.

The interaction rate comfortably tolerated by the data acquisition system is 1.4 MHz, or an instantaneous luminosity of 2×10^{31} cm^{-2}s^{-1}. The amount of data collected is maximized if this rate can be maintained for the life of an antiproton beam. E835 accomplished this by increasing the density of the gas-jet as the circulating antiproton beam became depleted. The target has a density range of $(0.1 - 3.2) \times 10^{14}$ atoms/cm^3. A beam current of 2.5×10^{11} antiprotons requires the maximum target density to obtain the desired interaction rate. Data taken with beams smaller than this current was taken at a lower event rate. However, small beam currents were used despite the lower rate for data taken below the transition

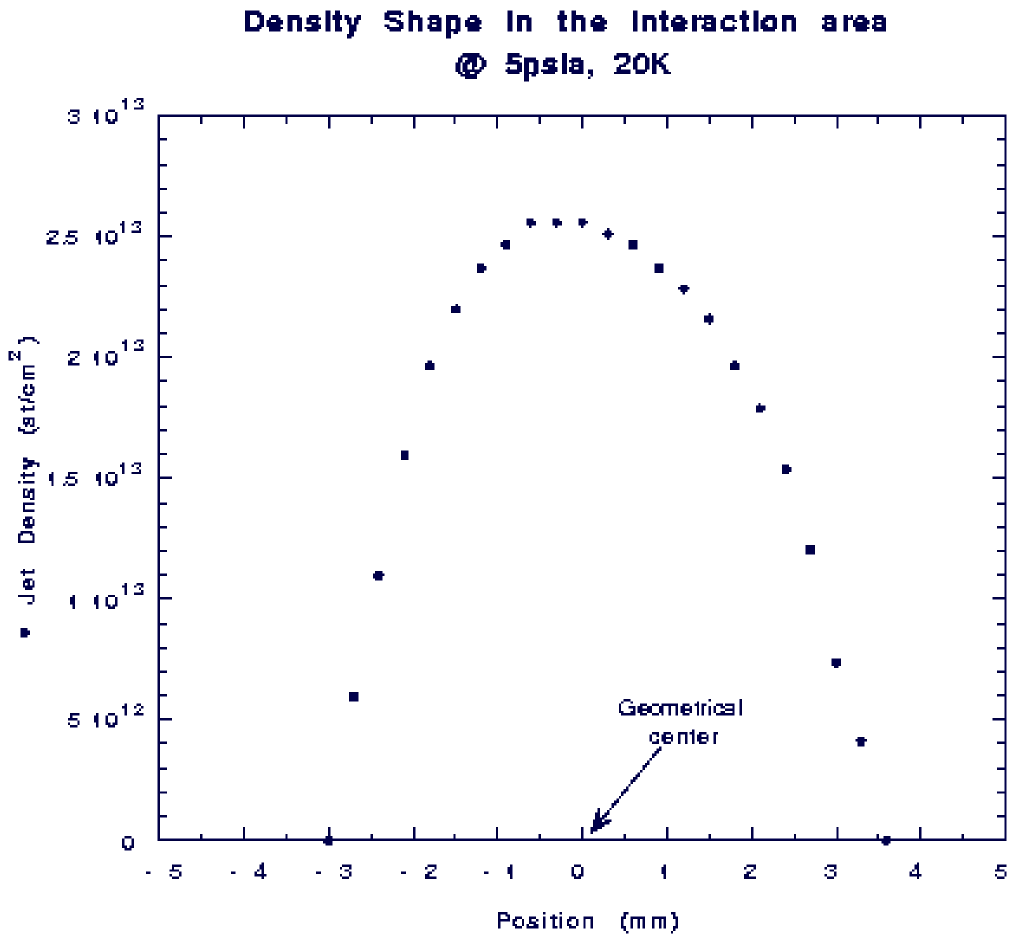

Figure 2.4: The jet density profile in the interaction area at 5 psia and 20K.

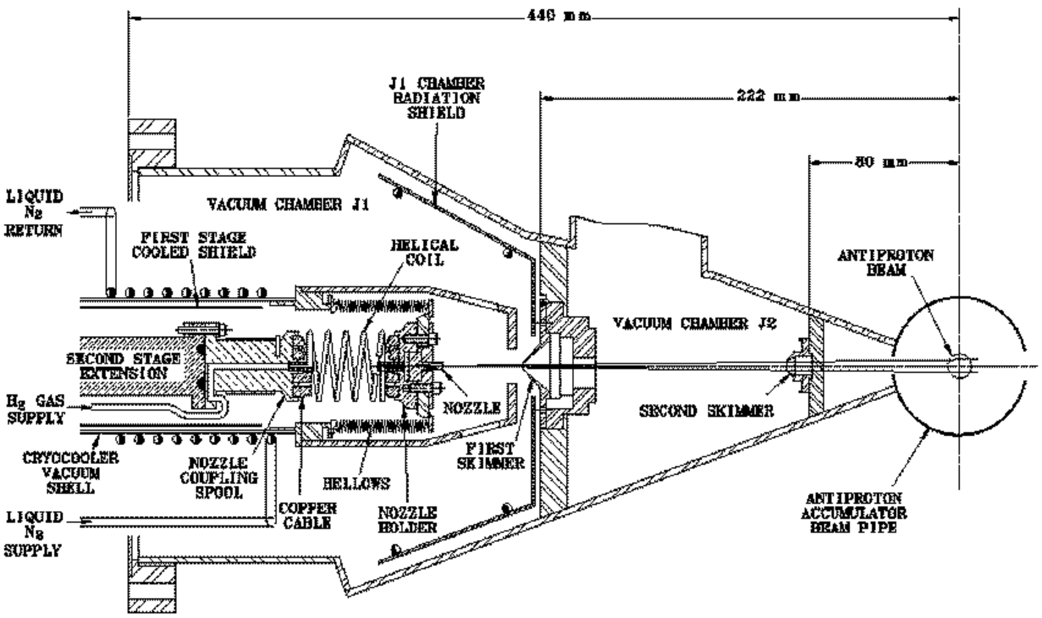

Figure 2.5: Schematic diagram of the gas-jet head.

energy of the beam, ($\sqrt{s} = 3.4$ GeV), since decelerating the beam through transition was more efficient with smaller beam currents.

The integrated luminosity is obtained by counting the number of recoil protons from $\overline{p}p$ elastic scattering in a silicon detector located 86.4° from the beam direction[78]. Since the differential cross section for elastic $\overline{p}p$ scattering at small angles is well-measured, the integrated luminosity can be obtained from the number of observed counts using the following equation

$$\mathrm{N} = \epsilon \int L dt \int \frac{d\sigma}{d\Omega} d\Omega \tag{2.6}$$

where the integral is over the active area of the detector and ϵ is the detection efficiency. The statistical error on the E835 luminosity measurement, at most 0.3%, is negligible compared with the error in the measured differential cross section, $\sim$ 2.2%[71].

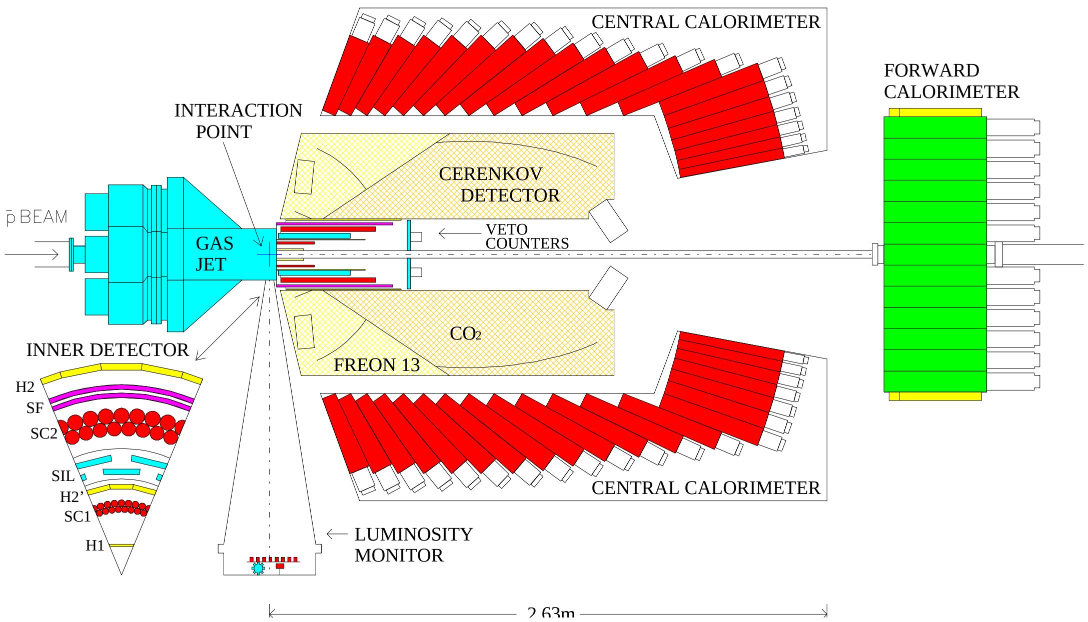

Figure 2.6: The E835 detector layout.

2.4 The Detector

The E835 detector, shown in figure 2.6, is a non-magnetic spectrometer cylindrically symmetric around the antiproton beam axis. It is an upgrade of the E760 detector. Selection of the $\gamma\gamma$ final state uses only the central calorimeter and the hodoscopes. The remaining parts of the detector are for charged particle tracking and identification. Figure 2.7 shows the layout of the inner detectors, used for triggering and charged tracking. Three layers of plastic scintillator hodoscopes, segmented in ϕ, identify charged particles quickly for the trigger. The scintillation light travels through light guides to photomultiplier tubes. Offline, their pulse heights are used to distinguish single charged particles from electron-positron pairs.

Two concentric cylinders of straw tubes measure ϕ of charged particles[23]. Each cylinder consists of two staggered layers of drift tubes, whose axes are parallel to the

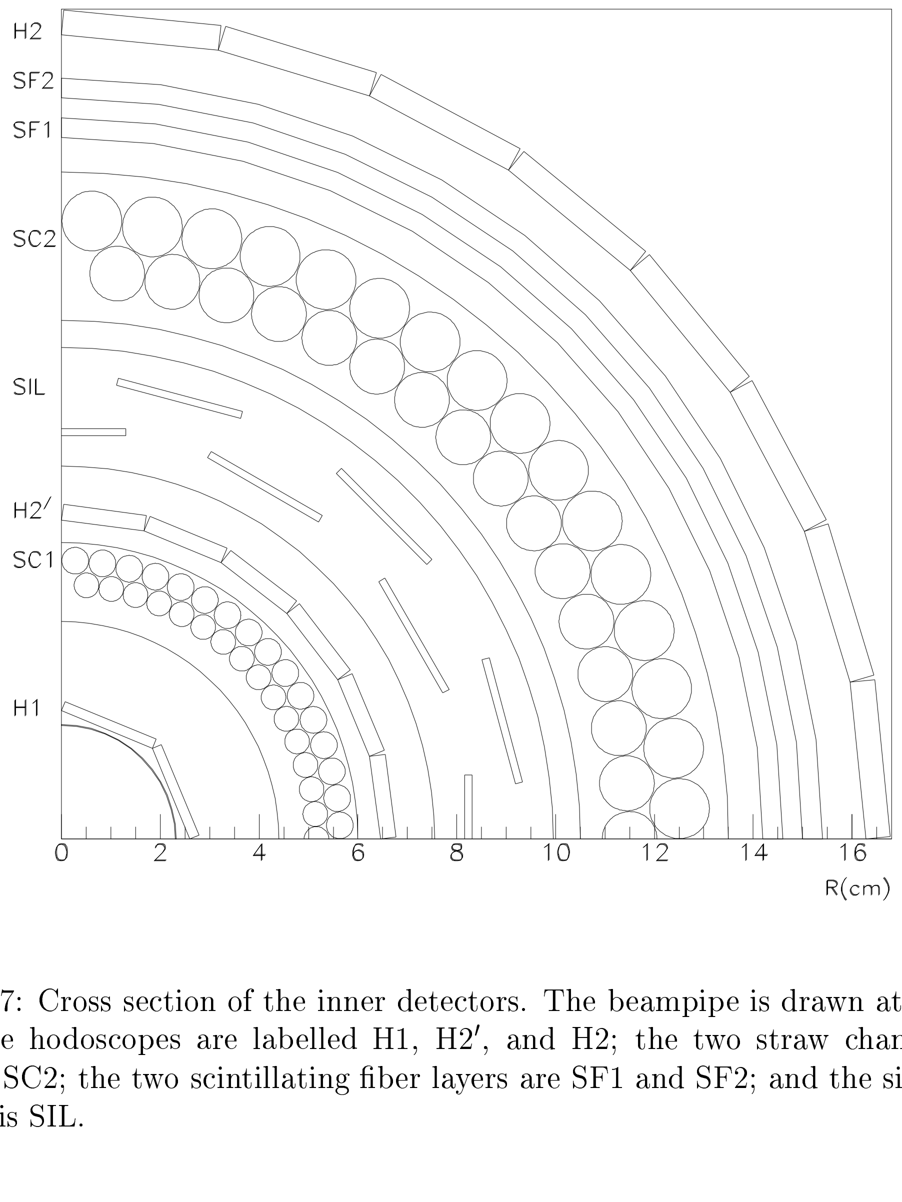

Figure 2.7: Cross section of the inner detectors. The beampipe is drawn at 2.25 cm. The three hodoscopes are labelled H1, H2′, and H2; the two straw chambers are SC1 and SC2; the two scintillating fiber layers are SF1 and SF2; and the silicon pad detector is SIL.

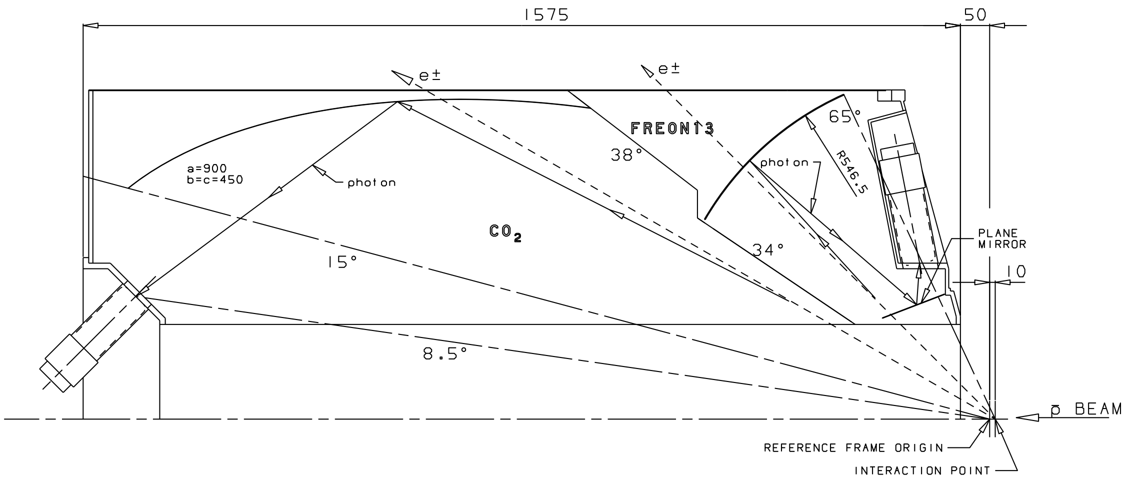

Figure 2.8: Schematic of one octant of the Čerenkov counter. Dimensions shown are in mm.

beam pipe. The gas inside the tubes is a mixture of Ar,C_4H_{10}, and $(OCH_3)_2CH_2$. Two layers of scintillating fibers[8] measure θ of charged particles. Light from the fibers is collected with VLPCs (Visible Light Photon Counters), solid state devices with high quantum efficiency, which operate at cryogenic temperatures. A silicon pad detector was also installed to measure both ϕ and θ[40], but never used in the analysis due to excessive electronic noise.

Combined, the inner tracking systems have a resolution of 12 mrad in ϕ and $4-10$ mrad in θ, with better resolution at smaller angles[27]. The range in the θ resolution comes from the scintillating fibers, where the number of fibers traversed by a single particle changes with θ.

Outside the inner detectors, is the threshold Čerenkov counter[24], which separates electrons and positrons from other charged particles. It is segmented into 8 cells in ϕ and 2 in θ, covering the polar region between 15° and 65°. The two cells in θ contain two different gases, CO_2 in the downstream cells, and Freon-13 in the upstream cells. Neither gas alone could provide electron/pion separation over the large range of velocities corresponding to the entire θ region. Fewer than 0.5% of the charged πs are identified as electrons by the Čerenkov[10].

The outermost cylindrical layer is the lead glass central calorimeter, an array of 1280 lead-glass Čerenkov counters. The calorimeter measures the energy and position of electrons, positrons and photons. It is the only detector that *sees* neutral particles, and is the essential component of the neutral trigger and analyses. It is discussed in detail in chapter 3.

In the forward, or small θ, region, there is a veto counter and electromagnetic calorimeter. The forward charged veto, FCV, is a plastic scintillating hodoscope which covers from 2° to 10° in θ, and the full azimuth. The FCV identifies charged particles, and is used as a veto in the neutral trigger. At the beginning of the 1996-97 run, the forward calorimeter from E760 (FCAL1)[55] was used. It consists of 144 rectangular blocks of lead-scintillator sandwich, whose layout is shown in figure 2.9. A wavelength shifter, covering one side of each block along the beam axis, collects the light from the scintillator pieces, and transports it to a photomultiplier tube. It also changes the wavelength of the light to optimize the PMT signal. There were difficulties calibrating FCAL1, which deteriorated more than expected since E760. During the shutdown in March 1997, FCAL1 was replaced with FCAL2[22] to improve the energy resolution and reliability. FCAL2 is an array of 144 lead-glass blocks readout with photomultiplier tubes.

2.5 Data Acquisition System

The Data Acquisition System (DAQ) receives, processes and stores information from four sources, or streams. The ACNET stream comes from the Accelerator complex computers and contains information about the antiproton beam, such as

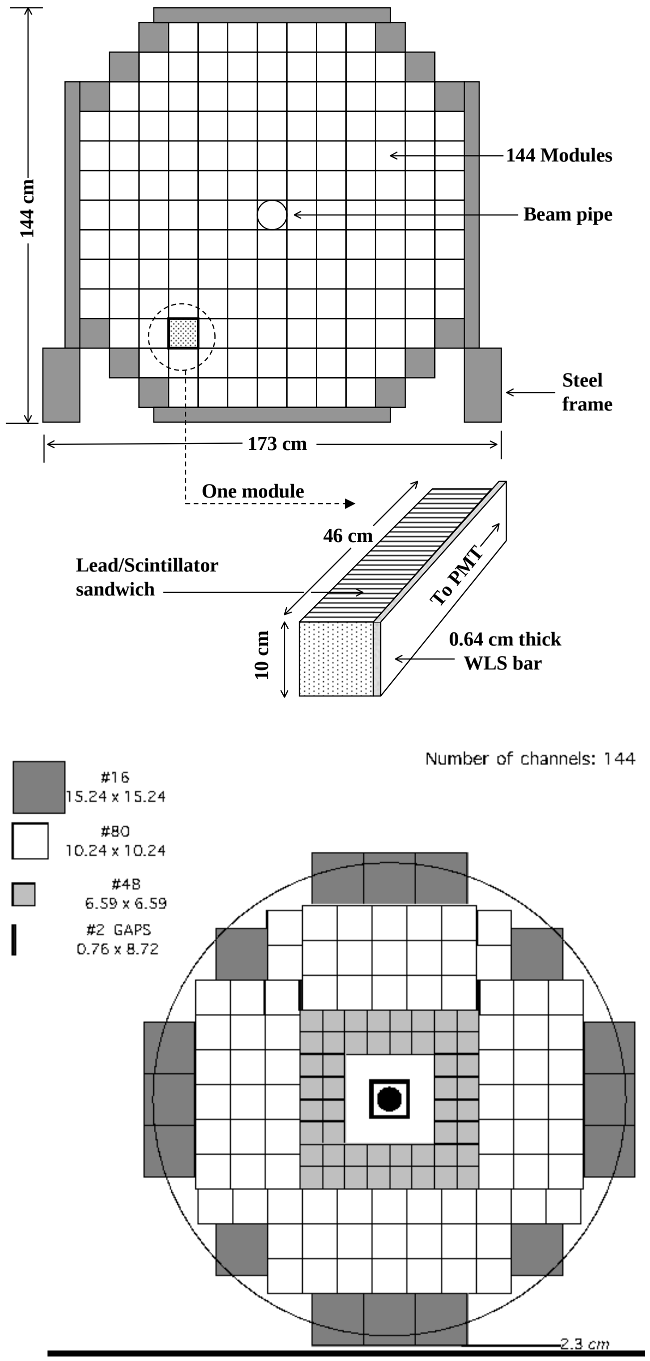

Figure 2.9: The two forward calorimeters used in E835: above, the layout of FCAL1 (scintillator/lead modules) and below, the layout of FCAL2 (lead-glass modules).

the frequency spectrum, beam position (from BPMs), and beam intensity. A second stream consists of the data from the luminosity monitor. The third stream is the scaler data stream. The scalers measure the activity rates of the triggers and subdetectors. The fourth stream is the actual experimental data from the detector. In this stream, the DAQ collects the signals from the detectors, packages them into events, and records them on tape and/or disk for later analysis. This fourth stream is the focus of this section.

There are two bottlenecks in the data stream, which affect the maximum event rate that the DAQ can handle with a reasonable efficiency. The first is the time required to collect the information from the detector's readout electronics, $\sim 20\ \mu$s, and the second is the rate at which the DAQ can record data to tape or disk.[2] E835 utilized both a hardware trigger and a software filter to discard events before each bottleneck, and increase the maximum event rate. Even more importantly, the trigger and filter enrich the charmonium (and other physics studied by E835) fraction within the data sample, improving offline analysis speed and reducing data storage overhead. The specific cuts of the trigger and filter and their implementation are discussed in detail after an explanation of the DAQ hardware and setup.

Since many experiments took data during the fixed target run in 1996-97, the DART (Data Acquisition fixed taRgeT) collaboration was created to develop a common system of hardware and software as a foundation for the DAQ system of the individual experiments. The E835 DAQ system was built upon this platform, optimizing the readout time without endangering the quality of the data. A diagram of

[2]Data can be written to tape at 0.4 MBytes/s (per tape drive), approximately 500 events/s for E835. The speed of each SCSI bus (there are 3) connecting the Challenge to the tape drives is about 1 MBytes/s, limiting the number of tapes that we can write at once, and thus the total number of events.

the hardware is shown in figure 2.10. The DAQ moves the data from the detector's readout electronics to the main computer of the DAQ in 3 stages. In each stage, the data are combined into larger and more structured buffers.

The detector signals are digitized by an ensemble of 163 ADC (LRS4300B), 66 TDC (LRS3377) and 23 PCOS (LRS2371) modules, housed in 14 CAMAC crates, and collectively referred to here as the readout electronics. The modules are connected in three streams to an SGI Indy computer via the CAMAC backplane and SCSI 411 Jorway interfaces. This connection is too slow for data taking, but useful for debugging and programming the modules. In data-taking mode, data is transferred from the individual modules to a DYC[43] module inside each crate via their front-end ECL-ports. The DYC module was developed at Fermilab as part of the DART project. It is an intermediate data buffer that changes the data format from 16-bit to 32-bit and packages the data from up to 23 readout modules. While data is being transferred from the readout electronics to a DYC, the DYC sends a busy signal to the trigger logic. One or more busy signals will inhibit the trigger from accepting the next event. Deadtime is the fraction of time that the trigger is inhibited while taking data. E835 ran with a deadtime of less than 5%.

The 14 DYCs are divided into two streams; the DYCs of each stream transfer their data, in series, to a pair of DC2/DM115 modules in a VME crate over a RS-485, or DART, cable. The DYC can simultaneously collect the data from the readout modules and send data over the DART cable. Each DC2 module is connected to two 32-MB DPMs (Dual Ported Memory) and one 8-MB DPM via the backplane of the VME crate. The DC2 fills one of the large DPMs with exactly N events. While the DC2 is filling one DPM, the gateway reads the other DPM via PTI, the hardware and protocol that enable communication between the two systems. The 8-MB DPM is used as a mailbox for communication between the gateway and the DC2. The

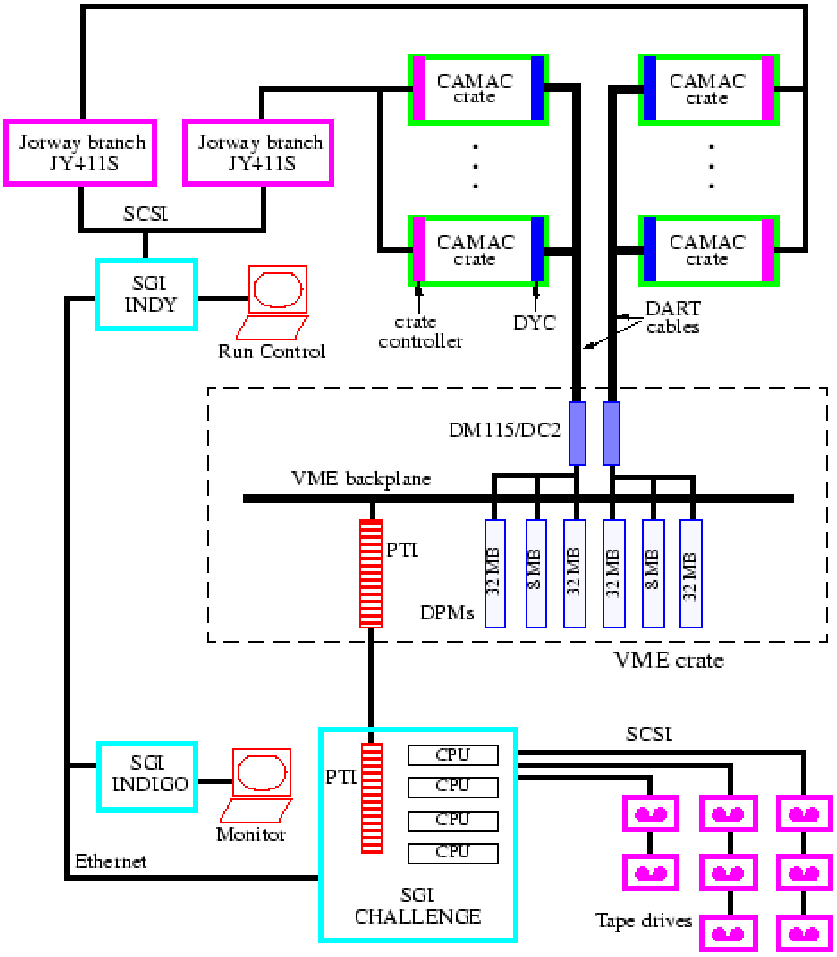

Figure 2.10: E835 data acquisition hardware layout.

gateway is a process running on the main computer of the DAQ, a SGI Challenge with 4 150-MHz CPU processors. Until this point, the data paths for the two DART streams are parallel but separate, each event divided between the two streams. The gateway combines the two corresponding buffers into a single buffer (still containing N events) which is then passed to the online filter. The online filter assembles each event and decides whether to discard it.

The good events are packaged and classified, then separated into three streams based upon the classification. Each stream is written to a logging buffer, and eventually to tape. The three streams are labeled GK, GN, and GP, for three categories of final states: e^+e^-X, neutral, and $\phi\phi + \overline{p}p$. These categories follow the descriptions in table 2.1. Two additional logging streams, GNA and gold, contain a duplicate subset of the data for immediate analysis. The logging buffers are also transferred to a third computer, a SGI Indigo, for monitoring the detector.

2.6 Hardware Trigger

The task of the hardware trigger is to reduce the interaction rate of 1.5 MHz to less than 2.5 kHz. There are three branches of the trigger, corresponding to the three different event signatures in the detector, outlined in table 2.1. The neutral branch is the path taken by the $\gamma\gamma$ candidates and and is summarized here. A full description of the E760 neutral trigger is found in reference [73] and the upgrades for E835 in reference [58]. Details on the other two branches can be found in reference [27].

The central calorimeter is the only piece of the detector sensitive to neutral particles, thus it is a crucial part of the neutral trigger. There are two sub-branches of the neutral trigger. The first, the total energy branch, searches for all multi-photon final states by requiring a large fraction of the total energy to be in the CCAL. The sec-

$\phi\phi$	$\overline{p}p \to \overline{p}p$ $\overline{p}p \to \phi\phi \to K^+K^-K^+K^-$
charged	$\overline{p}p \to J/\psi X \to e^+e^-X$
neutral	$\overline{p}p \to \gamma\gamma$ $\overline{p}p \to$ neutral hadrons, i.e. $\pi^0\pi^0$

Table 2.1: The three branches of the hardware trigger and the reactions they select.

ond, the PBG branch, searches for two large energy deposits in the CCAL that satisfy rough two-body kinematics. There is significant overlap between the two branches, providing a very efficient trigger with many cross checks. A diagram of the neutral trigger is shown in figure 2.11.

First the trigger reduces the number of CCAL elements from 1280 blocks to 40 *super-blocks*, which have dimensions 9 wedges x 5 rings, and overlap each other by one block in all directions. The 40 super-block signals are obtained by analog summing in two steps, first over rings and then over wedges. The signal from each PMT is sent to the level 1 summers, where it is split three ways. 95% of the signal is sent to the readout electronics through 320 ns of delay cable. 2.5% of the signal is combined with the blocks from the same ring to form a *total ring* sum. The total ring sums for rings 1-18 are then combined to form the total energy signal. The total energy signal is integrated, and compared with two different thresholds in a discriminator, one for ETOT-HI (80% of the total energy) and one for ETOT-LO (70% of the total energy). Logic signals indicating whether the ETOT-LO and ETOT-HI logics are 'ON' are sent to the NMLU.

The remaining 2.5% in the level 1 summer contributes to the ring sum for each of the super-blocks. The partial ring sums are sent to the level 2 summers, where 5% of the signals are sent to the Min-Bias discriminator (discussed later) and the remaining 95% are used to make a weighted sum over the wedges in a super-block. The weighted

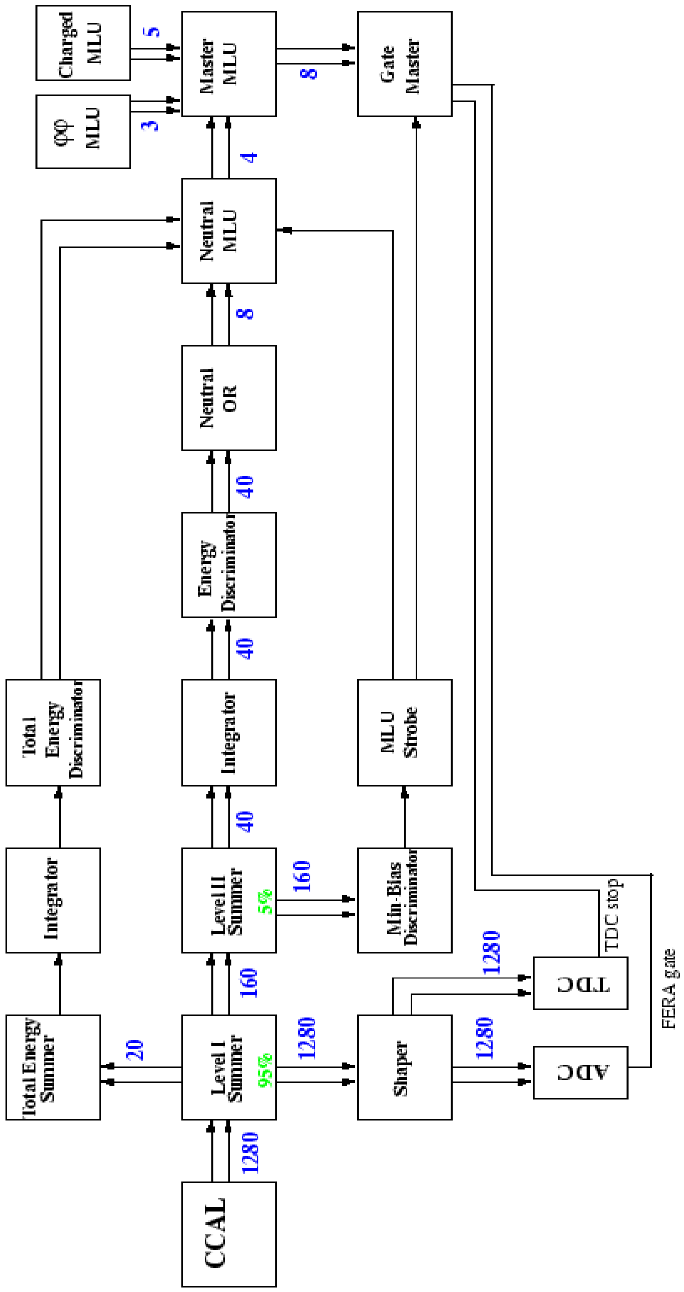

Figure 2.11: Diagram of neutral trigger. The double arrows indicate a set of signals, with a number denoting how many. When signals are passed through the electronics, a percentage (in gray) indicates the change in amplitude.

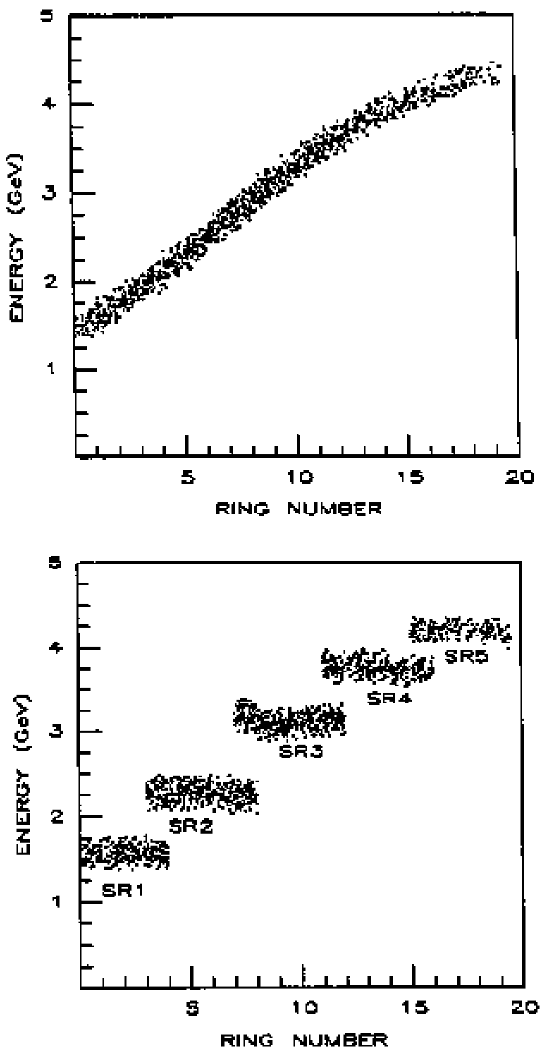

Figure 2.12: Results of an E760 Monte Carlo simulation of the process $J/\psi \to e^+e^-$. The ring number of the CCAL impact point is plotted vs the energy of the particle in the upper plot. In the lower plot, the energies have been weighted as they are in the level 2 summers to show the feasibility of a single energy threshold for the weighted super-ring sum.

sum is necessary because the expected energy deposit from a particle of a two-body decay varies with ring, however it is desired to use a single threshold for all five rings in a super-block. The weighted sum allows the use of a single threshold, as shown in figure 2.12. The 40 super-block signals are then integrated and compared with the appropriate thresholds in a discriminator. The thresholds are set at $\sim 60\%$ of the expected energy. The 40 discriminator outputs, which tell which super-blocks are above threshold, are combined into 8 superwedge signals, each the logical OR of the 5 super-block signals in that super-wedge. These 8 signals are then sent to NMLU.

The NMLU, or Neutral Memory Lookup Module, uses simple pattern matching to discern whether there are two large energy deposits possibly consistent with two-body kinematics. The NMLU has four outputs, as outlined in figure 2.13. Two are just the total energy signals given to the NMLU. PBG1 is 'ON' if there are super-blocks above threshold in two opposing octants (super-wedges) of the CCAL. PBG3 is a looser kinematical requirement than PBG1, requiring that a hit in one octant be paired with a hit in the opposing octant, or one of the octants on either side.

Each branch of the trigger has its own MLU. The Master MLU (MMLU) combines the logic signals from the individual branches and decides whether to send a trigger to the Gatemaster. The inputs and outputs of the MMLU are listed in table 2.6. For the neutral triggers, the MMLU combines the PBG and ETOT signals with a veto on tracks in the hodoscopes. Two MMLU inputs are the FCV-OR, which is 'ON' if there is one or more signals above threshold in the forward hodoscope, and $\mathrm{H1} \cdot \mathrm{H2}'$, which is 'on' if there is a hit over threshold in both a H1 element and one of the three corresponding $\mathrm{H2}'$ elements. The combination $\overline{\mathrm{H1} \cdot \mathrm{H2}'} \oplus \overline{\mathrm{FCV} - \mathrm{OR}}$ is called the *Neutral veto* in the discussion of the trigger efficiencies in section 5.2.1. The four outputs of the MMLU used to select events for the neutral analyses are

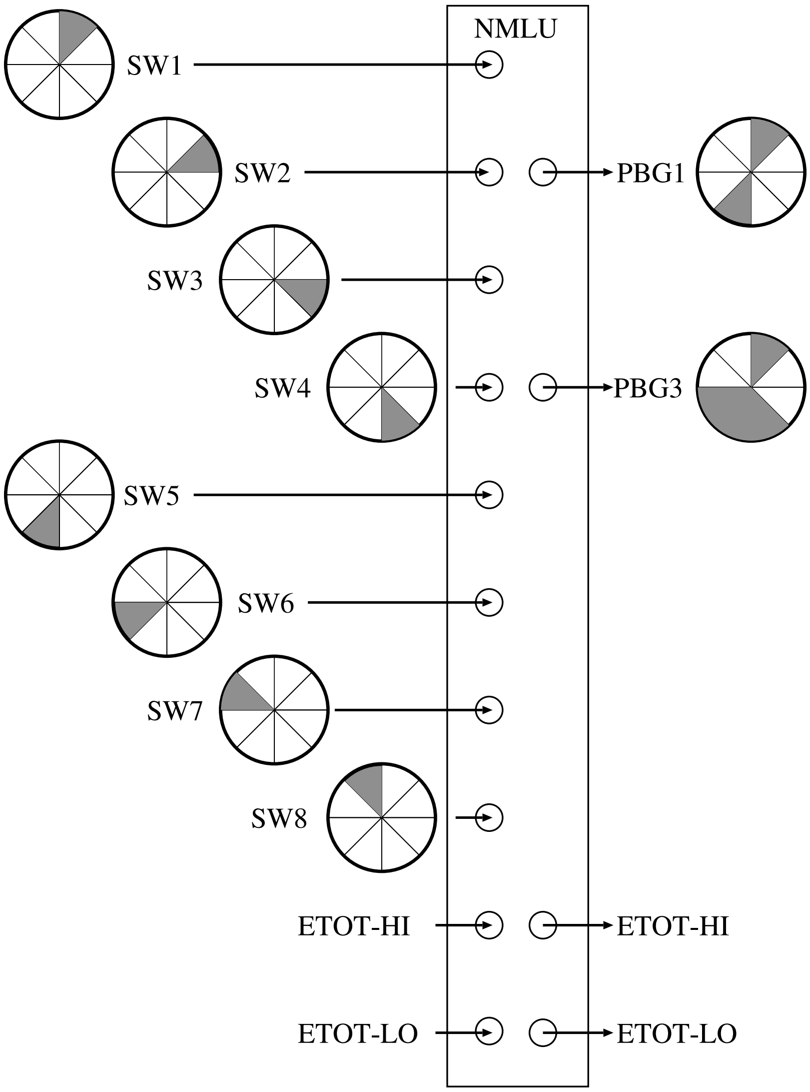

Figure 2.13: The inputs and outputs of the Neutral MLU. The diagrams illustrate the CCAL requirements, i.e. the NMLU input#1 (SW1) requires a hit above threshold in Superwedge 1 (wedges 1-9).

- **Neutral PBG1** - PBG1 $\oplus \overline{\mathrm{H1} \cdot \mathrm{H2}'} \oplus \overline{\mathrm{FCV-OR}}$
- **Neutral ETOT** - ETOT-HI $\oplus \overline{\mathrm{H1} \cdot \mathrm{H2}'} \oplus \overline{\mathrm{FCV-OR}}$
- **ETOT-NOVETO** - ETOT-HI $\oplus \overline{\mathrm{H2} \geq 2}$
- **ETOT-LO** - ETOT-LO $\oplus \overline{\mathrm{H1} \cdot \mathrm{H2}'} \oplus \overline{\mathrm{FCV-OR}}$

The MMLU outputs are sent to the gatemaster, four of 16 possible triggers, or reasons to readout the detector electronics. These are listed in table 2.6. The gatemaster checks that the none of the DYCs are busy, and then sends out a signal to the readout electronics to record the event. The time at which this signal is sent determines the window used by the FERA to integrate as well as the reference point of the TDC. The MLU strobe is used to determine this time. The signals entering the level 2 summers are passed through to the Minimum Bias discriminator, where a threshold roughly equivalent to 100 MeV is implemented. The MLU strobe is triggered by the second above threshold from the Minimum Bias discriminator, and represents the time of the second energy deposit that appears in the CCAL.

Many of the gatemaster inputs are designed to measure efficiencies. The ETOT-NOVETO data is prescaled so that only a small percentage, typically 1%, of these triggers are sent to the gatemaster. One use of the data is to study photon conversions in the beam pipe, discussed in appendix C. The ETOT-LO data are similarly prescaled, and used to check the efficiency of the ETOT-HI trigger. The laser trigger is used for monitoring the CCAL, as described in chapter 3. The Minimum Bias trigger is a pass-through of the MLU-strobe, prescaled significantly. The Random Gate trigger is generated with a pulser operating at 1 kHz, and gives information about overlapping events and noise in the detector.

Inputs	
1	PBG1 (NMLU output#1)
2	PBG3 (NMLU output#2)
3	ETOT-HI (NMLU output#3)
4	ETOT-LO (NMLU output#4)
5	H1 $\cdot$ H2$'$-OR
6	FCAL-OR
7	H2>2
8	FCV-OR
9	CMLU Output#1
10	CMLU Output#2
11	CMLU Output#3
12	CMLU Output#4
13	CMLU Output#5
14	PMLU Output#1
15	PMLU Output#2
16	PMLU Output#3
Outputs	
1	e^+e^-
2	$\overline{p}p90°$
3	$\phi\phi$
4	Neutral PBG1
5	Neutral ETOT
6	$\overline{p}p$ control (55°)
7	ETOT-NOVETO
8	ETOT-LO

Table 2.2: The Master MLU inputs and outputs.

GM#	Description	PRUDE Analysis	Priority	Output Stream
1	e^+e^-	e^+e^-	11	GK
2	$\overline{p}p$ 90°	autopass	8	GP
3	$\phi\phi$	$\phi\phi$	12	GP
4	Neutral PBG1	neutral	13	GN
5	Neutral ETOT	neutral	14	GN
6	$\overline{p}p$ control (55°)	autopass	9	GP
7	ETOT-NOVETO	autopass	4	GK
8	ETOT-LO	autopass	6	GK
9	CCAL Laser	autopass	1	GK
10	Silicon Strobe	autopass	10	GP
11	ALL			
12	Minimum Bias	autopass	2	GK
13	Random Gate	autopass	3	GK
14	FCAL Cosmic	autopass	5	GK
15	High Rate Minimum Bias	autopass	7	GP
16	empty			

Table 2.3: The gatemaster inputs and their descriptions.

2.7 Online filter

The online filter, named PRUDE(Program Rejecting Unwanted Data Events), is a software program that reduces the data rate from $\sim$ 2 kHz to $\sim$ 500 Hz (on average). 4 identical versions of the filter run in parallel on the Challenge. During the run, each utilized 40% of the CPU on its processor. Events are assigned a single trigger based upon the priority list given in table 2.6, and the gatemaster hits, which are recorded by a TDC module. Channel 11 is the OR of all the inputs, used for counting purposes. Some of the triggers have low enough rates to be passed through the filter automatically (autopass). For the triggers requiring filtering, PRUDE was programmed to automatically pass a fraction of each trigger for later efficiency studies. The triggers requiring filtering are divided into three categories, each with its own set of analysis cuts: e^+e^-, neutral and $\phi\phi$. The triggers and the associated filter are listed in table 2.6.

The neutral analysis is described in detail since this is the path of the $\overline{c}c \to \gamma\gamma$ events. A simplified version of the CCAL clusterizer described in section 3.4 is used by PRUDE to form invariant mass pairs. The filter selects events with $\overline{c}c$, η, and π^0 candidates, as well as the events with 90% of the reconstructed energy in the CCAL. The filter duplicates a subset of data as the gold stream, a purified sample of charmonium data written to disk for quick analysis. For a neutral event to qualify for the gold stream, the invariant mass of the two highest energy clusters is required to be greater than 2.7[2.5] MeV above[below] transition. Events with π^0 or η candidates are duplicated in the GNA stream, which is used for CCAL calibration.

Chapter 3

Central Calorimeter

The Central Calorimeter (CCAL) is a cylindrical array of 1280 lead glass Cherenkov counters, segmented both in θ and ϕ, which measures the energy and position of electromagnetic showers. It is F2-type lead glass, which has radiation length of 3.141 cm and a density of 3.61 g/cm^3. Each counter points toward the interaction region in a projective geometry. A *ring* in θ contains 64 counters, and a *wedge* in ϕ contains 20 counters. Figure 3.1 is a slice of the CCAL in ϕ, showing the layout of the counters in each wedge. The CCAL coverage in θ is restricted in the backward (large θ) region by the physical presence of the gas-jet pumping system. The region of small θ is covered by the forward calorimeter.

The granularity of the counters is a compromise between the desire to resolve the two photons from a symmetric π^0 decay and both the energy resolution (since the additional support structure decreases the resolution) and the increased cost of producing more blocks. The thickness of blocks ranges between 12 and 16 radiation lengths. At this thickness, the counters contain only $90 - 95\%$ of the highest energy shower. Longer blocks would give full containment, but increase the light transmission losses for the lowest energy clusters. Since detection of low energy photons is crucial for background reduction for the $\gamma\gamma$ final states, total containment of the highest energy showers was compromised. The dimensions and positions of the individual counters are presented in table 3.1.

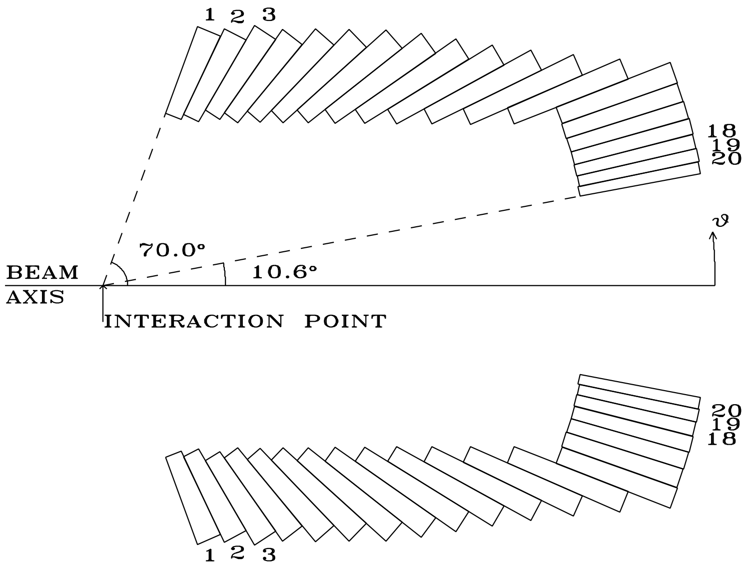

Figure 3.1: A side view of the Central Calorimeter (CCAL).

3.1 Resolution

The average position resolution determined in E760 was 9 mm, corresponding to 6 mrad in θ, 11 mrad in ϕ [30] and energy resolution [16] given by the formula

$$\frac{\sigma(E)}{E} = \frac{6.0\%}{\sqrt{E(\mathrm{GeV})}} + 1.4\% \tag{3.1}$$

Although a remeasurement of these resolutions is desirable for E835, it requires an *a priori* knowledge of the position and energy of particles. The inner tracking detectors cannot provide sufficient position resolution to do this. Instead, it can be shown that the resolution numbers from E760 are reasonable for E835 as well by using e^+e^- decays of the J/ψ. Clean events are selected with the hodoscopes and the Čerenkov.

Block Number	Block Length (cm)	Central θ (deg)	Block Width (deg)	Distance from Target (cm)	PMT Diameter (inches)	Fractional PMT Coverage
01	37.80	67.387	5.226	72.44	3.0	0.473
02	38.65	62.259	5.031	75.87	3.0	0.475
03	39.88	57.342	4.803	80.07	3.0	0.476
04	41.50	52.664	4.552	85.08	3.0	0.478
05	43.54	48.246	4.284	90.96	3.0	0.479
06	46.03	44.101	4.007	97.79	3.0	0.481
07	48.98	40.234	3.728	105.62	3.0	0.482
08	50.00	36.644	3.451	114.54	3.0	0.497
09	50.00	33.327	3.183	124.66	3.0	0.520
10	50.00	30.273	2.925	136.07	3.0	0.544
11	50.00	27.472	2.679	148.89	3.0	0.568
12	50.00	24.908	2.449	163.26	3.0	0.593
13	50.00	22.567	2.233	179.34	3.0	0.617
14	50.00	20.434	2.033	197.28	3.0	0.641
15	50.00	18.493	1.848	197.29	2.5	0.546
16	50.00	16.730	1.678	197.29	2.5	0.664
17	50.00	15.130	1.522	197.30	2.0	0.527
18	50.00	13.679	1.380	197.30	2.0	0.644
19	50.00	12.364	1.250	197.30	1.5	0.443
20	50.00	11.174	1.131	197.30	1.5	0.543

Table 3.1: Dimensions, positions and photomultiplier characteristics of the 20 lead-glass blocks within each of the 64 CCAL wedges.

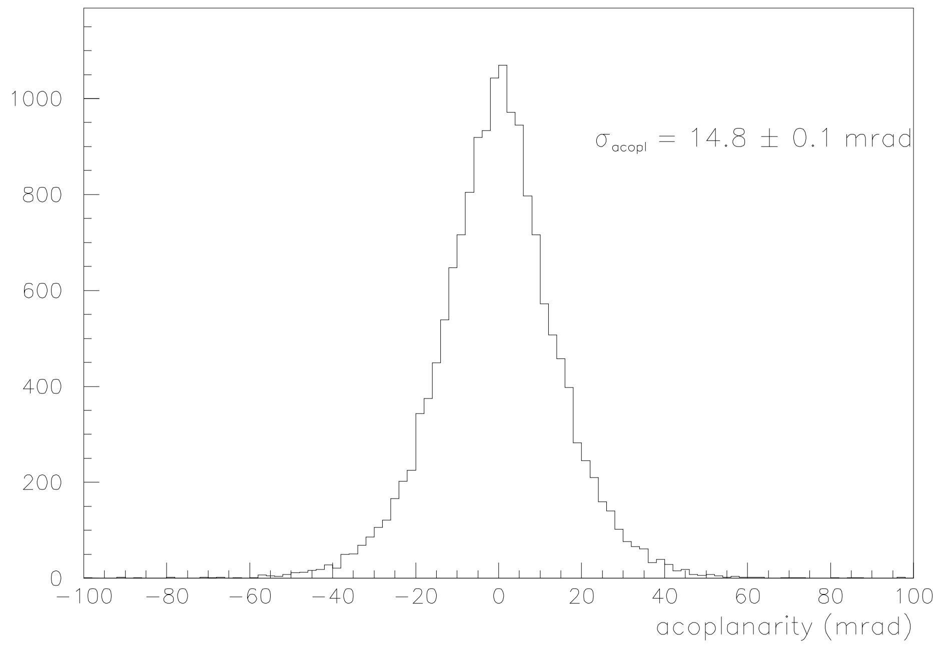

Figure 3.2: Acoplanarity ($\Delta\phi$) distribution for clean $J/\psi \rightarrow e^+e^-$ decays.

The quantity $\Delta\phi \equiv \pi - |\phi_1 - \phi_2|$ measures the deviation from two-body kinematics in the azimuthal plane. For a resolution $\sigma_\phi = 11$ mrad, a value of $\sigma_{\Delta\phi} = \sqrt{2}\sigma_\phi =$ 15.6 mrad is expected. The distribution of the variable $\Delta\phi$ is shown in figure 3.2, with $\sigma_{\Delta\phi} = 14.8$ mrad. Using a similar approach for θ , the quantity $\Delta\theta = \theta_{1,pred} - \theta_{1,meas}$ is considered, where $\theta_{1,pred}$ is calculated from $\theta_{2,meas}$ assuming two-body kinematics. The expected value for $\sigma_{\Delta\theta}$ is a function of θ, shown in figure 3.3 for $\sigma_\theta = 6$ mrad together with the $\sigma_{\Delta\theta}$ of the e^+e^- data. These comparisons confirm that the angular resolution has not changed from what was measured in E760.

Finally, the energy of the electrons and positrons can be predicted from two body kinematics using the angle θ measured by the CCAL. In figure 3.4, the quantity $(E_{pred} - E_{meas})/E_{meas}$ is plotted for J/ψ data. The result of the Gaussian fit,

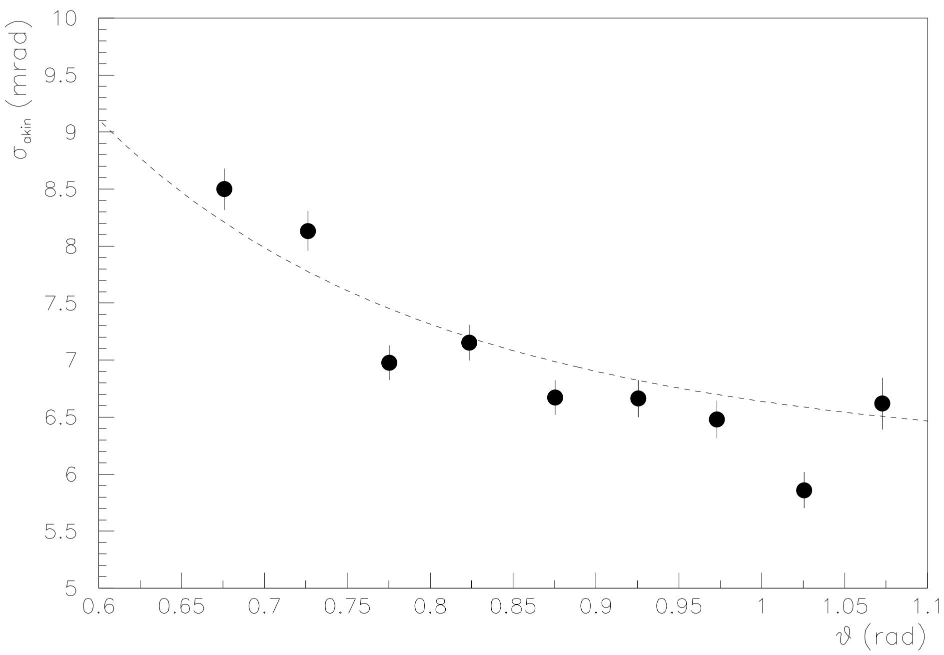

Figure 3.3: Akinematics ($\Delta\theta$) standard deviation is plotted as a function of θ for clean $J/\psi \to e^+e^-$ decays. The curve is the expected $\sigma_{\Delta\theta}$ for a resolution $\sigma_\theta = 6$ mrad.

$\sigma = 3.8\%$, is consistent with E760, and the RMS value of 5.3% for an average electron energy of 2.5 GeV is consistent with equation 3.1.

3.2 Monitoring System

For monitoring and testing purposes, a network of plastic polymer fiber optic cables transmit light the back of each lead glass block. The xenon flash lamp used in E760 was replaced with a nitrogen laser for E835. The laser produces 3 ns pulses of light with wavelength 337.1 nm. This light pulse is pointed at a piece of scintillator that produces light with wavelength ≈ 430 nm. The scintillator is needed since the fiber optic cable does not transmit ultraviolet light efficiently. The light then enters a

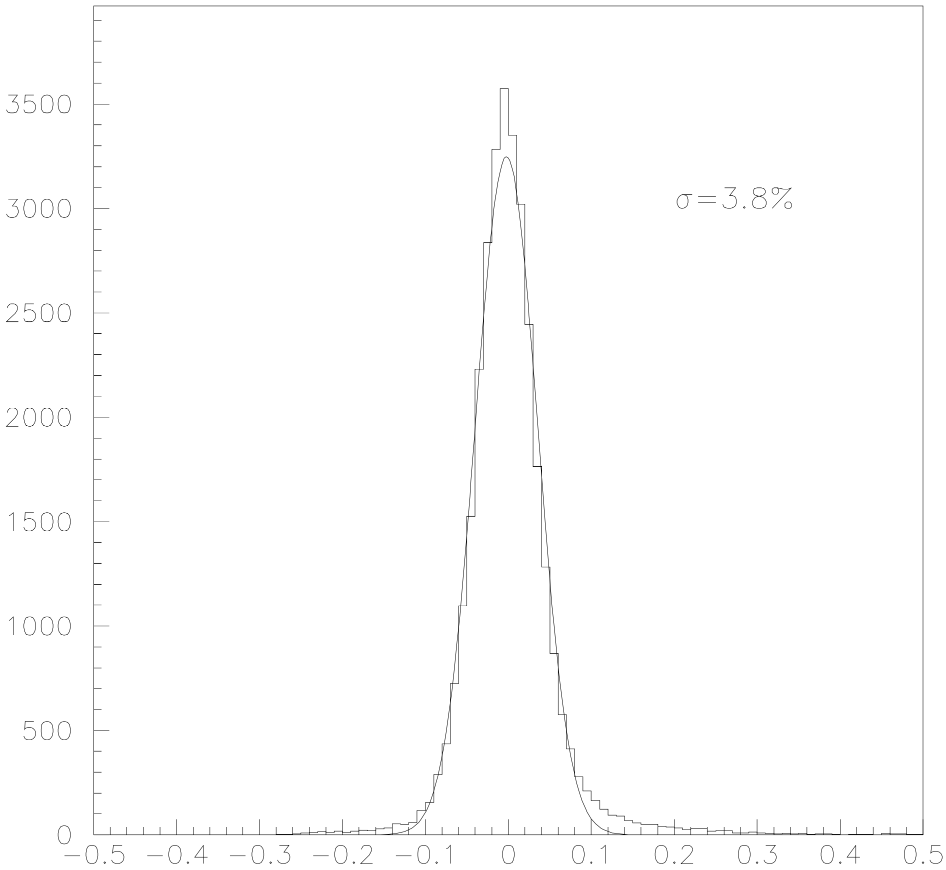

Figure 3.4: The difference between the measured and predicted energies for the decay particles from $J/\psi \to e^+e^-$ decays.

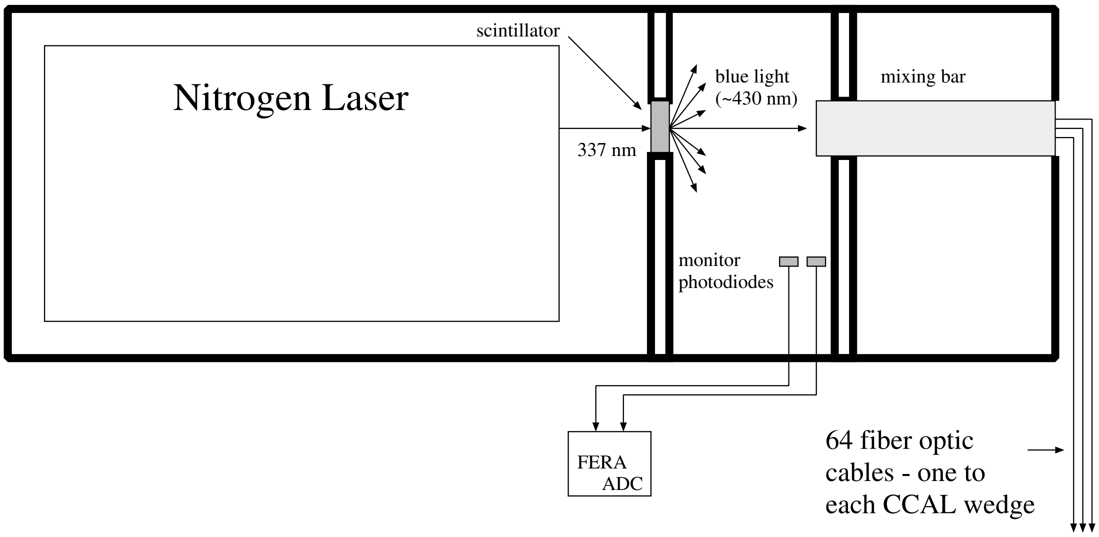

Figure 3.5: Layout of the aluminum laser box containing the laser, the scintillator, and the major mixing bar.

rectangular lucite mixing bar and is uniformly distributed over the fiber optic cables at the other end. These cables provide a light path to each wedge of the CCAL. Inside the wedge, the light encounters a secondary mixing bar which further distributes the light over twenty more fibers, one attached to the back of each block in the wedge. A light-tight aluminum box holds the laser, the scintillator, the major mixing bar and two PIN diodes, as shown in figure 3.5. The diodes measure the intensity of the individual laser pulses. This system was indispensable for testing the CCAL counters, prior to and during the data taking, and was also used to monitor the gain of the counters.

3.3 Readout Electronics

To allow enough time for the trigger to make a decision about an event, the signals from the CCAL are delayed with over 300 ns of coaxial cable between the trigger electronics and the readout electronics. Unfortunately, the cable performs a

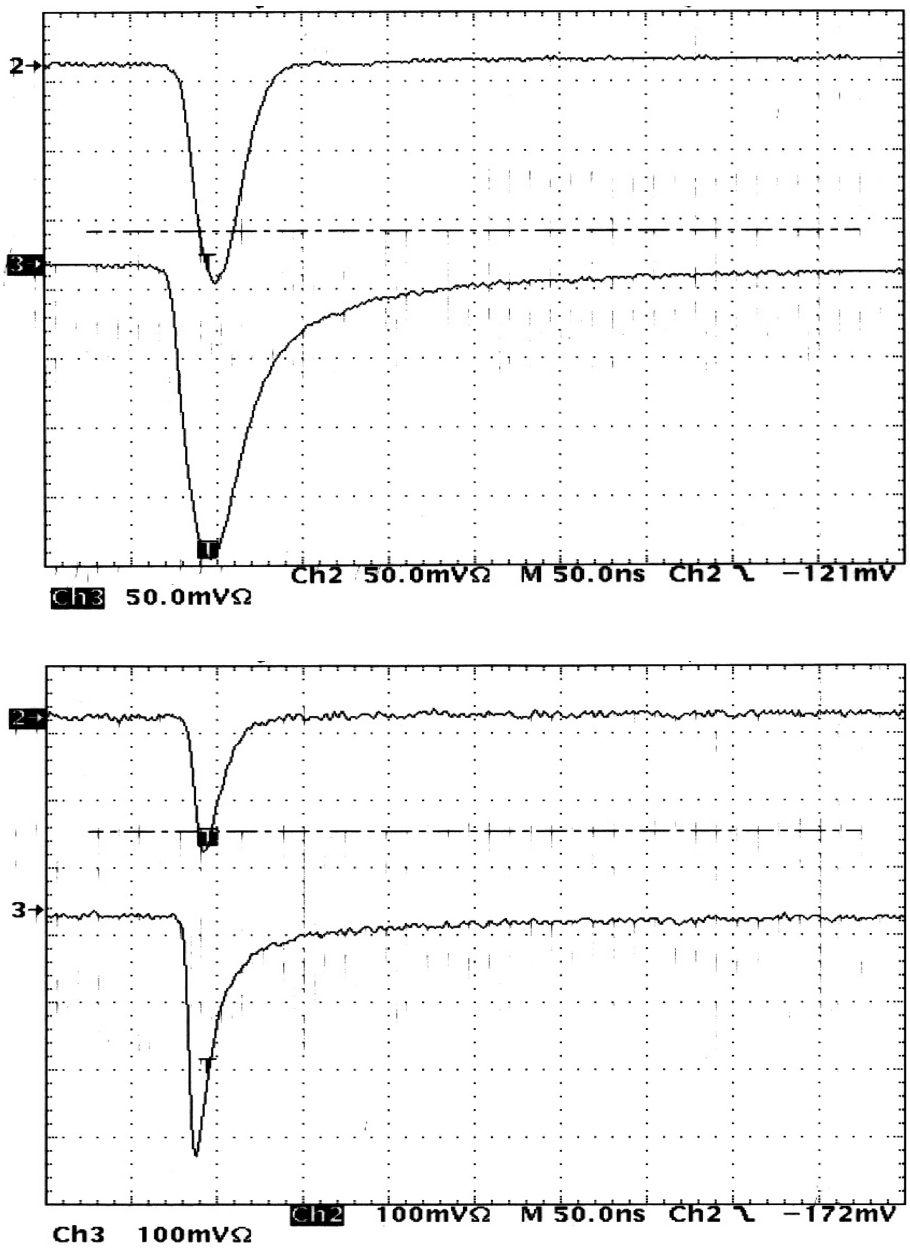

Figure 3.6: Oscilloscope trace showing the input (Ch3) and output (Ch2) of the shaper circuit for a $\sim$ 1 GeV pulse from a 3-inch PMT in ring 10 (above) and a 2-inch PMT in ring 17 (below). The pulses are from beam interactions, with the same electronics chain used during data taking.

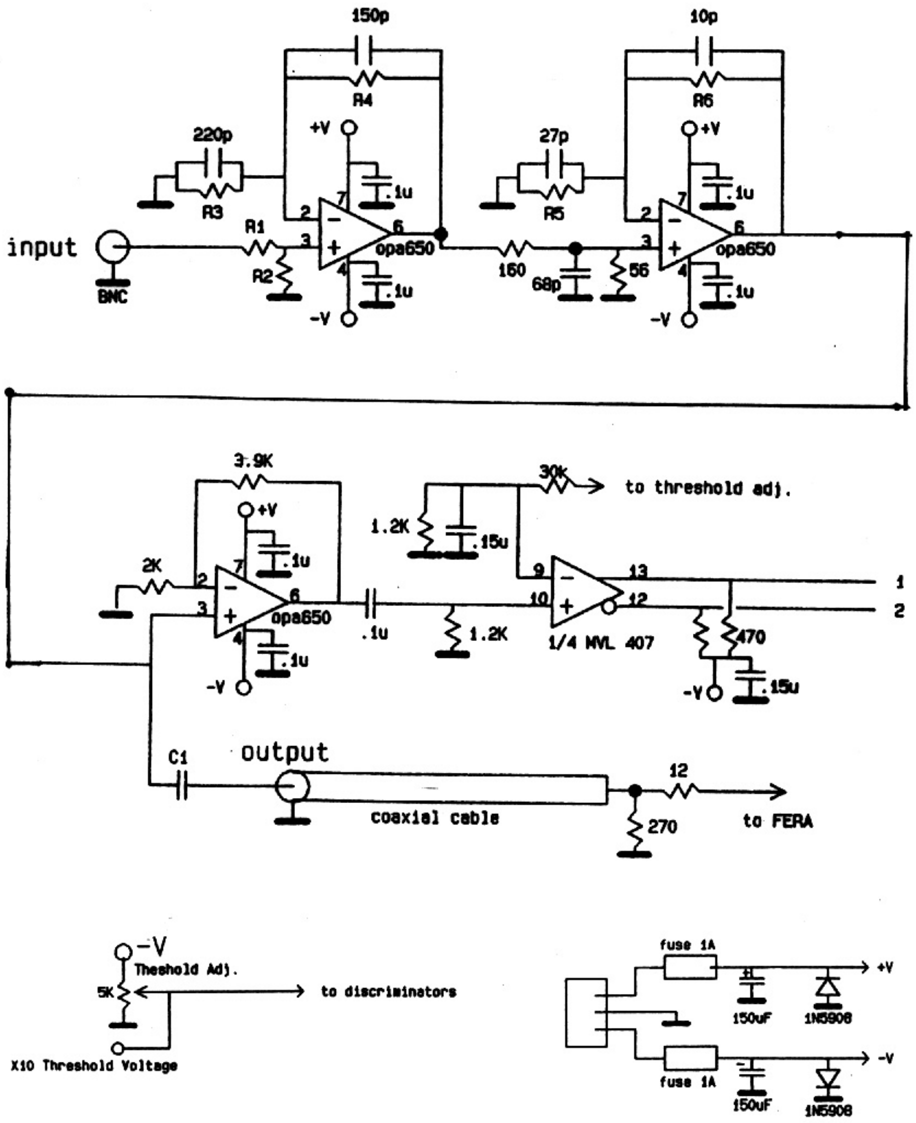

Tube diameter		R1	R2	R3	R4	R5	R6	C1
(3")	1	24	27	1.2K	1.0K	1.3K	1.3K	22nF
(2")	2	30	20	1.2K	680	820	1.5K	22nF
(1.5")	3	30	18	910	680	680	1.5K	18nF

Figure 3.7: A circuit diagram of the shaper. Only one of the 16 channels is shown, along with the potentiometer that controls the discriminator threshold for all 16 channels and the power connection.

frequency-dependent attenuation of the signal, extending the tail of the pulses for over 600 ns. In E760, the tails of earlier pulses appeared as extra clusters in the triggering event. With the increase of rate projected for E835, this contamination would have been detrimental to the data quality, especially for the $\gamma\gamma$ final states.

Added to the simple ADC readout of E760 is a passive filter, designed to re-shape the pulses from the CCAL. The filter also discriminates the pulses for timing purposes. There are three versions of the *shaper* circuit, since the pulses coming from the smaller PMTs (rings 17-20) are significantly different. Figure 3.6 displays oscilloscope traces of the input and the output of the shaper for two of the three different size PMTs. Each shaper circuit board has 16 channels; the diagram for a single channel is shown in figure 3.7. The circuit replaced a simple voltage divider with a gain of 0.5 used in E760 at the input to the ADC. In the shaper, two voltage dividers set the overall gain of the circuit equivalent to the 0.5 of E760. By narrowing the pulses, the same amount of charge is collected in a 100 ns ADC gate as E760 collected in a 150 ns gate. The improvements in both gate length and pulse shape allowed E835 to run at three times the instantaneous luminosity of E760 with the same fraction of contaminated events. The addition of timing information allows most of the contamination to be identified and separated from the triggering event.

3.4 Clusterizer

The clusterizer groups neighboring blocks, that are hit, into clusters and assigns a position and energy to each cluster. First, cluster *seeds* are found by identifying local maxima, i.e. blocks with more energy than the eight blocks around them. The cluster seed itself is required to have a minimum energy, known as the *seed threshold.* The summed energy of the cluster seed and the eight surrounding blocks is also required to be above an energy threshold, the *cluster threshold*, which again depends upon the physics analysis being performed. Analyses sensitive to low energy photons use thresholds of 5/20 MeV (seed/cluster) while other analyses use thresholds of 25/50 MeV. A 3x3 grid of blocks, with the seed at the center, forms a cluster. The clusters are classified in one of three categories: isolated, shared, or split. These classifications are summarized here, and the details of calculating the position and energy of each cluster follow.

Isolated clusters do not have a second local maxima in a 5x5 grid around their seed. If there is a second local maxima, the clusters are called shared clusters. The 3x3 grids around each of the two seeds will overlap, and the energy in these overlapping blocks must be shared between the two clusters. The third category, split clusters, is for energy deposits whose centers are so close together that there is not a second local maxima.

At the highest values of s examined by E835, the smallest π^0 opening angle corresponds to approximately 1.5 block widths. With this small opening angle, the two photons often hit two blocks whose corners touch diagonally, and only one local maxima will be found. To look for such occurrences, the *cluster mass*, or M_{cl}, was calculated for every isolated cluster,

$$M_{cl} \equiv \sqrt{\left(\sum_i E_i\right)^2 - \left(\sum_i \vec{p}_i\right)^2} \tag{3.2}$$

where the sum is over the 25 blocks in a 5x5 grid around the seed, E_i is the energy deposited in the ith counter of the cluster and $\vec{p}_i = E_i \hat{r}_i$ where $\hat{r}_i$ is the unit vector from the interaction point to the center of the ith counter. The upper plot of figure 3.8 shows the cluster mass for e^+e^- pairs from J/ψ decay and for clusters formed in π^0 decays. The large peak in the π^0 spectrum represents the coalesced π^0s, where the two photons have merged into a single cluster, and the small peak the isolated photons

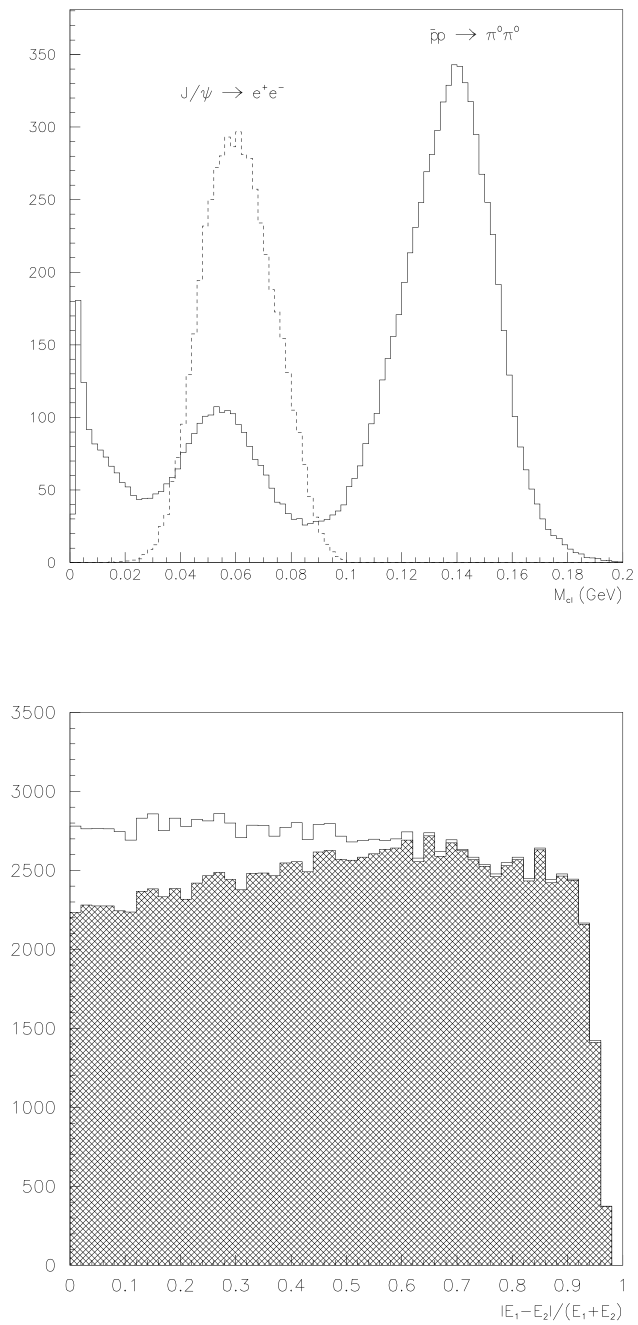

Figure 3.8: M_{cl} is plotted in the upper plot for $\pi^0\pi^0$ events (solid) and e^+e^- decays of the J/ψ (dashed). Below, the π^0 asymmetry $(E_1 - E_2)/(E_1 + E_2)$ is plotted without the split clusters (shaded) and including the split clusters (open).

from asymmetric π^0 decays. A cut was set at $M_{cl} = 100$ MeV to ensure that none of the e^+ or e^- clusters were affected. The lower plot of figure 3.8 demonstrates the π^0 recovery power of the cluster splitting method. The missing events for $asymmetry \approx 1$ contain a low energy photon that is outside the CCAL acceptance or below the CCAL energy threshold. The cluster mass of the split cluster is not recalculated after it has been divided, but is instead defined as the value calculated before splitting.

3.4.1 Isolated Clusters

An isolated cluster is one whose 3x3 grid is not overlapped by the grid of another cluster. The cluster position is first approximated by the energy weighted position average. Defining x as the distance in the θ (wedge) direction from the center of the seed block and y as the distance in the ϕ (ring) direction from the center of the seed block, in units of blocks, the energy weighted position average, (x,y), of the cluster is given by

$$\overline{x} = \sum_{i=1}^{9} \frac{En_i x_i}{En_i} \quad , \quad \overline{y} = \sum_{i=1}^{9} \frac{En_i y_i}{En_i} \tag{3.3}$$

where En_i is the energy deposited in the ith block, $x_i = -1, 0, 1$ is the block center in wedge units, and $y_i = -1, 0, 1$ is the block center in ring units.

The steel partitions between the blocks compose 2% of the surface area of the CCAL in ϕ and 0.5% in θ. Energy from the showers is lost in these *cracks* and corrections to both the position and energy of the shower must be made.

The position of the center of the cluster, (x', y'), is corrected using the equations

$$\begin{aligned} x' &= A_w \left(1 - e^{-\overline{x}/a_w}\right) + B_w \left(1 - e^{-\overline{x}/b_w}\right) \\ y' &= A_r \left(1 - e^{-\overline{y}/a_r}\right) + B_r \left(1 - e^{-\overline{y}/b_r}\right) \end{aligned} \tag{3.4}$$

where $x'(y')$ is the distance in the wedge(ring) direction, in block units, from the

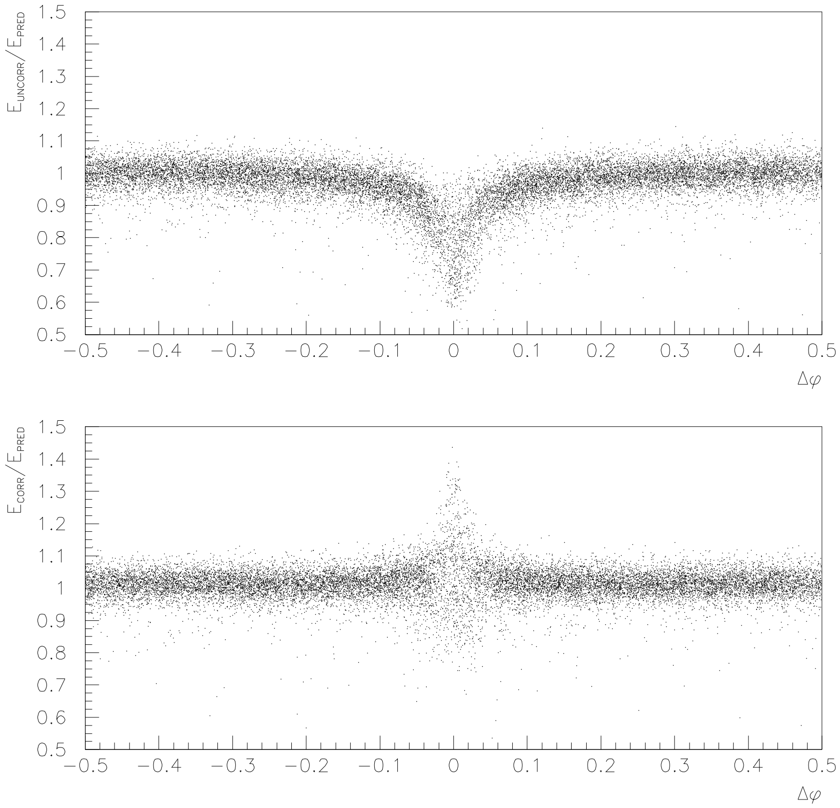

Figure 3.9: The ratio between the predicted and measured cluster energies for $J/\psi \to e^+e^-$ decays is plotted as a function of the distance from the crack (in block units).

center of the block. The functional form and the constants were both determined empirically with e^+e^- decays of the J/ψ in E760[47]. The constants are listed in table 3.2.

The corrected cluster energy is given by the equation

$$\begin{aligned} E &= f_{corr} E_{sum} \\ &= \frac{E_{sum}}{\left(1 - C_{high(low)} e^{-|x^*|/c_{high(low)}}\right)\left(1 - D_1 e^{-|y^*|/d_1} - D_2 e^{-|y^*|/d_2}\right)} \end{aligned} \tag{3.5}$$

where x^*, y^* are the distances from the closest edges of the block. Since the rings'

A_r	724.4	a_r	0.03208
A_w	706.5	a_w	0.03969
B_r	123.6	b_r	0.1860
B_w	102.6	b_w	0.1715
C_{low}	0.0614	c_{low}	7.367
C_{high}	0.0857	c_{high}	19.690
D_1	0.14736	d_1	48.908
D_2	0.15935	d_2	12.761

Table 3.2: Constants used in calculating the position and energy of CCAL showers.

faces are staggered, (see figure 3.1), different parameters are used for the high and low θ edges of the block. The values of the constants are listed in table 3.2. The energy of the final particles in the decay $J/\psi \to e^+e^-$ can be predicted from the measured values of θ. For these decays, figure 3.9 shows the ratio between the predicted and measured cluster energies, as a function of the distance from the crack, before and after the correction for crack losses. The energy resolution near the crack is worse than the rest of the block, and is discussed later in this chapter.

3.4.2 Shared Clusters

If there are two clusters whose 3x3 grids overlap, then the energy in the overlapping blocks is divided between the two clusters. The sharing is an iterative process, where the fraction of energy, $f_{i,m}$, in each shared block (denoted i) due to each cluster (denoted m) is calculated at each iteration, using the positions and energies of the two clusters from the previous iteration. The process is outlined below:

1. The initial cluster positions and energies are calculated assuming the clusters are isolated (the energy in the overlapping blocks is counted twice). The energy weighted position average is calculated and a correction for the crack losses is made to the positions and energies using equations 3.4 and 3.6.

2. The initial cluster positions and energies are then used to calculate $f_{i,m}$, the fraction of the total energy in block i that comes from cluster m, with the equation

$$f_{i,m} = \frac{E_m e^{-(|\delta x_{im}|+|\delta y_{im}|)/0.17}}{E_1 e^{-(|\delta x_{i1}|+|\delta y_{i1}|)/0.17} + E_2 e^{-(|\delta x_{i2}|+|\delta y_{i2}|)/0.17}} \tag{3.6}$$

where $f_{i,m} = 0$ if block i is not a part of the 3x3 grid for cluster m. E_m is the total energy of cluster m and the distance $\delta x_{im}(\delta y_{im})$ is measured along the ring(wedge) axis from the middle of block i to the center of cluster m. The form of this equation reflects the assumption that the energy deposited decreases exponentially with the distance from the cluster center along each axis. The factor of 0.17 in the exponent is determined empirically with $J/\psi \to e^+e^-$ events.

3. With the values of $f_{i,1}$ and $f_{i,2}$, the cluster positions and energies are re-calculated with an extension of equation 3.3

$$\overline{x_m} = \sum_{i=1}^{9} \frac{f_{i,m} En_i x_i}{f_{i,m} En_i} \quad , \quad \overline{y_m} = \sum_{i=1}^{9} \frac{f_{i,m} En_i y_i}{f_{i,m} En_i}$$
$$E_{sum,m} = \sum_{i=1}^{9} f_{i,m} En_i \quad , \quad m = 1, 2 \tag{3.7}$$

followed by the correction for crack losses.

4. These new positions and energies replace the initial ones, and the process is redone beginning at step 2.

Convergence is obtained when the following conditions are satisfied: the energy of both clusters changes by less than 30 MeV, and the θ and ϕ equivalent values for the cluster positions of both clusters all change by less than 5 mrad each. The whole process typically requires 2-4 iterations to converge, and it is terminated if it has not converged by the 10th iteration, retaining the values of the last iteration.

3.4.3 Split Clusters

Any cluster with $M_{cl} > 100$ MeV, that is not shared, is split into two clusters by identifying a second cluster center. The second center is chosen from the four corners of the 3x3 grid around the original cluster center by selecting the one with the largest energy. With the large overlap of the two showers, calculating the $f_{i,m}$ is more difficult. The sharing algorithm is modified by increasing the grid for each cluster from 3x3 to 5x5 and NOT sharing the energy in one cluster's center with the other cluster. Since the tail on one side of each cluster is hidden by the center of the second cluster, the enlarged grid maximizes the information from the visible portion of the tail. The iterations then proceed as in the case of shared clusters, outlined below.

1. The initial position for the two clusters is calculated with the energy weighted position average, using the 5x5 grid around the center and excluding the center of the other cluster. The corrections for the crack losses are computed with equations 3.4 and 3.6.

2. The initial cluster positions and energies are then used to calculate $f_{i,m}$, the fraction of the total energy in block i that comes from cluster m, with the equation

$$f_{i,m} = \frac{E_m e^{-(|\delta x_{im}|+|\delta y_{im}|)/0.17}}{E_1 e^{-(|\delta x_{i1}|+|\delta y_{i1}|)/0.17} + E_2 e^{-(|\delta x_{i2}|+|\delta y_{i2}|)/0.17}} \tag{3.8}$$

$$f_{i,1} = f_{j,2} \equiv 1 \qquad i = \text{center of cluster 1}$$

$$f_{j,1} = f_{i,2} \equiv 0 \qquad j = \text{center of cluster 2}$$

where $f_{i,m} = 0$ if block i is not a part of the 5x5 grid around the center clock of cluster m. E_m is the total energy of cluster m and the distance $\delta x_{im}(\delta y_{im})$

is measured along the ring(wedge) axis from the middle of block i to the center of cluster m. The energy in either cluster center is not shared for any iteration.

3. With the values of $f_{i,1}$ and $f_{i,2}$, the cluster positions and energies are recalculated with an extension of equation 3.3

$$\overline{x_m} = \sum_{i=1}^{25} \frac{f_{i,m} En_i x_i}{f_{i,m} En_i} \quad , \quad \overline{y_m} = \sum_{i=1}^{25} \frac{f_{i,m} En_i y_i}{f_{i,m} En_i}$$
$$E_{sum,m} = \sum_{i=1}^{25} f_{i,m} En_i \quad , \quad m = 1,2 \tag{3.9}$$

The corrections for crack losses are then applied to get the new positions and energies.

4. These new positions and energies replace the initial ones, and the process is redone beginning at step 2 until the process converges. The requirements for convergence are the same as for the shared clusters.

The separation of the two clusters is slightly overestimated by this process because the cluster centers are not shared. Thus, the calculated invariant mass for a split π^0 is slightly too large. For the results discussed in chapter 6, identifying the π^0s is crucial for background rejection. The invariant mass of two cluster is used to identify π^0s, except in the case of split clusters where the large cluster mass is sufficient for identification, and the actual cluster positions of the split clusters are not used.

3.4.4 Errors on Cluster Parameters

In section 3.1, the average resolution of the CCAL is described. Since the cracks in the CCAL affect the resolutions, the errors on both the measured position and the measured energy for an individual cluster depend upon how close to a crack the particle hit. The errors are calculated with the same algorithm for shared, split and isolated clusters.

If a cluster contains only one CCAL block, the position resolution is three-tenths of the block size. Additional blocks in the cluster improve the position resolution. In this case, the position resolution is parameterized as $\sigma_x = a + b\delta x$, where δx is the distance from the edge of the block to the cluster center of gravity (the assumed incidence point of the particle). The first term represents the intrinsic resolution in the glass, PMT, and electronics combined; the second represents the granularity. Applied to the two transverse dimensions of the cluster, the errors of the measured angular position are written

$$\sigma_\theta = \frac{\sigma_x}{R} = \frac{a_x + b_x\delta x}{R} \tag{3.10}$$

$$\sigma_\phi = \frac{\sigma_y}{R\sin\theta} = \frac{a_y + b_y\delta y}{R\sin\theta} \tag{3.11}$$

where R is the distance from the interaction point to the cluster center of gravity, and the variables x, y measure the horizontal and vertical distances across the face of a block.

The constants a_x, b_x, a_y, b_y were determined empirically with data during E760 [47], with the following results

$$\begin{aligned}\sigma_\theta &= (46.4 + 0.2 \times \delta x) \times \frac{1}{R} \\ &= (3.40 + 1.51 \times \delta x) \times \frac{136.42}{R} \qquad (3.12)\\ \sigma_\phi &= (46.5 + 0.2 \times \delta y) \times \frac{1}{R\sin\theta} \\ &= (5.90 + 2.62 \times \delta y) \times \frac{78.74}{R\sin\theta} \qquad (3.13)\end{aligned}$$

where the lengths are in cm and the angles in mrad. The values 136.42 cm and 78.74 cm represent the average values for R and $R\sin\theta$ over rings 1 to 14. It is not surprising that the position resolution is the same in either direction ($a_x = a_y$ and $b_x = b_y$) since the blocks are essentially square. The value of $R\sin\theta$ is almost a constant for all 20 rings, so the cluster errors in ϕ have a constant mean of 11 mrad, and range ± 3 mrad within a single block. In θ, the error depends upon the distance of the block from the interaction region as well as the position within the block. This results in a mean error which changes from 9 to 3 mrad as the distance increases, and the spread within a block is approximately half of the mean.

The error on the cluster energy follows the form in equation 3.1 on average, but for each individual cluster, the relative size of the crack correction is also considered. The error is calculated as follows

$$\sigma_E = 0.05\sqrt{E} + 0.3(f_{corr} - 1)E + 0.005 \tag{3.14}$$

where E is the corrected energy, $E_{corr} = f_{corr}E_{meas}$. The constants in the first two terms were determined with an empirical fit to the $J/\psi \rightarrow e^+e^-$ data; and the last term is added to allow for pedestal fluctuations of 1-2 ADC counts. The errors on the measured positions and energies of the CCAL clusters are used for kinematical fitting in the analysis. This is discussed in more detail in section 5.1.

3.5 Calibration

The *gain* of a CCAL channel is the conversion factor from ADC counts to energy. In E835, the gain of each channel is calculated for every stack, using $\pi^0\pi^0$ events. The events are selected with the kinematical cuts detailed in Appendix B. These cuts depend weakly on the energy calibration.

Ideally, the energy of each π^0 can be predicted from quantities independent of the measured energy, and then compared with the measured ADC counts to determine the gain of each channel. The energy of each π^0, E_j, can be calculated from its angles and two body kinematics. However, calculating the angles of the π^0 requires both the measured energy and angles of the two decay photons. Even though the use of the measured energy of the photons is minimized in the calculation of the π^0 angles, the measured angles of the π^0 depend weakly on the gain constants, $\{g_i\}$.

This dependence can alter the final values for the $\{g_i\}$ if the initial gain constants are more than $10-20\%$ different than their true values. Large changes ($\geq 5\%$) are possible after a long shutdown, or when the high voltage settings of the PMTs are changed, or when one or more cards (16 channels) of the readout electronics are changed. Large changes are confirmed (or sometimes discovered) with the monitoring system before calibrating. When such changes in the gains were foreseen, a second iteration of the event selection, followed by a second iteration of the calculation of the gain constants (described below) is performed.

The momentum of a photon is the cluster energy times the unit vector from the center of the interaction region to the center of gravity of the cluster. The angles of the π^0 are obtained from the momenta of the photons

$$\begin{aligned} \tan\theta &= \frac{\sqrt{(P_{x,1}+P_{x,2})^2+(P_{y,1}+P_{y,2})^2}}{P_{z,1}+P_{z,2}} \\ \tan\phi &= \frac{P_{x,1}+P_{x,2}}{P_{y,1}+P_{y,2}} \end{aligned} \tag{3.15}$$

where $P_{x,i}(P_{y,i},P_{z,i})$ is the x(y,z) component of the momentum vector for the two photons ($i=1,2$). The energy of the π^0 is then calculated from its polar angle and the center-of-mass energy (E_{cm})

$$\begin{aligned} E_{\pi^0} &= \frac{E_{cm}(1+A\beta\cos\theta)}{2\gamma(1-\beta^2\cos^2\theta)} \\ A^2 &\equiv 1-\frac{4\gamma^2 m_\pi^2(1-\beta^2\cos^2\theta)}{E_{cm}^2} \end{aligned} \tag{3.16}$$

where γ,β are the parameters of the Lorentz boost to the center-of-momentum frame.

All the counters belonging to the clusters of both decay photons are summed to obtain the measured π^0 energy, M_j

$$M_j = \sum_{i=1}^{n} g_i A_{ij} \tag{3.17}$$

where n is the number of blocks associated with the jth π^0 and A_{ij} is the ADC counts recorded for the ith block in the jth π^0.

The g_i are then found by an iterative χ^2 minimization procedure. χ^2 is defined as follows

$$\chi^2 \equiv \sum_{j=1}^{N} \frac{\left(M_j - E_j\right)^2}{\sigma_j^2} \tag{3.18}$$

where E_j is the predicted energy of the π^0, calculated from the θ of the π^0; σ_j is the estimated rms uncertainty in the predicted energy E_j; and N is the number of π^0s. The set of g_k that minimizes χ^2 is found with the equation

$$g_k = \frac{\sum_{j=1}^{N} \left(\frac{A_{kj}}{\sigma_j^2}\right) \left[E_j - \sum_{i=1, i\neq k}^{n} A_{ij} g_i\right]}{\sum_{j=1}^{N} \frac{A_{kj}^2}{\sigma_j^2}} \tag{3.19}$$

where $A_{kj} \equiv 0$ if $A_{kj} < 300$ ADC counts. In other words, if the *kth* block of the *jth* cluster has less than 300 ADC counts, the *jth* cluster is not included in the determination of the gain constant g_k. The ADC values are restricted this way to ensure that the counters are linear in the ADC region where the gain constants are determined and minimizes the affects of low energy fluctuations in the signals. As a consequence of the ADC restriction, the process must be iterated and the resulting values of the gain constants are slightly overestimated.

The set of g_k determined with equation 3.19 are then used to recalculate the g_k with equation 3.19, and the procedure iterated until the gains converge. The overestimate due to the ADC threshold is corrected by scaling the g_k by the ratio between the actual and measured η mass. This correction is typically $1 - 2\%$. Thue, the measured η mass is forced to match the known value, and the measured π^0 mass is used to check the procedure. The measured mass agrees with the known π^0 mass, within errors, for all stacks.

Since the number of π^0s that leave more than 300 ADC counts in the *kth* block, N_k, depends upon both the integrated luminosity and the center of mass energy of each stack, N_k is required to be greater than 15 for the new value of g_i to replace the previous one for a particular block. For 1 pb^{-1} of integrated luminosity above transition, the average value of N_k for each ring varies from 15 to 120, with the angular distribution of the $\pi^0\pi^0$ decays. Below transition, 500 nb^{-1} of data gives a range of N_k from 50 to 400. The g_i are determined to $\sim$ 2% with the minimum number of events.

3.6 Vertex determination

The pointing geometry of the CCAL assumes an ideal vertex. This point in space was defined to be (x,y)=(0,0) and the location of the center of the jet to be z=0. This point, the direction of the beam (the z axis), and the center of the counters in wedge 1 of the CCAL (the x-axis) define the laboratory coordinate system. The interaction region is defined in the xy-plane by the position of the beam and fixed in yz-plane by the gas jet. While the jet location did not change, changes in the beam position from stack to stack were unavoidable.

The measured angles of a particle are determined from the unit vector connecting the center of the interaction region and the center of gravity of the cluster. Thus, there is a small smear in the angles due to the size of the interaction region, $\sim 5 \times 7 \times 7$ mm, however this much smaller than the angular resolution of the CCAL and can be neglected. However, the displacement of the vertex from the ideal position at $(0, 0)$

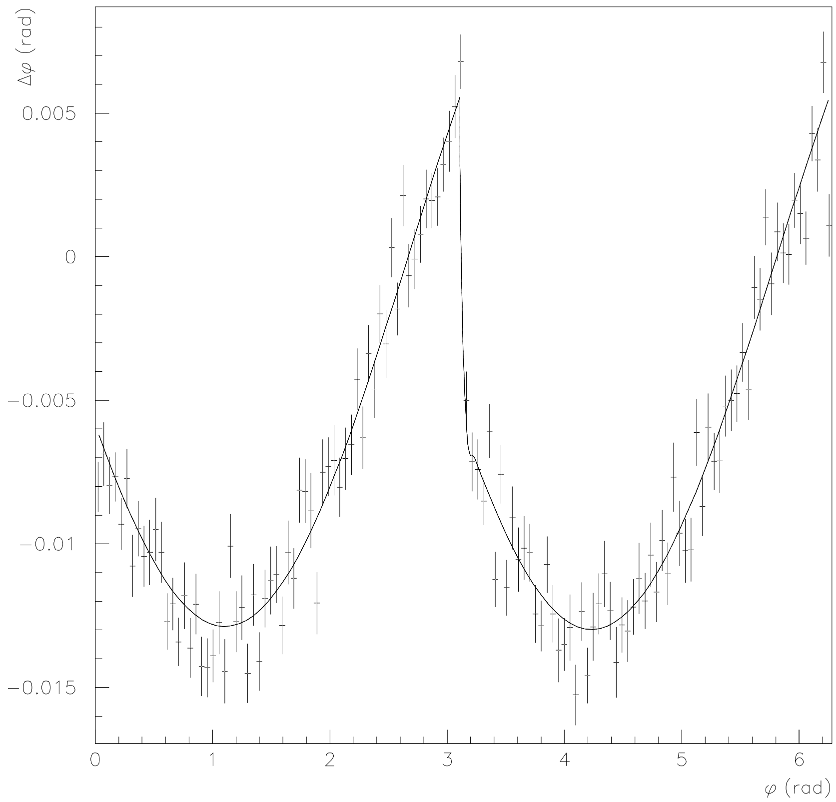

Figure 3.10: The acoplanarity ($\Delta\phi$) distribution in ϕ for $\pi^0\pi^0$ data from stack 30.1, $\sqrt{s} = 3009$ MeV. The function drawn is equation 3.20 with $(x_0, y_0) = (-0.39, 0.2)$ cm.

causes a shift in the measured angles that cannot be neglected. The displacement is measured and the angles corrected prior to starting the calibration process described in the previous section. Corrections for the vertex displacement are also important in the kinematical evaluation of the $\gamma\gamma$ events, discussed in chapter 5.

For a two body final state, trigonometry gives the following formula for the *acoplanarity*, $\Delta\phi \equiv \pi - |\phi_1 - \phi_2|$, as a function of ϕ for a vertex at $(x_0, y_0, 0)$ where ϕ is the azimuthal angle of one of the π^0s.

$$\tan(\frac{\Delta\phi}{2}) = \frac{x_0 \sin(\phi) - y_0 \cos(\phi)}{R - x_0 \cos(\phi) - y_0 \sin(\phi)} \tag{3.20}$$

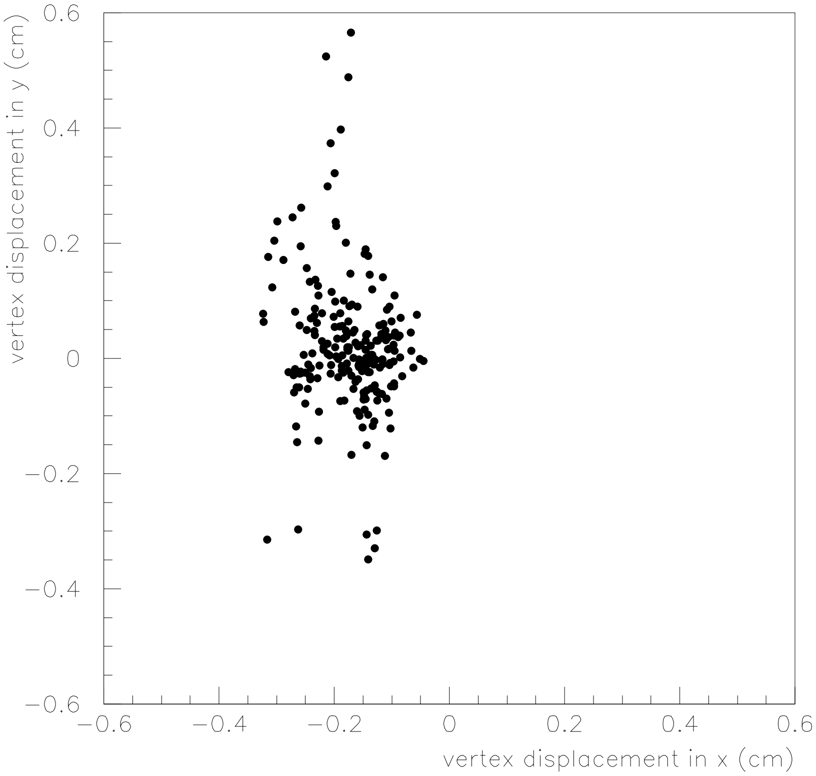

Figure 3.11: The vertex position of each stack is plotted as a single point. The shift away from $x = 0$ is a mis-alignment of the CCAL.

The $\Delta\phi$ values for bins in ϕ were fit to equation 3.20 to obtain x_0 and y_0.

For every stack, the (x,y) coordinate of the center of the interaction region is extracted from a clean sample of $\pi^0\pi^0$ events, whose selection is described in appendix B. Approximately 10,000 events are required for a resolution of 0.1 mm. The vertex position measured by the CCAL for each stack is plotted in figure 3.11.

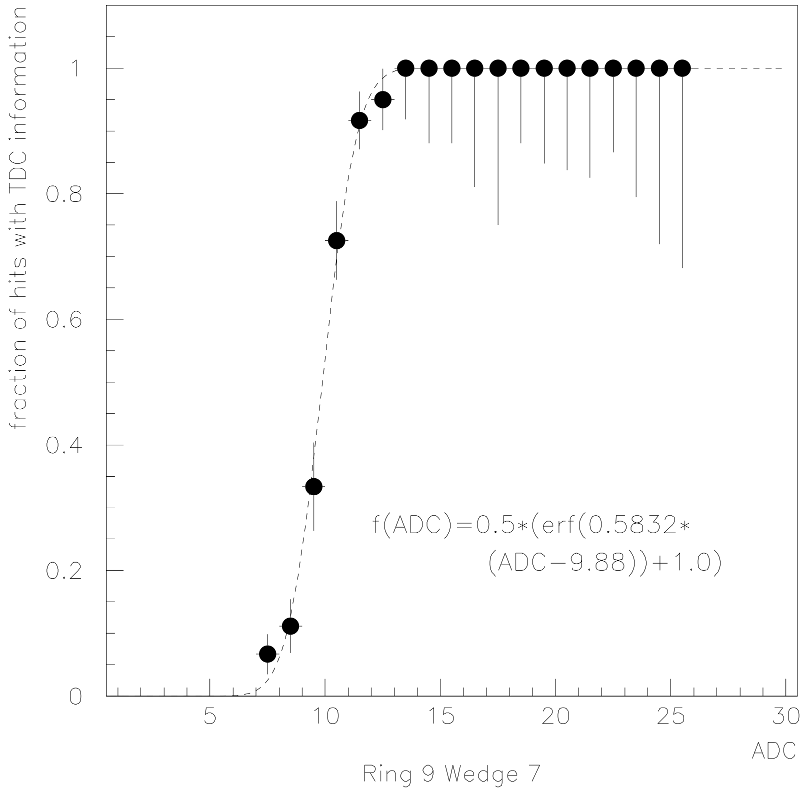

Figure 3.12: A sample turn-on curve for the discriminator in the shaper circuit. 1 ADC count is approximately 2.6 MeV. The error bars represent the 68% confidence region assuming Poisson statistics. The function plotted is a fit to equation 3.21, also displayed within the plot.

3.7 Cluster Timing

The multi-hit TDCs were used in *common stop* mode with a LSB of 1 ns, meaning that the counts reported were the integer number of ns between the leading edge of the discriminator output and a reference pulse timed to arrive approximately 10 ns after the end of the FERA gate. Thus, a larger TDC value corresponds to an earlier pulse. The entire window is 255 ns, sensitive to pulses arriving during the FERA gate or in the preceding 145 ns.

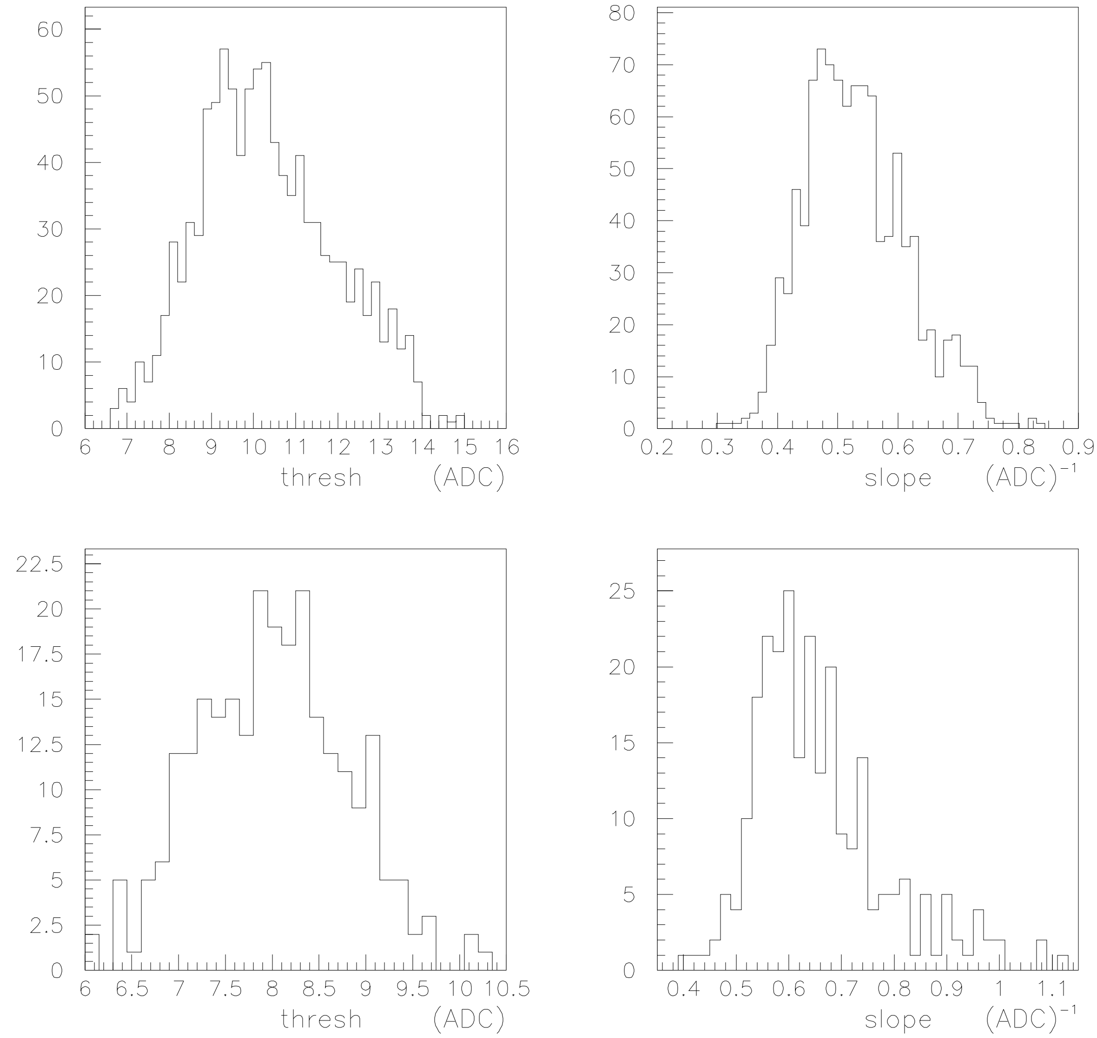

Figure 3.13: Distribution of the turn-on curve parameters for every channel. Data from rings 1-16 are in the top two plots, with the threshold on the right and the slope on the left, and data from rings 17-20 in the bottom plots. On average, 1 ADC count is 2.6 MeV.

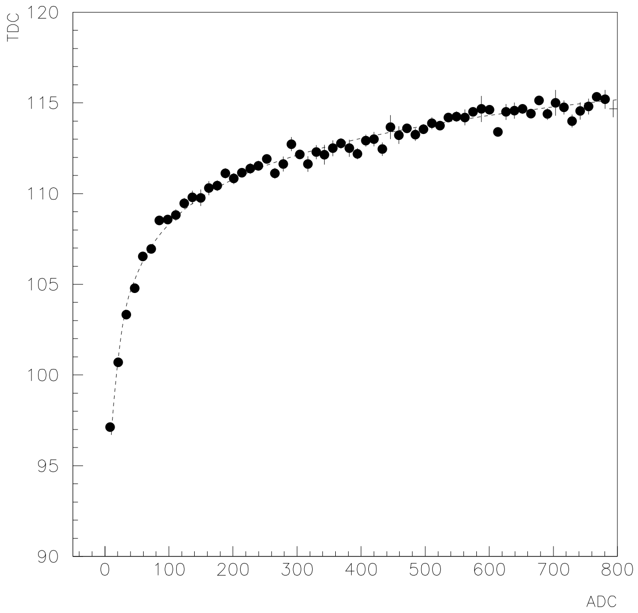

Figure 3.14: An example of the ADC dependence of the TDC signal for a single counter, ring 9 wedge 7. The function plotted is a fit to equation 3.22 with $B_0 = 2.84$ and $E_0 = 3.59$.

A sample turn-on curve, with a 5 mV discriminator threshold setting[1], is shown in figure 3.12. The fraction of ADC signals with a corresponding TDC signal is plotted as a function of ADC counts. The data are hits in that counter belonging to one of the clusters from a $\pi^0\pi^0$ event, (see Appendix B) These data are used to calculate all the constants mentioned in this section. The data are fit to the function

$$f = 0.5 \times (\mathrm{erf}(slope \times (\mathrm{ADC} - thresh)) + 1.0) \tag{3.21}$$

where *slope* and *thresh* are the two parameters of the fit and f is the fraction of hits per ADC bin that have TDC information. The turn-on curve for every channel was

[1]Throughout this document, the discriminator threshold quoted is the equivalent pulse height of the analog output signal. The voltage difference at the test points on the circuit is 100 times larger.

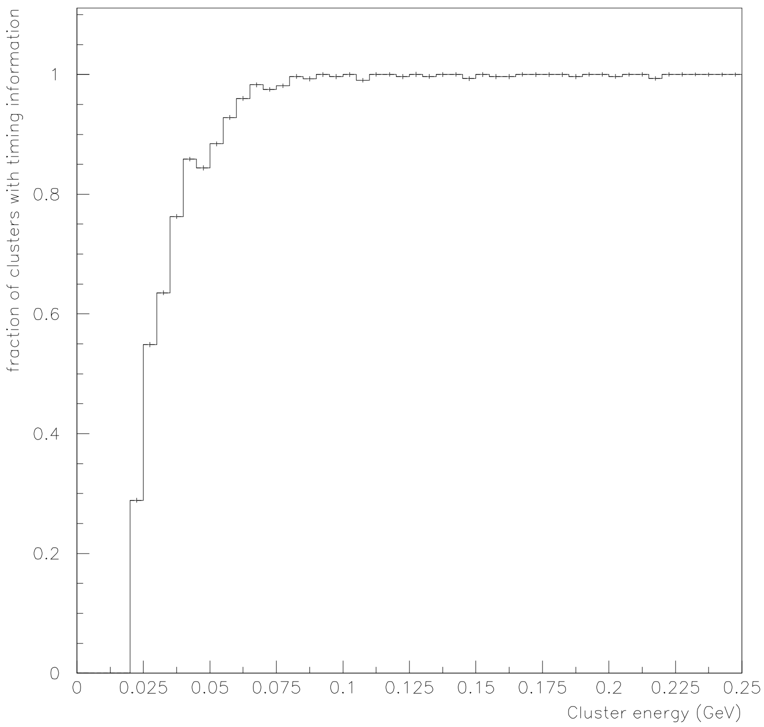

Figure 3.15: The fraction of clusters with timing information as a function of cluster energy.

measured periodically to monitor the electronics. Figure 3.13 shows the distribution of these parameters for the data taken during stack 8.

In order to compare the relative times of different size pulses, the measured TDC value is corrected for slewing, or the fact that different size pulses will cross the discriminator threshold at different times if their peaks are aligned. A plot of ADC counts vs. TDC counts for a single channel is shown in figure 3.14. The data are taken from a clean $\pi^0\pi^0$ sample (see Appendix B). For each block within a cluster, the ADC and TDC values are input if there is exactly one TDC hit in the window $[T_0 - 40, T_0 + 60]$, which roughly corresponds to the FERA gate. T_0 is defined for every channel as the average TDC value of a pulse with A_0 ADC counts, where A_0 is

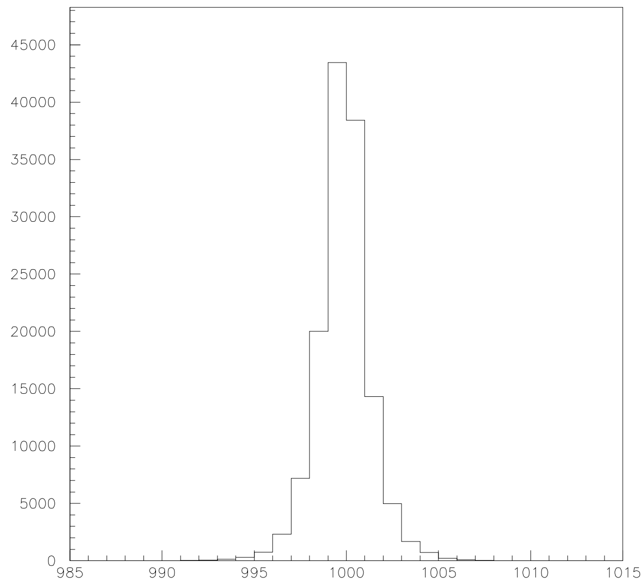

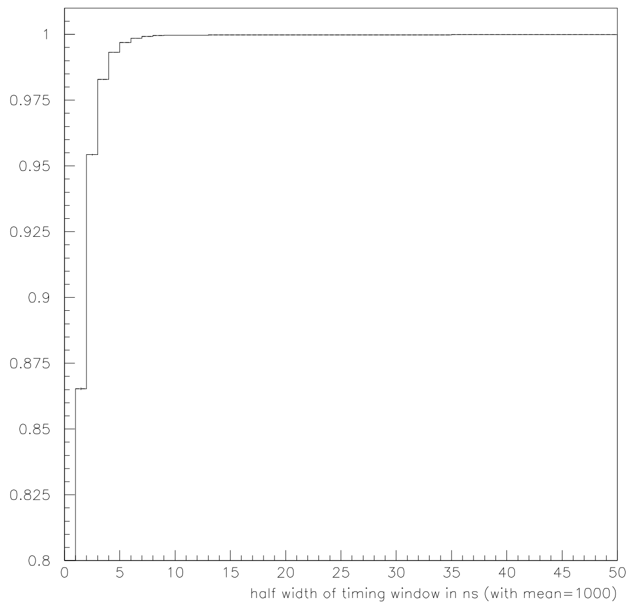

Figure 3.16: Above is the distribution of corrected TDC values for the clusters with timing information. A Gaussian fit yields a mean of 999.9 ns and a standard deviation of 1.3 ns. Below is the fraction of clusters within a window around 1000 ns as a function of the size of the window.

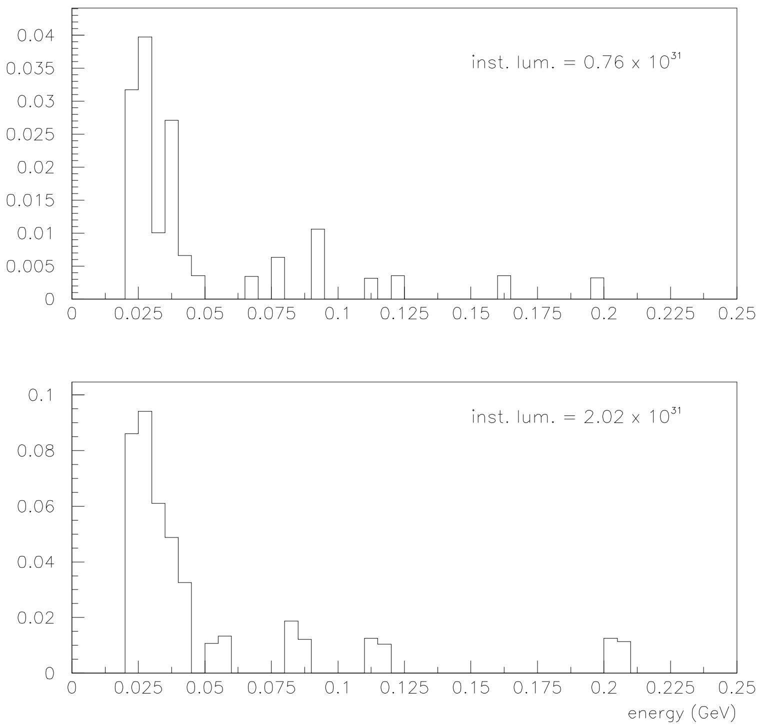

Figure 3.17: The fraction of $\pi^0\pi^0$ clusters mistakenly called out-of-time is plotted as a function of cluster energy for two different event rates. The low statistics, only 300 clusters per bin, make it difficult to see inefficiencies below 1%.

the *thresh* parameter from the turn-on curve. The spread of T_0 values are a result of differences in cable lengths and PMT response time between the channels. Then the data are fit to the function

$$\mathrm{TDC} = T_0 + B_0 \times (1 - \frac{A_0}{\mathrm{ADC}}) \times \log(\mathrm{ADC} + E_0) \tag{3.22}$$

where B_0 and E_0 are free parameters in the fit.

This fit is then used to assign a time to an energy deposit in a CCAL counter. If there is more than one TDC hit in the counter, and one or more of these hits is within the window $[T_0 - 40, T_0 + 60]$, the earliest hit within this window is chosen. If there are no hits within the window, the earliest hit is chosen. The counter is assigned a *corrected* TDC value using the equation

$$\mathrm{TDC_{corr}} = \begin{cases} \mathrm{TDC} - [T_0 + B_0 \times (1 - (A_0/\mathrm{ADC}))\times \\ \qquad \log(\mathrm{ADC} + E_0)] + 1000 & \mathrm{ADC} > A_0 \\ \\ \mathrm{TDC} - T_0 + 1000 & \mathrm{ADC} \leq A_0 \end{cases} \tag{3.23}$$

Since a cluster can have up to 9 blocks, one more step is needed. Only the TDC information of the two counters with the most ADC counts is considered. If neither block has any TDC information, the cluster is labeled *undetermined*. If either of the two blocks has a $\mathrm{TDC_{corr}}$ within 10 ns of 1000, the cluster is labeled *in-time*. Otherwise, the cluster is labeled *out-of-time* .

To study the efficiency and resolution of the cluster timing algorithm, clean $\pi^0\pi^0$ data are selected from a different stack than the one used to determine the slewing parameters. The split clusters are excluded, and the times of the remaining 146,920 clusters are studied. For cluster energies above 50 MeV, over 99.5% of the clusters are determined in-time. Below 50 MeV, the discriminator threshold becomes visible. When a pulse does not cross the discriminator threshold, an earlier pulse in the same channel can cause the small pulse, which would otherwise be undetermined, to be mistakenly identified as out-of-time. Thus, the number of out-of-time pulses below 50 MeV increases with instantaneous luminosity. More detail can be seen in figures 3.15-3.17, where the data shown are from stack 34, $\sqrt{s} = 2990$ MeV and an instantaneous luminosity of 0.76×10^{31} cm^{-2}s^{-1}.

Chapter 4

Background Sources and Estimates

The background to the $\gamma\gamma$ signal comes from $\pi^0\pi^0$ and $\pi^0\gamma$ events where the decay of the π^0s is asymmetric and the resulting low energy photon(s) lost either below the energy threshold of the CCAL or outside its geometrical acceptance. The expected background is calculated by first measuring the differential cross sections for both reactions, and then using a Monte Carlo simulation to predict how many $\pi^0\pi^0$ and $\pi^0\gamma$ events pass the $\gamma\gamma$ analysis cuts. Also the expected background from the continuum reaction $\overline{p}p \to \gamma\gamma$ is discussed. All of these processes are interesting physics measurements in their own right, not just irritating background sources. E760 published a measurement of the cross sections[17], and E835 plans a similar undertaking. In this document, the discussion is limited to what is necessary to understand the backgrounds to the charmonium channels.

The term *data-point* is used in the next three chapters and refers to the set of data taken at the same energy during a single stack. A number is assigned to each data-point, and is of the form $[stack].[order]$. For example, 7.2 refers to the 2nd set of data taken in the 7th stack.

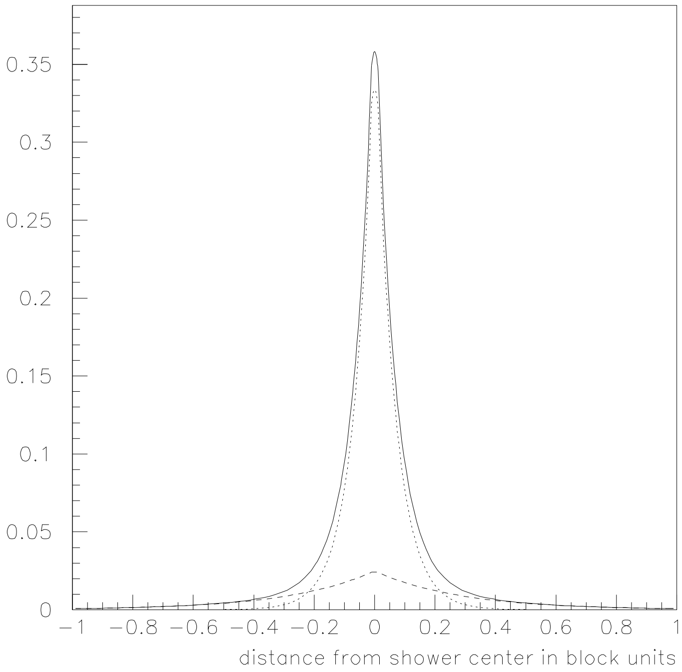

Figure 4.1: The shower profile in the wedge direction used by the Monte Carlo. The solid curve is the profile, which is the sum of two exponentials. The two exponentials are shown individually as the dashed curves. The profile models the average shower shape after the crack losses. Hence, the profile in the ring direction is slightly wider since less energy is lost in the cracks.

4.1 Monte Carlo performance

The Monte Carlo simulates events in the CCAL by first randomly choosing the energy and direction of the particles in an event, within the constraints of energy and momentum conservation. A simulation of the CCAL response is then used to determine the ADC counts and TDC signal for each block in the CCAL. This response simulation was chosen over a full simulation of the particle interactions in the lead glass (with GEANT for example) because the response simulation is 10-20 times faster and the results sufficiently accurate for studying the $\gamma\gamma$ background.

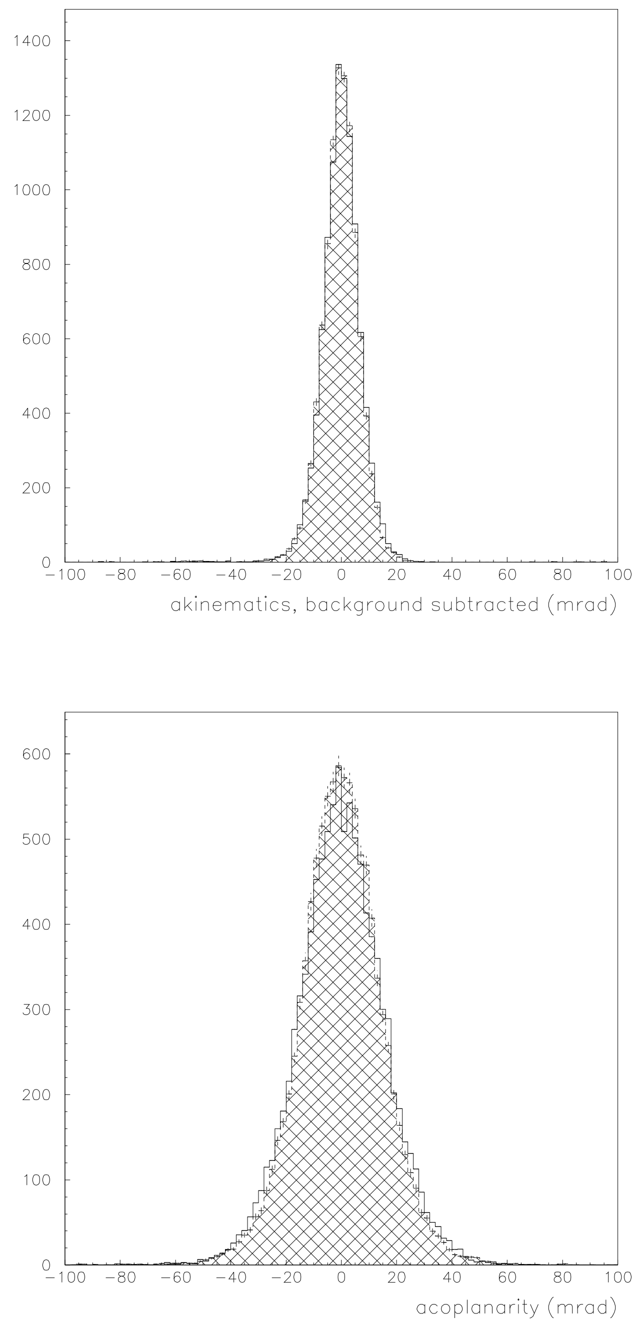

Figure 4.2: Comparison of $\pi^0\pi^0$ analysis variables from data (white histogram) and Monte Carlo (shaded histogram) samples for data-point 34.1.

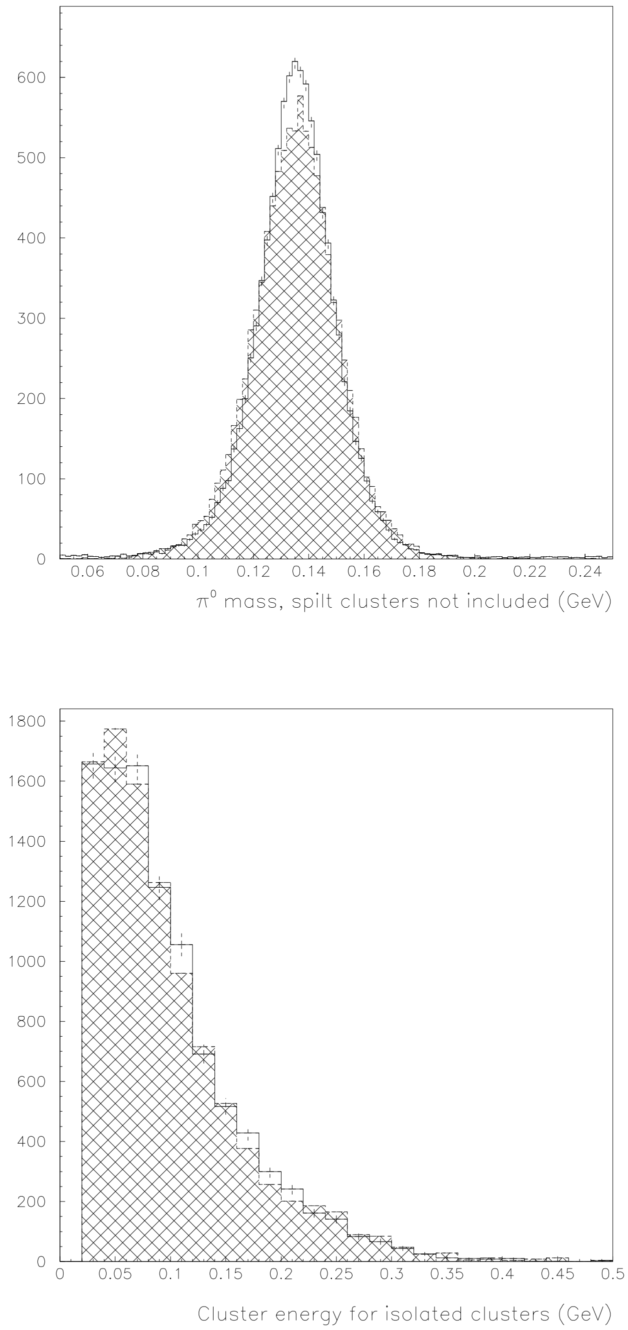

Figure 4.3: Comparison of $\pi^0\pi^0$ analysis variables from data (white histogram) and Monte Carlo (shaded histogram) samples for data-point 34.1.

The event vertex is randomly chosen in the interaction region from a distribution based on the shapes of the beam and gas-jet target, and centered at the (x_0, y_0) measured for the data-point being simulated.

The expected center of gravity of the cluster is calculated from the position of the particle by reversing equation 3.4. Then the fraction of the particle's energy lost in the cracks is calculated with equation 3.6 and subtracted. The distribution of the remaining energy about the cluster's center of gravity is modeled with the sum of two exponentials, shown in figure 4.1. This parameterization was chosen empirically, comparing simulated and actual $\pi^0\pi^0$ data for a data-point taken at low instantaneous luminosity. The function is integrated to obtain the energy deposited in each block.

Both the fraction of energy lost in the cracks, and the amount of energy deposited in each block is smeared, simulating the energy resolution of the CCAL. A pedestal fluctuation is also introduced for each block, based upon the pedestal widths measured prior to taking data each data-point. The calibration constants for the data-point being simulated are used to convert energy to ADC counts.

The timing is simulated for every block considered in the determination of a cluster time. Hits above 50 ADC counts are automatically assumed to have a corresponding TDC hit within the window. For hits below 50 ADC counts, the timing is simulated by first determining whether TDC information exists for that block, and second whether that information is within the 20 ns window. The first is obtained from the turn-on curves measured with $\pi^0\pi^0$ data (discussed in section 3.7). The fraction obtained from the turn-on curve is combined with a random variable to determine whether the simulated ADC hit has timing information. If the simulated hit has timing information, then it is determined whether that time is within the ± 10 ns window. To do this, a lookup table is created from actual $\pi^0\pi^0$ data. For each ADC value, the fraction of corresponding TDC hits outside the window is tabulated. The value from this table is combined with a random number to determine whether the simulated hit is outside the window. There are a only few blocks for which there is a non-zero fraction of hits outside the window, and these inefficiencies are found only in the smallest ADC values (values near A_0, see equation 3.22).

Finally, to simulate the effect of overlapping events, a data event taken with the random gate trigger during that data-point is superimposed onto the Monte Carlo event. A comparison of the data and the Monte Carlo $\pi^0\pi^0$ events for the same data-point is made in figures 4.2 and 4.3. The distributions have been normalized for comparison, and the error bars represent the statistical error associated with the number of events in each sample.

4.2 $\pi^0\pi^0$ differential cross section

Beginning with the data in the neutral DSTs,[1] $\pi^0\pi^0$ events are selected using the cuts outlined below. the event topology with the minimum value of $\sqrt{(2\Delta\theta)^2 + (\Delta\phi)^2}$ is chosen. Then the following cuts are applied:

- Exactly 4 i.o.u.[2] CCAL clusters above 50 MeV.
- $\mid M_{\pi^0} - 135 \mid \leq 35$ MeV OR the π^0 is formed from the two halves of a split cluster.
- *acoplanarity* $(\Delta\phi) \equiv \mid \pi - \mid \phi_1 - \phi_2 \mid\mid < 30\ mrad$
- *akinematics* $(\Delta\theta) \equiv \mid \theta_{1pred}(\theta_{2meas}) - \theta_{1meas} \mid < 2\ \sigma_{akin}$, where $\theta_1 \leq \theta_2$.
- The centers of the 4 clusters are within CCAL rings 2-18.

[1] The neutral DSTs are described in detail in appendix E.

[2] in-time or undetermined

The *akinematics* is difference between the measured and predicted polar angle of the forward (small θ) π^0. The predicted angle is calculated by using the measured polar angle of the backward π^0 and two-body kinematics. The width of the akinematics distribution decreases as the kinematical variable s increases. The cuts are discussed in more detail in appendix B.

A small amount of background remains from $\overline{p}p \to \pi^0\pi^0\pi^0$ and $\overline{p}p \to \pi^0\omega \to \pi^0\pi^0\gamma$ [17], where either one or two low energy photons were undetected. This background can be seen as an asymmetric distribution underneath the akinematics peak in figure B.1. It is typically 5% of the data at all energies, except where the $\pi^0\pi^0$ differential cross section has a sharp minimum, and the background can be as large as 10%. This background is subtracted by first collecting the data in bins 0.025 wide in $\cos\theta^*$, and then fitting the akinematics distribution for each bin to a gaussian, representing signal, plus a quadratic, representing background. $f_{signal,i}$ is calculated as the fraction of events that are signal, and accepted by the akinematics cut, in the *ith* bin.

The $\pi^0\pi^0$ differential cross section is given by the equation

$$\frac{d\sigma(\overline{p}p \to \pi^0\pi^0)}{d \mid cos\theta^* \mid} = \frac{N_{obs,i} f_{signal,i}}{\int Ldt} \times \frac{1}{(a\epsilon_{tot})_i} \tag{4.1}$$

where $N_{obs,i}$ is the observed number of $\pi^0\pi^0$ events in the *ith* bin, $\int Ldt$ is the integrated luminosity and $a\epsilon_{tot}$ can be further broken down

$$\begin{aligned} a\epsilon_{tot} \equiv \; & a \times \epsilon_{analysis} \times (1 - P_{cont}) \\ & \times \epsilon_{trigger} \times (1 - P_{conv})^4 \times (1 - P_{Dalitz})^2 \times \epsilon_{NDST} \end{aligned} \tag{4.2}$$

where a is the geometrical acceptance, P_{cont} is the probability that an overlapping event contaminated a good event, causing it to be rejected, P_{conv} is the probability that a photon converts into a e^+e^- pair that turns on the neutral veto and P_{Dalitz} is

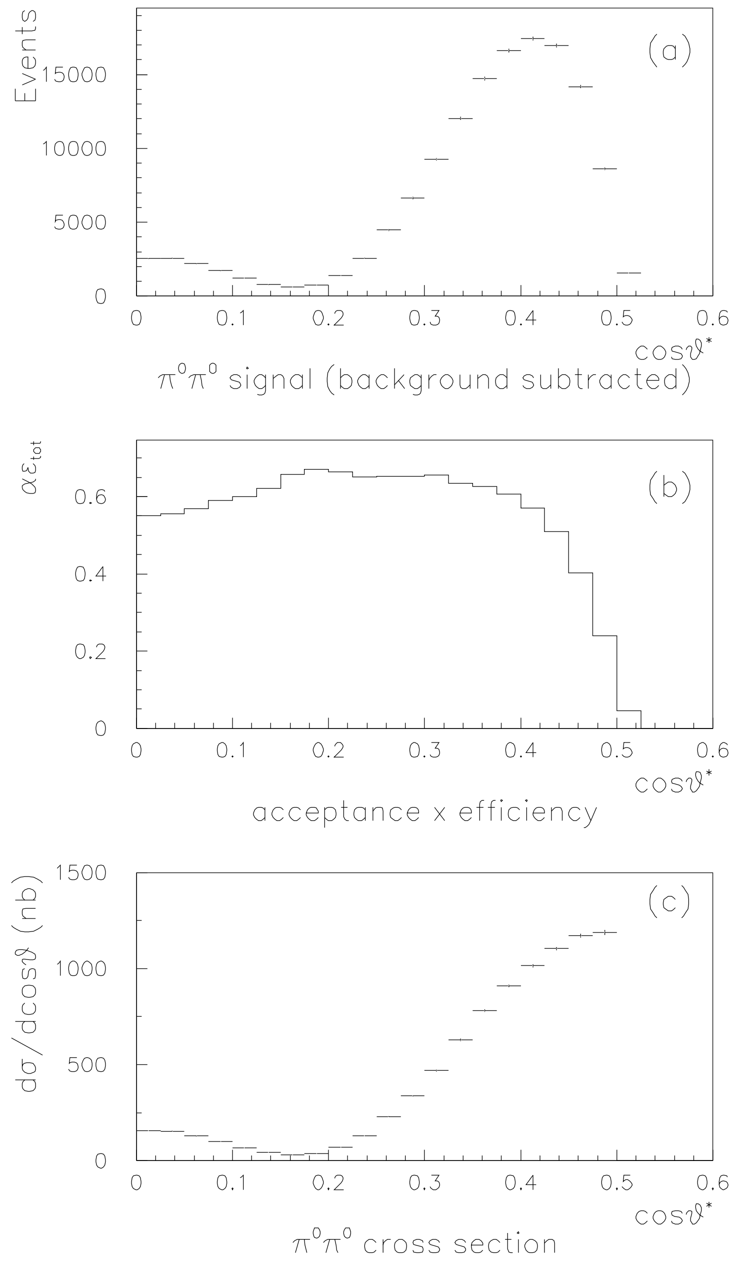

Figure 4.4: The distribution in $\cos\theta^*$ of (a) the $\pi^0\pi^0$ events after subtracting the background, (b) $a\epsilon_{tot}$, and (c) the $\pi^0\pi^0$ differential cross section. The data are from data-point 48.1, $\sqrt{s} = 2.986$ GeV.

the probability that a Dalitz decay of a π^0 turns on the neutral veto. Of this product, P_{conv}, P_{Dalitz} and $\epsilon_{trigger}$ are known constants. P_{conv} and P_{Dalitz} are discussed in appendix C. The trigger efficiency, $\epsilon_{trigger}$, is the combined efficiency for the hardware trigger and the online filter and is 100% for all the data. This is calculated in appendix D. The neutral DST efficiency is a function of $\sqrt{s}$, ranging from 94% to 99%, as shown in appendix E The remaining terms, $a\epsilon_{analysis}(1 - P_{cont})$ are treated as a single number, which changes with the running conditions, and must be calculated for each data-point.

The cross section is calculated on bin by bin basis, using an iterative procedure to obtain the product $(a\epsilon_{tot})_i$. The iteration is necessary because events generated in one bin can migrate to another bin when reconstructed in the CCAL, due to the CCAL position and energy errors. The iteration process alternately calculated the angular distribution of the $\pi^0\pi^0$ events and the product $(a\epsilon_{tot})_i$.

The Monte Carlo events are generated[3] evenly in $\cos\theta^*$ and then reconstructed using the same analysis code used for the data. The Monte Carlo events are weighted, using the generated calue of $\cos\theta^*$, by an angular distribution function, which is assumed flat in $\cos\theta^*$ for the first iteration. The iteration then proceeds as follows

1. The product $(a\epsilon_{tot})_i$ is calculated, for each bin in $\cos\theta^*$, as the number of Monte Carlo events reconstructed in the *ith* bin, divided by the number of Monte Carlo events generated in the *ith* bin, and multiplied by the factor $0.025(1 - P_{conv})^4 \cdot (1 - P_{Dalitz})^2 \cdot \epsilon_{trigger}$, a known constant for each data-point.

[3]Enough Monte Carlo events are generated so that the statistical error is negligible, typically five times the number of data events. This applies to all uses of the Monte Carlo discussed in this chapter.

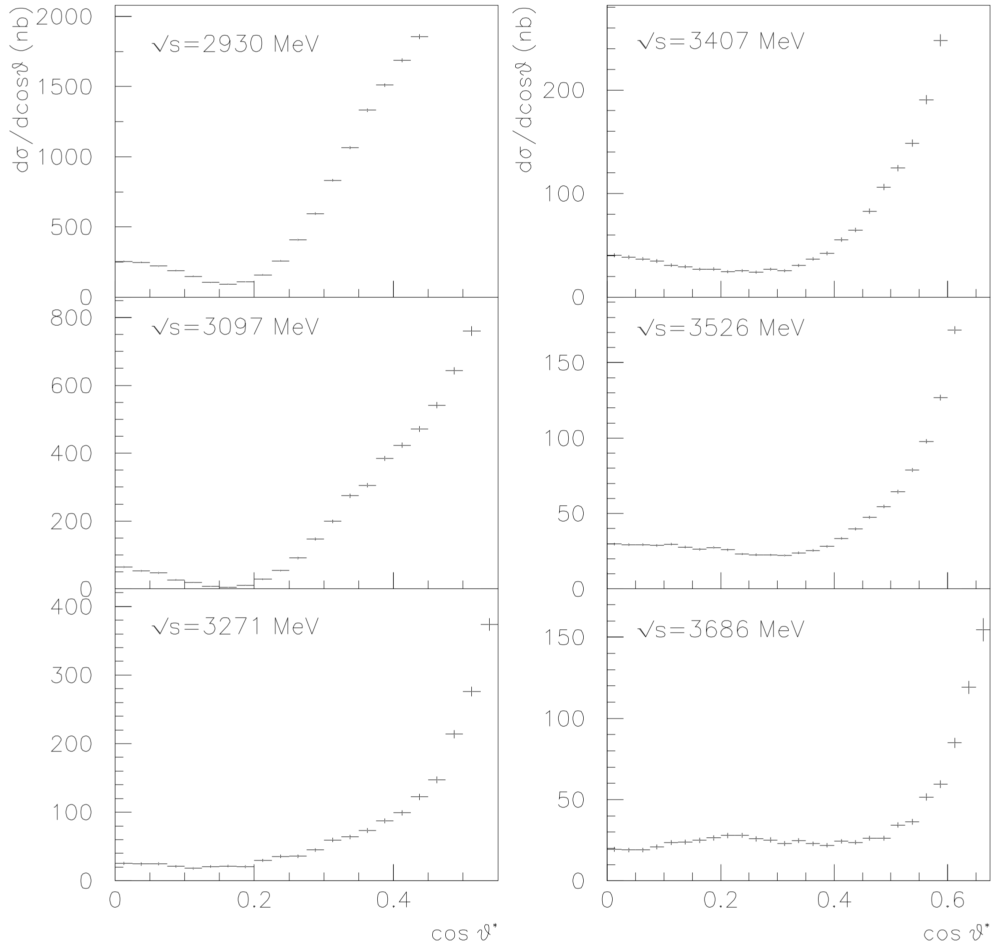

Figure 4.5: The measured $\pi^0\pi^0$ differential cross section for a large range of $\sqrt{s}$.

2. The reconstructed Monte Carlo events are weighted by the angular distribution found in the previous iteration, using the generated angle.

3. The new form of the angular distribution is then found by dividing the data by $a\epsilon_{tot}$, bin by bin, and fitting the result to a six degree polynomial.

4. The new angular distribution is then used in step 1 of the next iteration.

The iteration converges because the fraction of events that are reconstructed in a bin different than the generated one is small. The process is complete when the corrected angular distribution changes by less than 1% in every bin, typically 4 iterations. The product $a\epsilon_{tot}$ and differential cross section that result from this process are shown in figure 4.4 for a single data-point.

4.3 $\pi^0\gamma$ differential cross section

Beginning with the neutral DSTs, $\pi^0\gamma$ events are selected from events having exactly 3 i.o.u. clusters above 50 MeV in the CCAL. As with the $\pi^0\pi^0$ event selection, the event topology with the minimum value of $\sqrt{(2\Delta\theta)^2 + (\Delta\phi)^2}$ is chosen. Then the following cuts are applied:

- Exactly 3 i.o.u. CCAL clusters above 50 MeV.

- $\mid M_{\pi^0} - 135 \mid \leq 35$ MeV OR the π^0 is formed from the two halves of a split cluster.

- A confidence level from a SQUAW[42] kinematical fit greater than 10%.

- The centers of the 3 clusters are within CCAL rings 2-18.

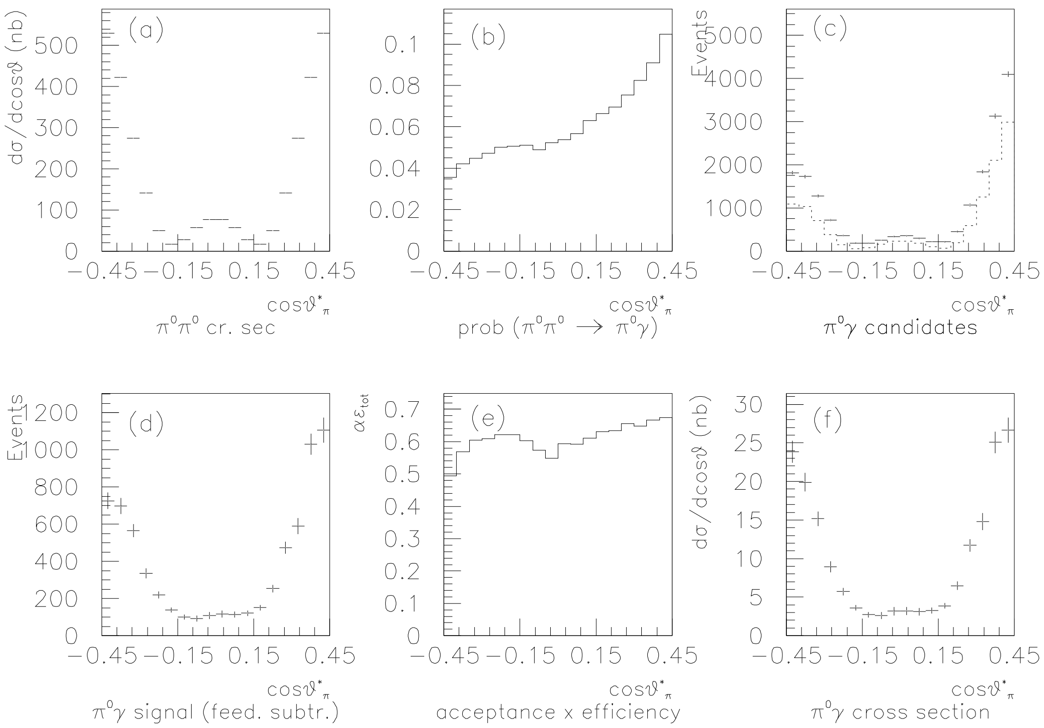

Figure 4.6: A pictorial description of the $\pi^0\gamma$ differential cross section calculation, using data from data-point 48.1, $\sqrt{s} = 2.986$ GeV.

In the data surviving these cuts, there is a significant background from $\pi^0\pi^0$ events, where one of the photons is not detected by the CCAL. From the $\pi^0\pi^0$ differential cross section, the Monte Carlo can predict how many $\pi^0\pi^0$ events there are in the $\pi^0\gamma$ candidates. Figure 4.6(a) shows the measured $\pi^0\pi^0$ cross section, and (b) the probability of a $\pi^0\pi^0$ event to mimic a $\pi^0\gamma$ event. The multiplication of (a) and (b), multiplied by the luminosity, yields the dashed line in (c), the calculated background in the $\pi^0\gamma$ data. The solid lines on the same plot represent the candidate events. The background events are subtracted from the candidates, 4.6(d), and the same iterative process used for the $\pi^0\pi^0$ cross section is performed to obtain the product $(a\epsilon_{tot})_i$,

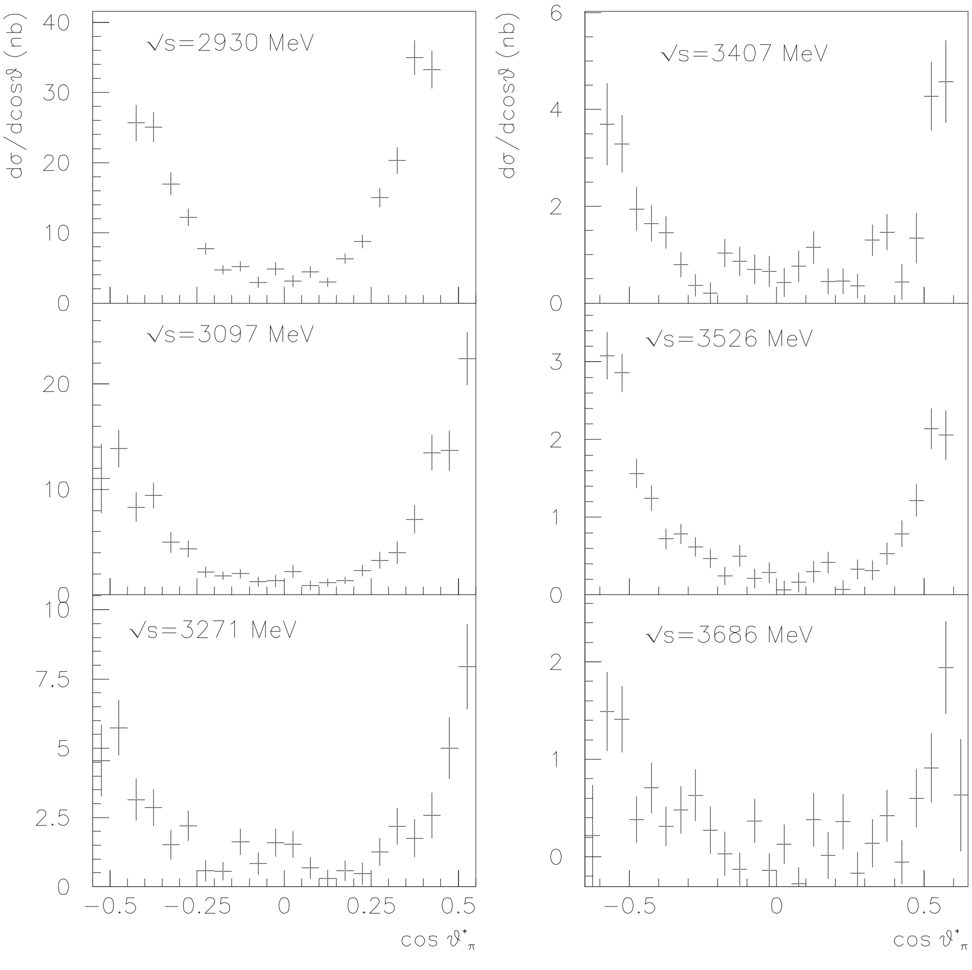

Figure 4.7: The measured $\pi^0\gamma$ differential cross section for a large range of $\sqrt{s}$.

figure 4.6(e) and the $\pi^0\gamma$ differential cross section, 4.6(f), calculated with the equation

$$\frac{d\sigma(\overline{p}p \rightarrow \pi^0\gamma)}{d(cos\theta^*_\pi)} = \frac{N_{obs,i}}{\int Ldt} \times \frac{1}{(a\epsilon_{tot})_i} \tag{4.3}$$

where $N_{obs,i}$ is the observed number of $\pi^0\gamma$ events in the ith bin, $\int Ldt$ is the integrated luminosity, and $a\epsilon_{tot}$ can be further broken down

$$\begin{aligned} a\epsilon_{tot} \equiv\ & a \times \epsilon_{analysis} \times (1 - P_{cont}) \\ & \times (1 - P_{conv})^3 \times (1 - P_{Dalitz}) \times \epsilon_{NDST} \times \epsilon_{trigger} \end{aligned} \tag{4.4}$$

This method of measuring the differential cross section relies heavily on the Monte Carlo determination of the number of $\pi^0\pi^0$ events present in the $\pi^0\gamma$ data. However, charge conjugation invariance demands that the final cross section be symmetric around $\cos\theta^* = 0$. The symmetry of the measured cross section is a strong test of the Monte Carlo performance.

4.4 Calculation of the $\pi^0\pi^0$ and $\pi^0\gamma$ contribution to the $\gamma\gamma$ background

With both differential cross sections, the Monte Carlo can predict the number of events these reactions contribute to the $\gamma\gamma$ background when low energy photons are lost. Figure 4.8(b) shows the probability that a simulated $\pi^0\pi^0$ event will pass the $\gamma\gamma$ analysis cuts. Multiplying the $\pi^0\pi^0$ cross section by this probability gives the expected $\gamma\gamma$ background from $\pi^0\pi^0$ figure 4.8(c). The same method produces figure 4.8(f) for $\pi^0\gamma$ events.

This prediction can then be compared with the observed number of events away from the charmonium resonances. The predicted background for the η_c region is shown in figure 4.9, along with the off-resonance data.

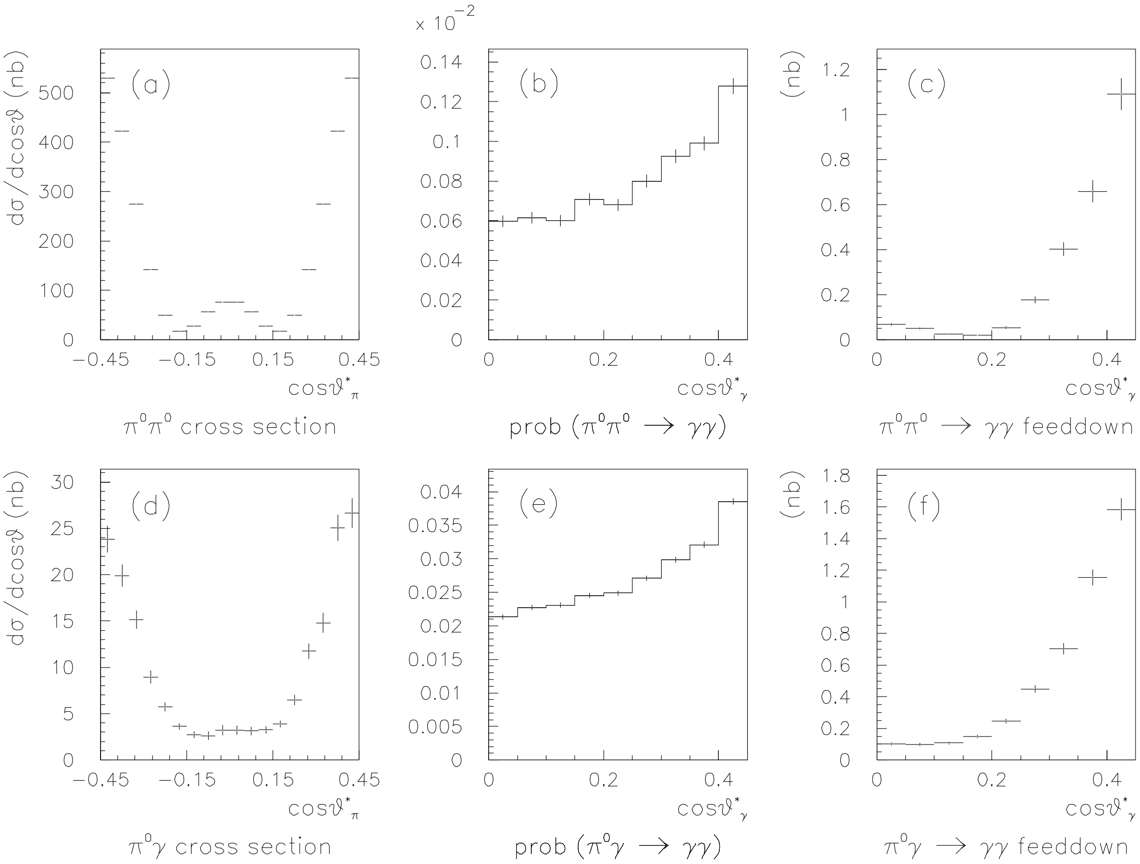

Figure 4.8: A pictorial description of the $\gamma\gamma$ background calculation, using data from data-point 48.1, $\sqrt{s} = 2.986$ GeV. More details are given in the text.

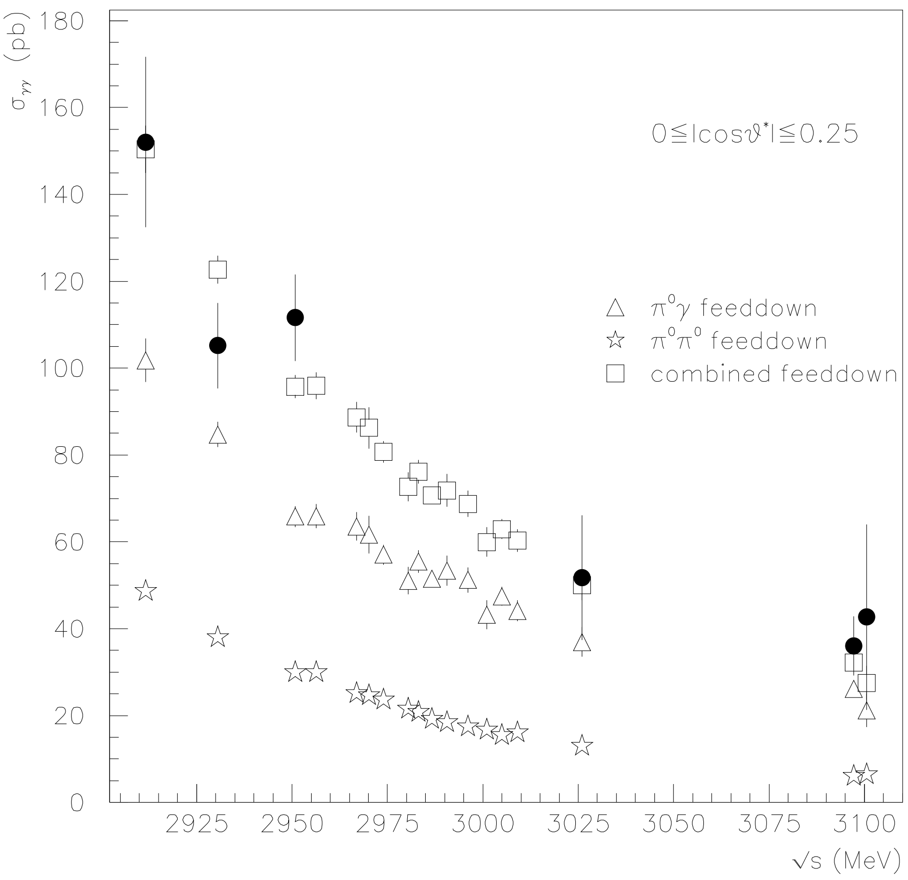

Figure 4.9: Results of the background calculation in the η_c region. The squares are the combined background from $\pi^0\pi^0$ and $\pi^0\gamma$, and the circles are the data. The errors shown on the feeddown points are statistical only.

4.5 Estimation of systematic errors

Any imperfections in the Monte Carlo reproduction of the cluster positions and energies will result in an error in the determination of the efficiency term $a\epsilon_{tot}$. The systematic errors of the $\pi^0\pi^0$ and $\pi^0\gamma$ cross sections are evaluated by by varying the event selection cuts and observing any changes in the $\pi^0\pi^0$ cross section. For the cuts on $\Delta\theta$,$\Delta\phi$, and M_{π^0}, the $\pi^0\pi^0$ cross section changed less than 1% when the cuts are varied $\pm$10% of their total value. For example, the $\pi^0\pi^0$ cross section is calculated for two values of the cut on $\Delta\phi$: $25, 35$ mrad. (The standard cut is 30 mrad.) The ratio of the two cross sections obtained with modified cuts was within the range 1.00 ± 0.01 for all three cuts listed above. This study was also done changing the total cluster energy threshold from 50 MeV to 40 and 60. Again, the $\pi^0\pi^0$ cross section changes by less than 1%.

The remaining possible source of systematic error is the cluster mass cut for identifying π^0s. The value of the cut, $M_{cl} = 100$ MeV, is conservatively chosen so that no isolated clusters are mis-identified as symmetric π^0s. This has the unfortunate consequence that some of the symmetric π^0s are identified as single isolated clusters. Since one cluster is found instead two for such a π^0, the event is rejected by the cut on the number of clusters. The calculation of $a\epsilon_{tot}$ with the Monte Carlo contains this efficiency. However, the lower plot in figure 4.10 shows that the simulated cluster mass (shaded histogram) is shifted to the left of the actual cluster mass (white histogram). The shared clusters have not been included in this plot so that the separation of the isolated and split clusters is clearly visible. The split clusters form the peak on the right, and the left tail of this peak is missing because of the cut. Using a Gaussian fit to each distribution above $M_{cl} = 100$ MeV, it is estimated that roughly 5% of the split clusters in the actual data are lost to this cut and roughly 10% of the split

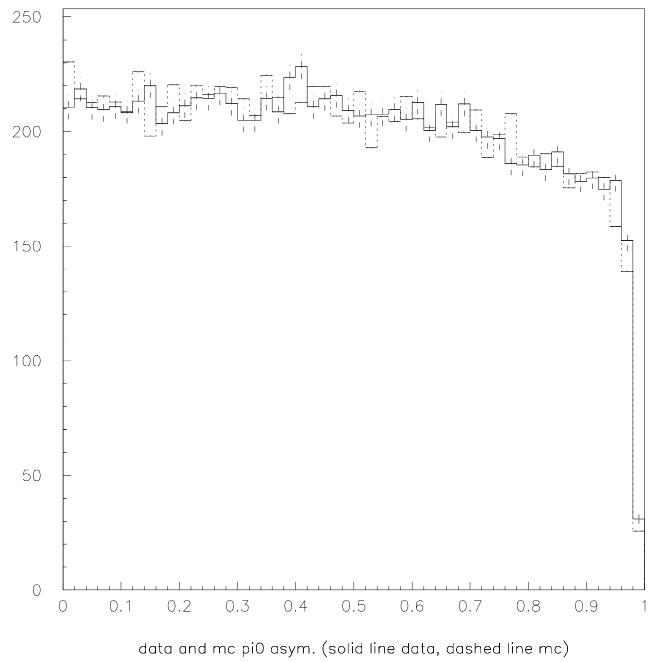

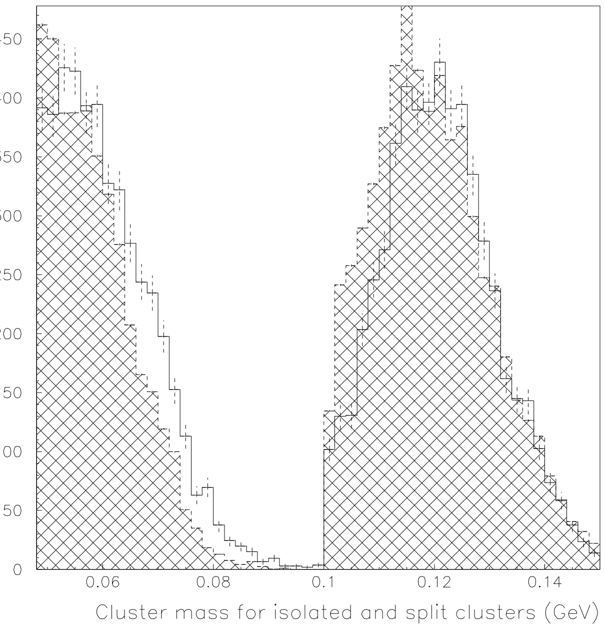

Figure 4.10: The π^0 asymmetry (above) and cluster mass (below) for data and Monte Carlo events. In the asymmetry plot, the dashed line is the simulated data and the solid the actual data. The cluster mass is shown in the region of the cut for cluster splitting, $M_{cl} = 100$ MeV, with the simulated events in the shaded histogram.

clusters in the simulated data are lost to this cut. In the region of the η_c, 5% of the π^0s in the data sample are split and near the χ_2 resonance, 12% of the π^0s in the data sample are split. The net systematic error on the $\pi^0\pi^0$ and $\pi^0\gamma$ cross sections is less than 1% in the η_c region. This is verified by the method described above: lowering the cluster mass cut and observing the corresponding change in the cross section. Combining all the cuts, the Monte Carlo contributes a conservative estimate of 2% to the systematic error on the $\pi^0\pi^0$ and $\pi^0\gamma$ cross sections.

Lowering the CCAL cluster energy threshold to 20 MeV for the feeddown calculation adds an additional systematic error. The acceptance gained by lowering the threshold is seen by comparing the upper plot in figure 4.10, the π^0 asymmetry distribution for data selected with 50 MeV energy thresholds, with the asymmetry plot in figure 3.8, which was made with 20 Mev thresholds. The plots have identical binning, and the bins near $asymmetry = 1$ have more events for the lower threshold. There is also a small difference between the actual data and the simulated data in these bins in figure 4.10. This difference indicates that the Monte Carlo overestimates the fraction of low energy clusters lost below the threshold or outside the acceptance by approximately 5%. This systematic error is translated to a systematic error on the total feeddown cross section.

The feeddown cross section is approximated as

$$\sigma_{feed} = \sigma_{\pi^0\pi^0} P_\gamma^2 + \sigma_{\pi^0\gamma} P_\gamma \tag{4.5}$$

where P_γ is the probability to lose a photon. The systematic error on σ_{feed} from the error on P_γ is

$$\Delta\sigma_{feed} = (2\sigma_{\pi^0\pi^0} P_\gamma^2 + \sigma_{\pi^0\gamma} P_\gamma)\frac{\Delta P_\gamma}{P_\gamma} \tag{4.6}$$

and using the approximations $\sigma_{\pi^0\pi^0}P_\gamma^2 = \frac{1}{3}\sigma_{feed}$ and $\sigma_{\pi^0\gamma}P_\gamma = \frac{2}{3}\sigma_{feed}$ (see figure 4.9),

$$\frac{\Delta\sigma_{feed}}{\sigma_{feed}} \approx \frac{\Delta P_\gamma}{P_\gamma} \approx 5\% \tag{4.7}$$

$\Delta\sigma_{feed}$ is used as the *r.m.s.* value of the systematic error, and is combined in quadrature with the ones from the $\pi^0\pi^0$ and $\pi^0\gamma$ cross sections to give an estimate of the total systematic error of 6% on the feeddown cross section. This estimate is combined in quadrature with the statistical error on the feeddown cross section, from the statistical errors on $\sigma_{\pi^0\pi^0}$ and $\sigma_{\pi^0\gamma}$. The combined error is the term σ_k in the likelihood function 6.5.

4.6 $\gamma\gamma$ continuum

The final source of possible background discussed here is the continuum reaction $\overline{p}p \to \gamma\gamma$. The cross section is expected to decrease with s[38], and the angular distribution is expected to be peaked in the forward direction[46]. E760 found no evidence for this reaction in the region of the η_c, and placed an upper limit on the cross section of $\sigma(\overline{p}p \to \gamma\gamma) < 43$ pb, with $|\cos\theta^*| \le 0.4$ and $\sqrt{s} = 2988$ MeV[16]. The time-reversed reaction, $\gamma\gamma \to \overline{p}p$, has been observed by the CLEO[18] and VENUS[54] experiments. The relation between the cross sections is found using detailed balance

$$\frac{\frac{d\sigma}{d\Omega}(\overline{p}p \to \gamma\gamma)}{\frac{d\sigma}{d\Omega}(\gamma\gamma \to \overline{p}p)} = \frac{p_\gamma^2}{2p_p^2} \tag{4.8}$$

where p is the momentum of the final particles. At $\sqrt{s} = 3.0$ GeV, the ratio is approximately $\frac{2}{3}$. Both experimental results indicate that the angular distribution of the reaction $\gamma\gamma \to \overline{p}p$ changes dramatically from $\sqrt{s} = 2.0$ GeV to $\sqrt{s} = 3.0$ GeV. Only the VENUS measurement reports the data in the E835 region of interest: 2.9 GeV $< \sqrt{s} <$ 3.1 GeV and $|\cos\theta^*| \le 0.25$. Unfortunately, there are only a

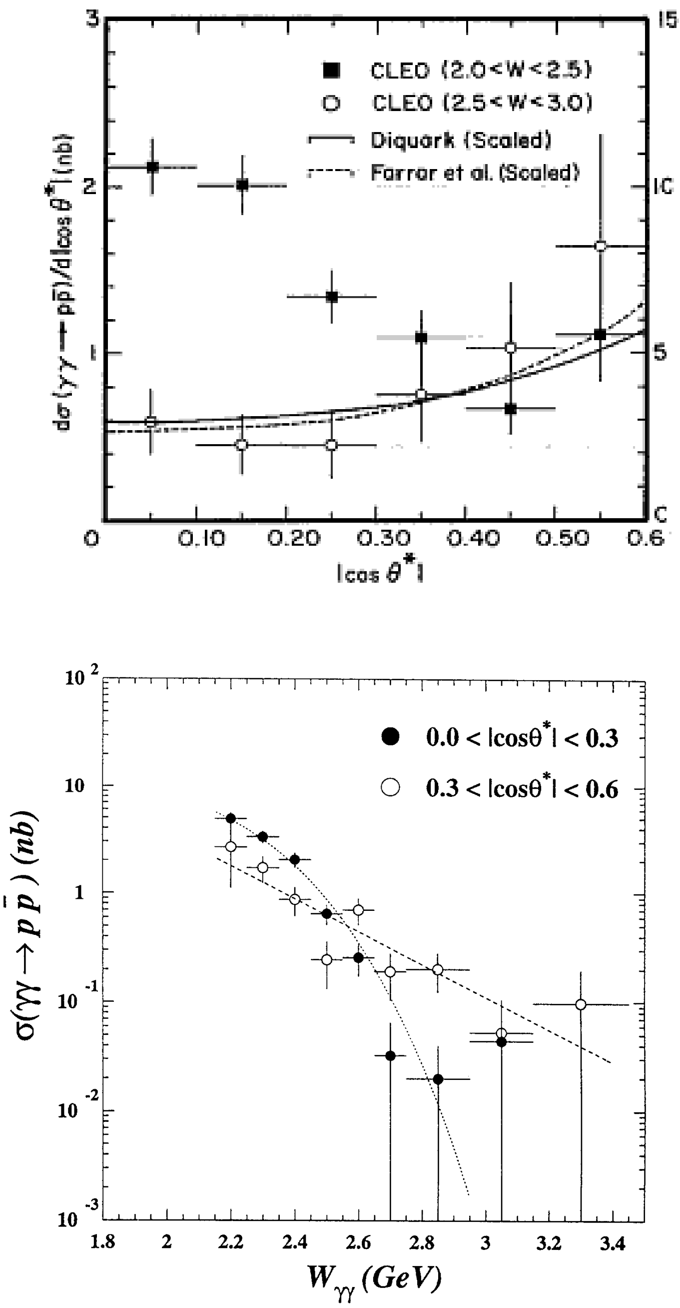

Figure 4.11: The recent measurements of the reaction $\gamma\gamma \rightarrow \overline{p}p$ by the CLEO collaboration[18] (above) and the VENUS collaboration[54] (below).

few events in this restricted region. From their data, shown in figure 4.11, we expect $\sigma(\gamma\gamma \rightarrow \overline{p}p) = 25 \pm 25$ pb for 2.9 GeV $< \sqrt{s} <$ 3.1 GeV and $|\cos\theta^*| \leq 0.25$, which results in $\sigma(\overline{p}p \rightarrow \gamma\gamma) = 16 \pm 16$ pb.

Theory offers predictions about the size of the continuum reaction; however, the predictions vary substantially. Farrar, Maina and Neri[46] predict $\sigma(\gamma\gamma \rightarrow \overline{p}p) \approx 3$ pb at $\sqrt{s} = 2.4$ GeV and $|\cos\theta^*| \leq 0.3$ while Kroll *et al.*[60] predict $\sigma(\gamma\gamma \rightarrow \overline{p}p) = 34$ pb for $|\cos\theta^*| \leq 0.2$ and $\sqrt{s} = 3.0$ GeV. With no clear answer from theory or experiment, the $\overline{p}p \rightarrow \gamma\gamma$ continuum signal cannot be neglected as a source of background events near the η_c resonance and is included in the analysis of section 6.4. For $\sqrt{s} > 3.1$ GeV, the contribution of the continuum to the background is assumed negligible.

Chapter 5

Data Analysis

E835 collected over 150 pb^{-1} of data. The table in appendix A lists all the data-points along with the associated integrated and instantaneous luminosities, the number of $\gamma\gamma$ events passing the analysis cuts, and the efficiency of the analysis cuts. This chapter describes in detail the analysis cuts and the resulting efficiencies. Figure 5.1 shows the $\gamma\gamma$ signal in the regions of the η_c, χ_0, χ_2, and η_c'.

5.1 Event selection

Event selection begins with the events identified by the online filter as potential $\gamma\gamma$ events. These are events that satisfy either the PBG1 or ETOT hardware trigger[1], and whose two largest energy CCAL clusters have an invariant mass above 2.5[2.7] GeV for below[above] transition data.

The analysis cuts purify the $\gamma\gamma$ sample even more. First, the invariant mass of the two largest CCAL clusters is required to be within 20% of $\sqrt{s}$, using cluster thresholds of 5 MeV for the seed and 20 MeV for the total energy. Then, a 4C kinematical fit

[1]Prior to stack 5.3, only the GM4 events were considered by the filter. However, both PBG1 and ETOT are 100% efficient for $\gamma\gamma$ events.

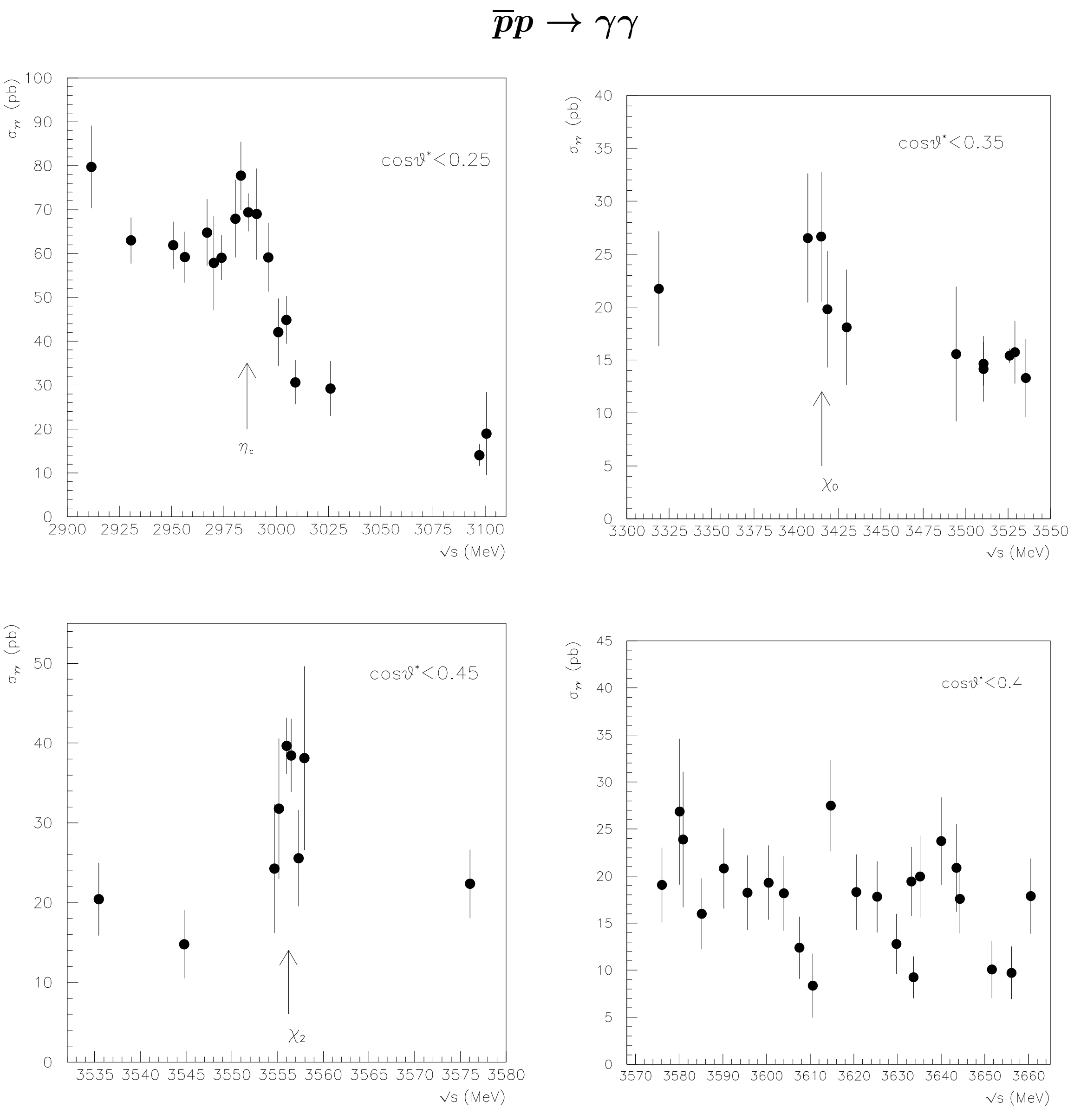

Figure 5.1: The $\gamma\gamma$ signal in the regions around η_c, χ_0, χ_2, and η_c' expected resonances. The arrows indicate the values for the resonance mass in reference [52].

to the $\gamma\gamma$ hypothesis is performed using the SQUAW program [42], and events with a nominal confidence level below 5% are discarded.

The kinematical fit is a minimization of the chi-squared

$$\chi^2 = \sum_{i=1}^{6} \frac{(x_{i,fit} - x_{i,meas})^2}{\sigma^2_{x,i}} \tag{5.1}$$

where the sum is over the six measured quantities, the angles of each photon, $\tan\theta$ and ϕ , and the momentum of each photon. The $\sigma_{x,i}$ are determined from the errors on the cluster energies and angles discussed in section 3.4.4. In the fit, the $x_{i,fit}$ values are required to satisfy energy and momentum conservation, with the zero-mass of the photon as a constraint. If the $x_{i,meas}$ are Gaussian distributed about their true values with standard deviation $\sigma_{x,i}$, then χ^2 is distributed as

$$P(\chi^2) = \frac{\left(\frac{\chi^2}{2}\right)^{(\nu/2-1)} e^{-\chi^2/2}}{2\Gamma\left(\frac{\nu}{2}\right)} \tag{5.2}$$

and ν is the number of independent variables in the χ^2 sum. For each event, the value χ^2_{event} is calculated and the nominal confidence level is the probability of obtaining χ^2_{event} from a random $\gamma\gamma$ event. In other words, the confidence level is a numerical measure of the 'goodness of fit' of the $\gamma\gamma$ hypothesis to the measured quantities.

Unfortunately, a small fraction of the abundant $\pi^0\pi^0$ and $\pi^0\gamma$ events also satisfy these kinematical cuts when the π^0 decays asymmetrically. Further cuts were imposed in an effort to reduce this background. No in-time extra clusters were allowed in the candidate events. Out-of-time extra clusters are disregarded and all undetermined extra clusters were paired with each candidate photon and the event rejected only if the invariant mass of any pair fell within 35 MeV of the π^0 mass (135 MeV). Data from several data-points in the η_c region are shown in figure 5.2, where a clear peak in the invariant mass distribution can be seen at the π^0 mass.

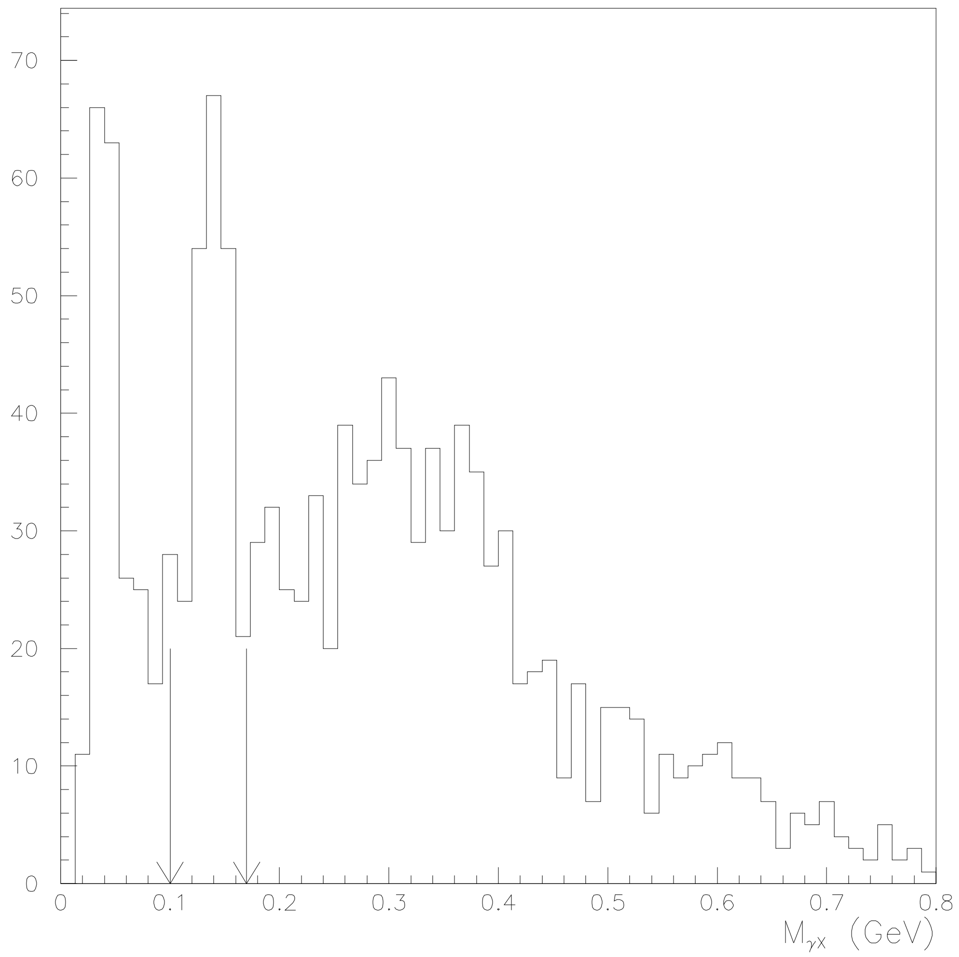

Figure 5.2: The invariant mass of γ candidates and any extra 'undetermined' clusters for data from several data-points in the η_c region. The events satisfy all other analysis cuts, including $|\cos\theta^*| \leq 0.25$. The arrows indicate the region rejected by the cut PI.

Since the $\pi^0\pi^0$ and $\pi^0\gamma$ angular distributions are peaked in the forward direction, an acceptance cut is chosen, $|\cos\theta^*| < \alpha$ to maximize the significance of the signal. The cutoff α is increased for larger s since the background events become increasingly concentrated in the forward region.

Finally, if there are charged tracks associated with both of the photons, then the product of the electron weight index for these tracks is required to be less than 10^{-4}. The electron weight index is a statistic for determining whether a particle is an electron, and is constructed from the information in the hodoscopes, Čerenkov, and CCAL. The electron weight is described in detail in reference [70]. In the $\gamma\gamma$ analysis, this cut eliminates any potential background from e^+e^- events. This is necessary for the data taken at peak of the J/ψ and ψ' resonances, where a small fraction of the e^+e^- decays did not fire either the charged trigger or the neutral veto This small fraction, however, is still much larger than the $\gamma\gamma$ signal. Figure 5.3 shows the ϕ distribution of the events at the J/ψ energy, before (white histogram) and after (shaded histogram) the cut on the electron weight. The e^+e^- events are concentrated in two bins in ϕ that correspond to known *holes* in the logic of the neutral veto. At the J/ψ and ψ' resonances, it is also necessary to exclude from the analysis the region in ϕ corresponding to the holes. The excluded regions are shown as vertical bands in figure 5.3.

The cuts are summarized as follows:

- **TG** - Requirement of either GM4 or GM5 in the trigger (both require neutral veto to be OFF).

- **IM** - The invariant mass of the two largest CCAL clusters is within 20% of $\sqrt{s}$

- **CL** - The confidence level from a 4C kinematical fit at least 5%

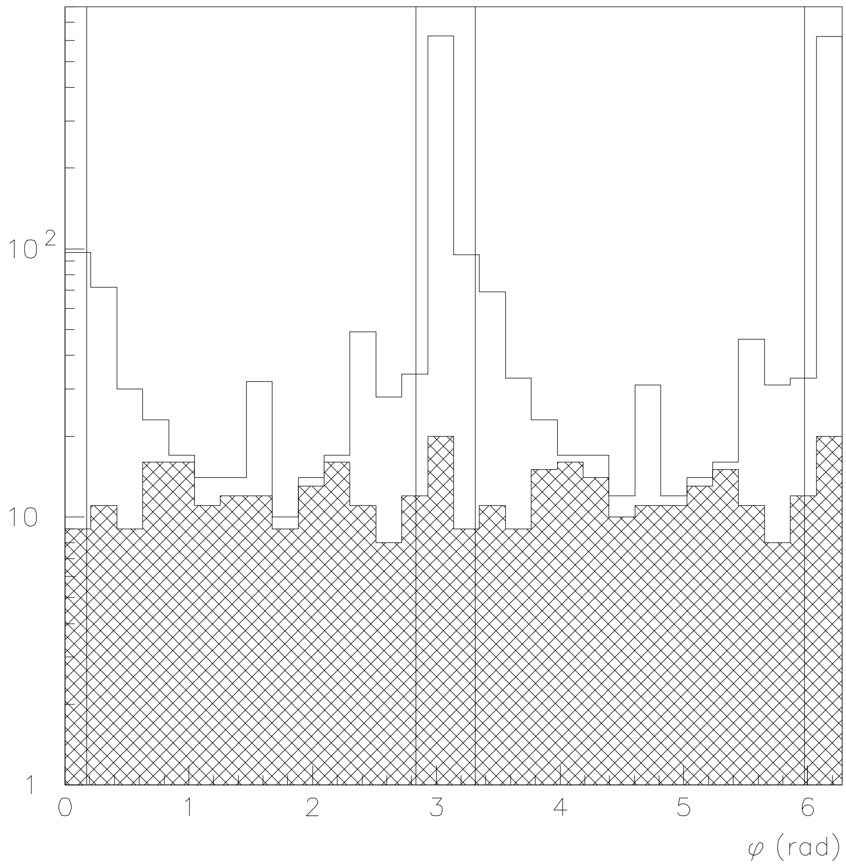

Figure 5.3: The azimuthal angle ϕ for $\gamma\gamma$ candidate events from the J/ψ data-points before and after applying the electron weight cut.

- **XC** - No in-time extra clusters
- **PI** - No undetermined extra clusters that form an invariant mass within 35 MeV of the π^0 mass.
- **EW** - If there are charged tracks associated with both photons, then $EW_1 * EW_2 < 10^{-4}$ is required.

5.2 Efficiencies

The observed number of events is corrected to get the $\gamma\gamma$ signal using the equation

$$\sigma(\overline{p}p \to \gamma\gamma) = \frac{N_{obs}}{\int Ldt} \times \frac{1}{\epsilon_{tot}} \times \frac{1}{\alpha} \tag{5.3}$$

where N_{obs} is the observed number of $\gamma\gamma$ events, L is the instantaneous luminosity, α is the geometrical acceptance of the cuts, and ϵ_{tot} can be broken down as follows

$$\epsilon_{tot} \equiv \epsilon_{analysis} \times \epsilon_{trigger} \times (1 - P_{cont}) \times (1 - P_{conv})^2 \tag{5.4}$$

P_{cont} is the probability that an overlapping event contaminates a good event, causing it to be rejected, and P_{conv} is the probability that either photon converts into a e^+e^- pair before reaching the first detector element (H1).

The final values of ϵ_{tot} for every data-point are listed in appendix A and the calculation of the components are described in detail

5.2.1 Hardware Trigger

The efficiencies of the PBG1 and ETOT components of the neutral trigger are each 100% for the $\gamma\gamma$ data. This is verified with special trigger test runs, discussed in detail in reference [28]. During these runs, $J/\psi \to e^+e^-$ events were accumulated, requiring only a single electron track in the hodoscopes and a CCAL invariant mass above 2.0 GeV. A clean J/ψ sample is selected by requiring exactly two CCAL clusters with energy above 25 MeV and whose centers lie within rings 2 to 18. The product of the electron weight for the two associated tracks is required to be greater than 10, ensuring a clean sample of J/ψ decays. Examining the response of the standard trigger to these events reveals that the PBG1, PBG3, and ETOT bits are 'ON' for every event.

The CCAL invariant mass requirement is necessary for a clean sample of J/ψ events.. It is assumed that the only reason that a J/ψ event, that satisfies the other cuts, would not pass the invariant mass cut is that one of the electrons deposited most of its energy into a CCAL channel which was not working. Dead CCAL channels are a source of inefficiency not accounted for here. Instead, the effect of the dead CCAL channels is included in the analysis efficiency calculated with the Monte Carlo (see figure 5.6).

The only remaining contribution to the trigger efficiency is $1 - f_{study}$, where f_{study} is the fraction of data automatically siphoned off for autopass triggers. These triggers, in particular, ETOT-LO and ETOT-NOVETO, were separated from the rest of the data for efficiency studies. These values of $1 - f_{study}$ for the entire running period are listed in table 5.1 as the trigger efficiency.

data-points	$\epsilon_{trigger}$
4.1 - 4.4	0.998
5.1 - 26.1	0.996
27.1 - 79.7	0.980

Table 5.1: The trigger efficiency for the $\gamma\gamma$ analysis, excluding the effects of overlapping events and dead CCAL channels since they are included elsewhere.

5.2.2 Overlapping events

If a second event occurs close enough in time to the event of interest, the signals it leaves in the detector are recorded as a part of the original event. The original event is now contaminated and may be mistakenly thrown out by the analysis cuts described above if the overlapping event has one of the following

1. The neutral veto on. (TG)

2. One or more in-time clusters in the CCAL. (XC)

3. One or more undetermined clusters in the CCAL that form an invariant mass within the window [100,170] MeV when combined with a photon from the $\gamma\gamma$ event. (PI)

This effect is studied with events from the random gate trigger. Cuts 1 and 2 are applied sequentially to the random gate data, and the results plotted in figure 5.4 for a subset of the data-points with the same CCAL shaper board thresholds and hodoscope thresholds. To obtain the efficiency of cut 3, one thousand $\gamma\gamma$ events are generated for each data-point. Each generated event that satisfies the the CL cut is combined with every random gate event and the fraction of combinations passing all three cuts plotted as circles in figure 5.4 as the combined efficiency.

5.2.3 Analysis

The term $\epsilon_{analysis}$ in equation 5.4 refers to the fraction of good $\gamma\gamma$ events that satisfy the analysis cuts (CL and IM). These cuts are studied using a Monte Carlo simulation of the CCAL. The Monte Carlo itself is discussed in detail in section 4.1. The results from the simulation are shown in figure 5.5, as a function of $\cos\theta^*_\gamma$, for

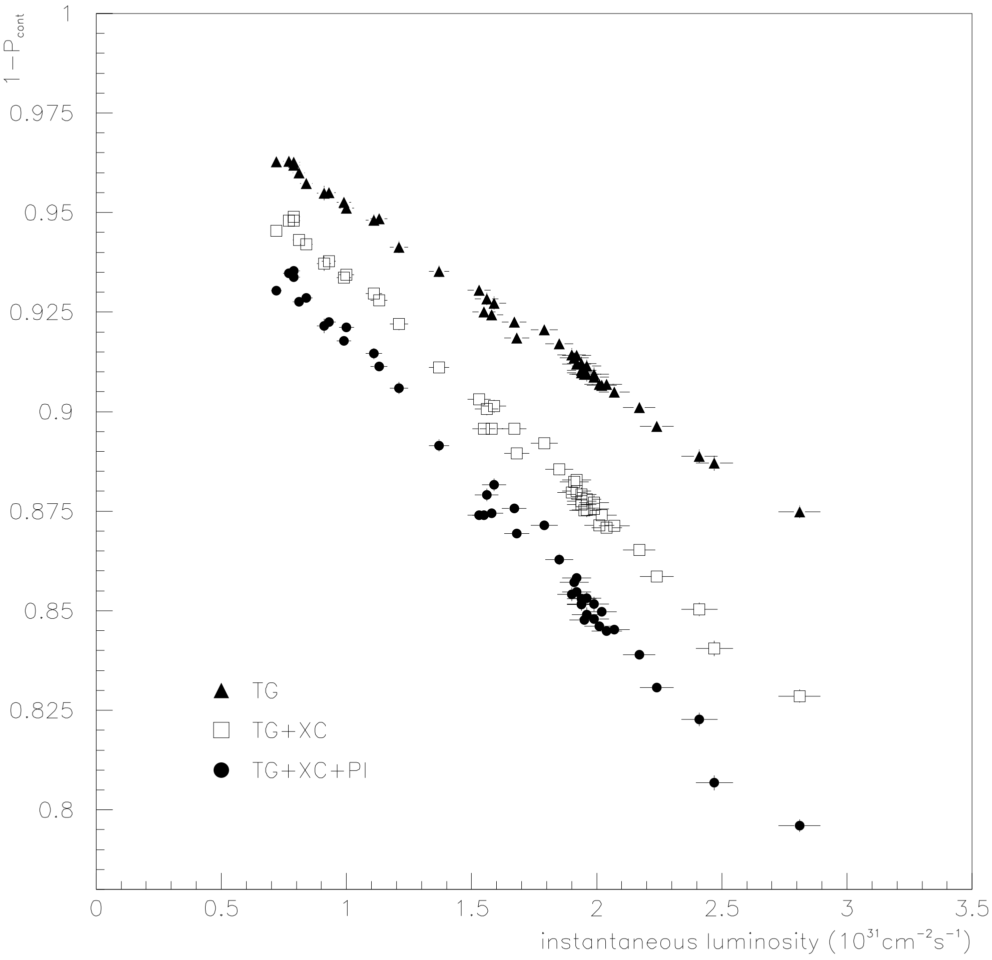

Figure 5.4: The efficiency of the cuts TG,XC, and PI when applied sequentially for stacks 8-27. The horizontal error bars reflect the 3% uncertainty in the luminosity measurement and the vertical error bars are statistical, from the number of random gate events.

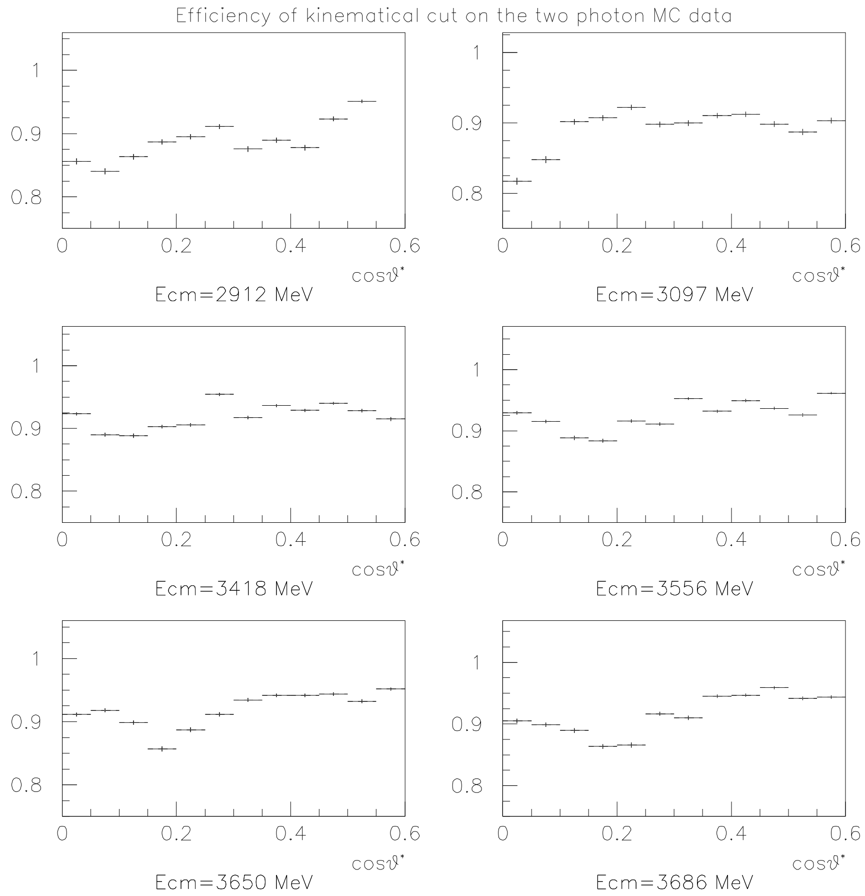

Figure 5.5: The efficiency of the analysis cuts (CL and IM) calculated with the Monte Carlo for many values of $\sqrt{s}$.

different values of $\sqrt{s}$. The noticable dip is a result of the three dead CCAL channels, two in ring 8 and one in ring 7.

To verify the Monte Carlo results, data from 5 different data-points at the J/ψ are considered. Clean e^+e^- events are selected as described in the previous section. The energy of the electron clusters is scaled by 1.015 prior to applying the cuts to compensate for the average energy lost by the electrons in interactions in the material encountered before the CCAL.

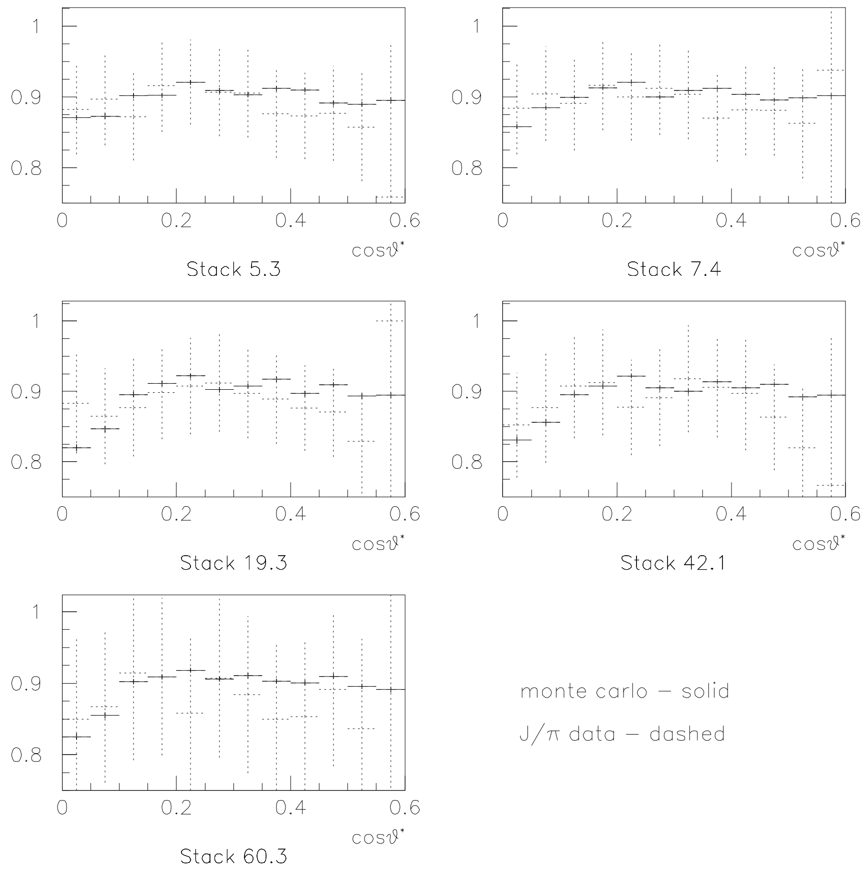

Figure 5.6: The efficiency of the analysis cuts (CL and IM) at the J/ψ resonance, calculated using the Monte Carlo (solid) and a sample of clean e^+e^- events (dashed).

Figure 5.6 shows both calculations of the analysis efficiency for each of the five data-points taken at the J/ψ resonance. The efficiencies are consistent within the statistical errors. In both studies, there are no events that satisfy the confidence level cut and do not satisfy the invariant mass cut. The invariant mass cut is retained merely to eliminate events before performing the kinematical fit, which is time consuming.

These discussions provide a qualitative understanding of the impact of the individual cuts; however, the product $\epsilon_{analysis} \times (1 - P_{cont})$ is in practice calculated as a single number using the standard Monte Carlo, where the random gate triggers are superimposed on the events before clusters are formed. For every data-point, 100000 $\gamma\gamma$ events are generated and $\epsilon_{analysis} \times (1 - P_{cont})$ is the fraction of Monte Carlo events that survive all the analysis cuts. This fraction is used to calculate the values of ϵ_{tot} in appendix A.

5.3 Acceptance Restrictions

The angular distribution of the background is peaked in the forward (small θ) region. Since the angular distribution of the charmonium resonances are essentialy flat within the detector acceptance (see section 6.2), a restriction on $\cos\theta^*$. will improve the statistical significance of the charmonium signal. Figure 5.7 shows the background and the data at many values of $\sqrt{s}$. The background shown in the plots is from the feeddown calculation, any contribution from the $\gamma\gamma$ continuum is neglected in this discussion.

It is preferable to determine such an acceptance cut *a priori*, before looking at the results. The ratio of the maximum values of the likelihood function for the resonance and no-resonance hypotheses provides a measure of the statistical significance of a resonance signal above a known background. Let $\lambda = 2\ln(\frac{L_{max}(H1)}{L_{max}(H0)})$, where $L_{max}(H1)$ is the maximum value of the likelihood function for the resonance plus background hypothesis, while $L_{max}(H0)$ is the maximum value of the likelihood function for the background only (null) hypothesis. We chose a critical value, $\lambda = \lambda_c$, and reject the null hypothesis if $\lambda > \lambda_c$. Such a test has a significance S and a power P for discriminating between the two hypotheses. S is the probability to reject H0 when it is actually true, and P is the probability to accept H1 when it is actually true. For a given value of S, P is a measure of the separation of the two probability distributions for λ, one under the hypothesis H1 and the other under H0. For the E835 case, $L_{max}(H0)$ is a constant, independent of α. Thus maximizing λ is essentially maximizing P, or the power to discriminate between the resonant and non-resonant hypotheses.

The background cross section is obtained from the feeddown calculation, fitting the results to a fourth degree polynomial. It is assumed that background is known perfectly, and that it is independent of $\sqrt{s}$ in the region spanned by the resonance. Using Poisson statistics, the likelihood function is written

$$L = \prod_{j=1}^{N} \frac{\nu_j^{n_j} e^{-\nu_j}}{n_j!} \tag{5.5}$$

where n_j is the observed number of events and ν_j the expected number of events for the *jth* data point. The best value for α is the one that maximizes λ. It will be shown that this value of α is sensitive to the angular distribution of the background, and rather insensitive to the resonance parameters assumed.

First consider the case of a single data-point taken at the resonance peak energy. Then, λ can be written

$$\begin{aligned} \frac{\lambda}{2} = \ln\left(\frac{L_{max}(H1)}{L_{max}(H0)}\right) &= n \ln\left(\frac{\hat{\nu_1}}{\nu_0}\right) - (\hat{\nu_1} - \nu_0) \\ \nu_1 &= \epsilon \int Ldt \times \left(\sigma_{bkgd}(\alpha) + \alpha\sigma_{peak}\right) \\ \nu_0 &= \epsilon \int Ldt \times \sigma_{bkgd}(\alpha) \end{aligned}$$

where $\int Ldt$ is the integrated luminosity, ϵ is the total efficiency, and $\hat{\nu_1}$ denotes the best estimator of ν_1 from the likelihood fit.

The above equations are combined to give the following expression for λ

$$\frac{\lambda}{2} = \epsilon \int Ldt \times \left[\left(\sigma_{bkgd}(\alpha) + \alpha\sigma_{peak}\right) \times \ln\left(\frac{\sigma_{bkgd}(\alpha) + \alpha\sigma_{peak}}{\sigma_{bkgd}(\alpha)}\right) - \alpha\sigma_{peak}\right] \tag{5.6}$$

This equation is extended to several data points by assuming that $\hat{\nu_{1,i}} = n_i$.

$$\begin{aligned}\frac{\lambda}{2} &= \sum_{j=1}^{N}\left[\left[\epsilon\int Ldt\right]_j \times \left[\left(\sigma_{bkgd}(\alpha)+\alpha\sigma_{peak}C_j\right)\times\right.\right.\\ &\qquad \left.\left.\ln\left(\frac{\sigma_{bkgd}(\alpha)+\alpha\sigma_{peak}C_j}{\sigma_{bkgd}(\alpha)}\right)-\alpha\sigma_{peak}C_j\right]\right] \qquad (5.7)\end{aligned}$$

where C_j depends on the beam energy distribution, $f_j(\sqrt{s})$, and is given by

$$C_j = \frac{1}{\sigma_{peak}}\int f_j(\sqrt{s'})\frac{\Gamma_R^2}{4(\sqrt{s'}-M_R)^2+\Gamma_R^2}d\sqrt{s'} \qquad (5.8)$$

The assumption $\hat{\nu_{1,i}} = n_i$ is equivalent to neglecting the statistical fluctuations in the n_i, i.e. treating the fit as in the limit of an infinite number of events. This expression for λ is maximized to determine the acceptance cut.

Figure 5.8 shows the function λ for the four resonances considered. For the χ_2 equation 5.7 has been modified to include the angular distribution of the $\gamma\gamma$ decay, which is discussed in appendix F. The luminosity and efficiency of actual data-points are used, and the resonance parameters are taken from the PDG [52], except for the η_c', where $M = 3600$ MeV, $\Gamma = 10$ MeV, and $\sigma_{peak} = 1$ pb are used. The curve for the η_c' resonance is shifted to the left of the χ_2 curve because of the small signal expected. Values for α corresponding to the maximums in λ are listed in Table 5.2. Also listed are the cut values used, which are constrained to be integer multiples of 0.05 by the binning. At the χ_0, a larger value of α (0.35 instead of 0.30) is deliberately chosen to improve the continuity of the background, discussed in detail in section 6.7.

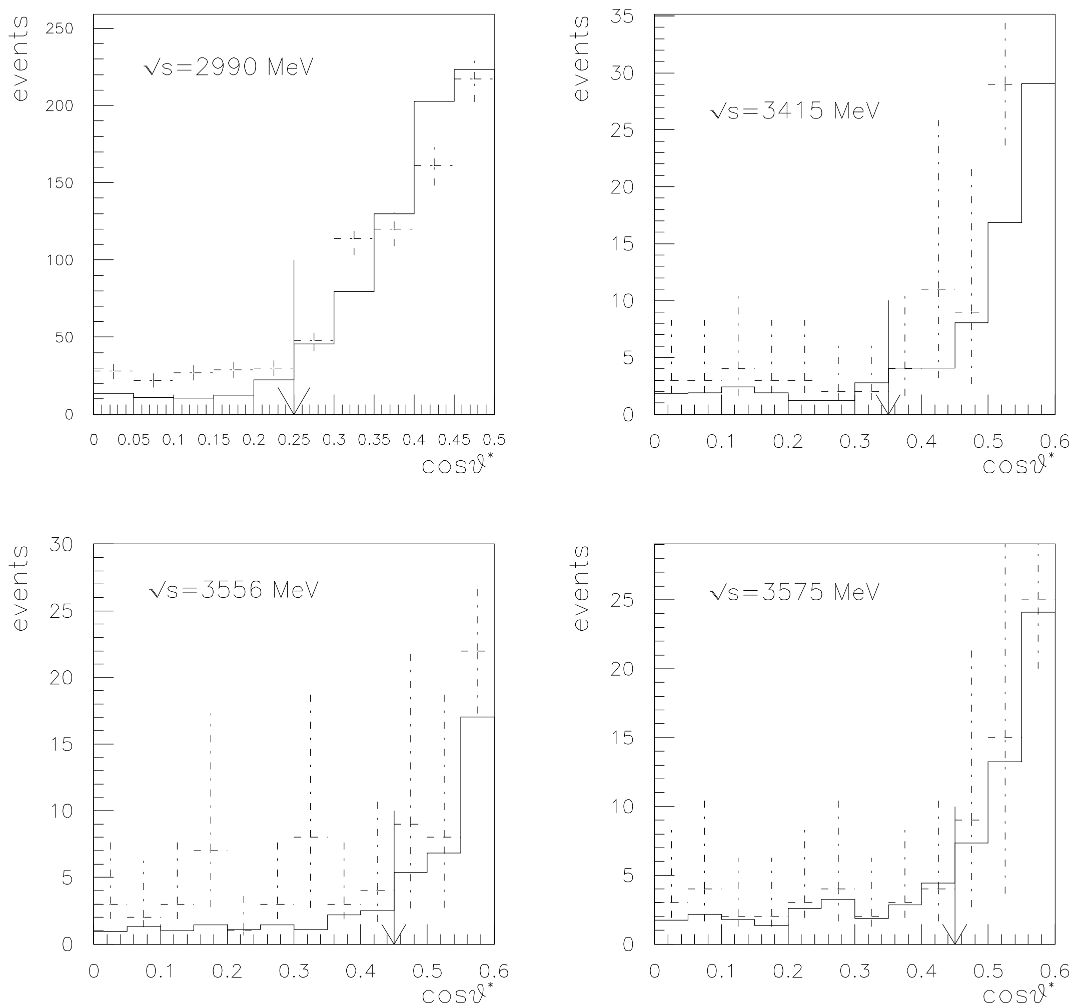

Figure 5.7: The feeddown calculation of the background is shown with the data for different values of $\sqrt{s}$. The arrows indicate where the acceptance cuts were chosen.

resonance	α_{max}	α_{cut}
η_c	0.25	0.25
χ_0	0.31	0.35
χ_2	0.46	0.45
η_c'	0.42	0.40

Table 5.2: α_{max} is the value that maximizes λ, while α_{cut} is the value used in the acceptance cut $|\cos(\theta^*)| \leq \alpha$.

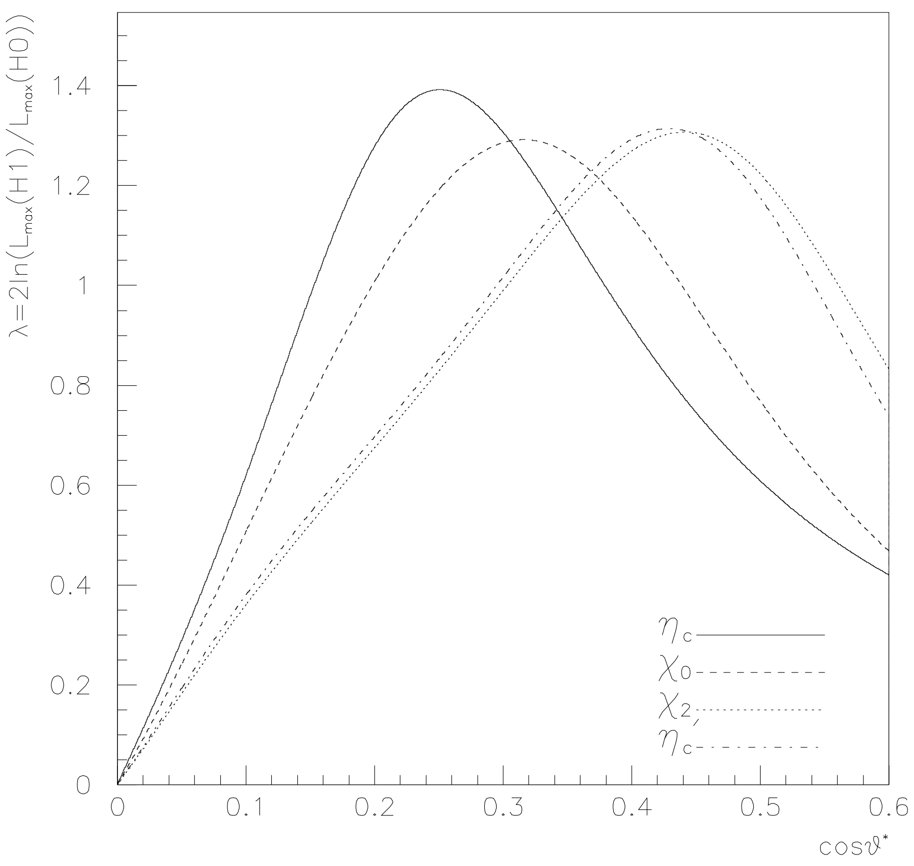

Figure 5.8: λ as a function of the acceptance cut for each of the four resonances studied. The curves have been normalized to contain the same area.

Chapter 6

Results

6.1 Determination of Resonance Parameters

The expected shape of the measured data is the sum of a background curve and a Breit-Wigner resonance curve convolved with the normalized distribution $f_i(\sqrt{s})$ of the antiproton beam for the ith data-point. To extract the resonance parameters, a likelihood function is written assuming Poisson statistics, and the curve that best fits the data is given by the set of parameters $\{\ M_R, \Gamma_R, \sigma_{peak}, A, B\ \}$ that minimizes the function $-\ln(L)$. The likelihood function and its parameters are

$$L = \prod_{j=1}^{N} \frac{\nu_j^{n_j} e^{-\nu_j}}{n_j!} \tag{6.1}$$

where n_j is the observed number of events and ν_j the expected number of events for the *jth* data-point, calculated as follows

$$\begin{aligned} \nu_j \quad &= \quad \left[\epsilon_{tot} \times \int Ldt\right]_j \times \qquad (6.2)\\ &\left[\sigma_{bkgd}(\sqrt{s}) + a\sigma_{peak} \int f_j(\sqrt{s'}) \frac{\Gamma_R^2}{4(\sqrt{s'} - M_R)^2 + \Gamma_R^2} d\sqrt{s'}\right] \end{aligned}$$

$$\sigma_{peak} = \frac{(2J+1)\pi}{k^2} \times B_{\overline{p}p} \times B_{\gamma\gamma} \tag{6.3}$$

$$\sigma_{bkgd} = A \times \left(\frac{\sqrt{s_0}}{\sqrt{s}} \right)^B \tag{6.4}$$

Here $k^2 = \frac{M_R^2 c^2 - 4m_p^2 c^2}{4\hbar^2 c^2}$, m_p is the mass of the proton, B_X is the branching ratio for the resonance to decay to the final state X. J is the total angular momentum of the $\bar{c}c$ resonanant state and a is the acceptance of the geometrical cut on $|\cos\theta^*|$. s_0 is a fixed constant, chosen at each resonance so that A is the value of the background cross section at the nominal resonance peak. The power law parameterization of the background is suggested by theory[38].

The likelihood function in equation 6.1 can be modified to include the the feeddown calculation as well

$$L = \prod_{j=1}^{N_{data}} \frac{\nu_j^{n_j} e^{-\nu_j}}{n_j!} \times \prod_{k=1}^{N_{feed}} \frac{1}{\sqrt{2\pi}\sigma_k} e^{\left(n_k - \epsilon_{tot,k}\left[\int L dt\right]_k \sigma_{feed,k}\right)^2 / 2\sigma_k^2} \tag{6.5}$$

where N_{feed} is the number of feeddown points calculated and N_{data} is the number of data-points taken. σ_k is the Gaussian error on n_k, the calculated number of feeddown events , and σ_{feed} is the effective feeddown cross section, parameterized as a function of s. The parameterization is discussed later in this chapter. σ_k includes both the systematic and statistical terms discussed in section 4.5. In equation 6.4, σ_{bkgd} includes contributions from both the continuum and the feeddown, while σ_{feed} in equation 6.5 is only the contribution from the continuum. The details of the background treatment are presented along with the measurements at the individual resonances.

6.2 Angular Distributions of $\gamma\gamma$ decays

Calculating the acceptance, a in equation 6.1, requires the functional form of the angular distribution, $d\sigma(\bar{p}p \to \bar{c}c \to \gamma\gamma)/d(\cos\theta^*)$. Unfortunately, our charmonium data sample does not have enough statistics to yield a measurement of the angular distributions of the $\gamma\gamma$ decays. Instead, theoretical formulae for the angular distributions are used to calculated the acceptances. For the η_c, η_c', and χ_0, the angular distributions are assumed isotropic since the states are spin 0 particles.

The angular distribution for the process $\overline{p}p \to \chi_2 \to \gamma\gamma$ is given by

$$\frac{d\sigma(\overline{p}p \to \chi_2 \to \gamma\gamma)}{d(\cos\theta^*)} \propto \left[K_1 + K_2\cos^2\theta^* + K_3\cos^4\theta^*\right] \tag{6.6}$$

The coefficients, K_i, are related to the helicity amplitudes for the initial and final states. The initial state can have helicity, $\lambda = 0, 1$, resulting in the amplitudes B_0 and B_1. The final state can have helicity, $\nu = 0, 2$, corresponding to amplitudes A_0 and A_2.

$$\begin{aligned}
K_1 &\equiv (2A_2^2)R + (2A_0^2 + 3A_2^2)(1-R) \\
K_2 &\equiv (12A_0^2)R + (-12A_0^2 - 6A_2^2)(1-R) \\
K_3 &\equiv (-12A_0^2 - 2A_2^2)R + (18A_0^2 + 3A_2^2)(1-R) \\
R &\equiv \frac{2B_1^2}{B_0^2 + 2B_1^2}
\end{aligned} \tag{6.7}$$

The constant R measures the fractional contribution of the helicity one production process. The factor of two appears because the helicities $\lambda = \pm 1$ contribute equally. This result is derived in appendix F. The production amplitudes have been measured by E760[13] with the process $\overline{p}p \to \chi_2 \to J/\psi\gamma \to e^+e^-\gamma$. The value R=1.0 is the best fit to the data; alternatively, $R \geq 0.78$ with 90% confidence. Perturbative QCD predicts that the helicity zero component vanishes in the limit of massless quarks; and a small contribution is expected when non-zero quark masses and non-perturbative effects are included, $R \sim 0.84 - 0.92$[13]. The decay amplitude has not been measured, but theory places tight limits on the ratio A_0^2/A_2^2, which must vanish in the non-relativistic limit and correction terms are very small. For example, Li, Close and Barnes[64] calculate that $A_0^2/A_2^2 < 0.005$ with all relativistic corrections included. Ignoring the helicity zero components in both the formation and decay processes, the angular distribution is given by

$$\frac{d\sigma(\overline{p}p \to \chi_2 \to \gamma\gamma)}{d(\cos\theta^*)} \propto (1 - cos^4\theta^*) \tag{6.8}$$

Integrating the angular distribution over the acceptance region $|\cos\theta^*| < 0.45$ gives an acceptance $a = 0.56 \pm 0.02$, where the error comes from the uncertainty in the magnitude of the neglected terms.

6.3 χ_2 results

The mass and width of the χ_2 are already well determined experimentally [52] [14]. The partial width, $\Gamma(\chi_2 \to \gamma\gamma)$ was well measured in E760 to be 0.32 ± 0.09 keV. This measurement is improved using the E835 data.

To extract the partial width from the E835 data, the likelihood function from equation 6.1 is maximized with the mass and width of the χ_2 fixed to $M_{\chi_2} = 3556.17$ MeV and $\Gamma_{\chi_2} = 2.0$ MeV[52]. The background is well constrained by the data taken during the $^1P_1$ search ($3525\ MeV < \sqrt{s} < 3530$ MeV) and at the ψ' resonance (3686 MeV), so the feeddown calculation is not necessary. The acceptance cut of $|\cos\theta^*| \leq 0.45$ optimizes the significance of the signal, as discussed in section 5.3. The data are shown in figure 6.1, and the results of the fit are tabulated in table 6.1 for three different acceptance cuts.

The result for the partial width is $\Gamma_{\gamma\gamma}(\chi_2) = 0.252 \pm^{0.042}_{0.040} \pm^{0.028}_{0.023} \pm 0.017$ keV. It includes a systematic error from the uncertainty in the $\overline{p}p$ branching ratio and a smaller systematic error from the uncertainty in the resonance width.

The branching ratio $B(\chi_2 \to \gamma\gamma)$ can also be obtained from the quantity R, the

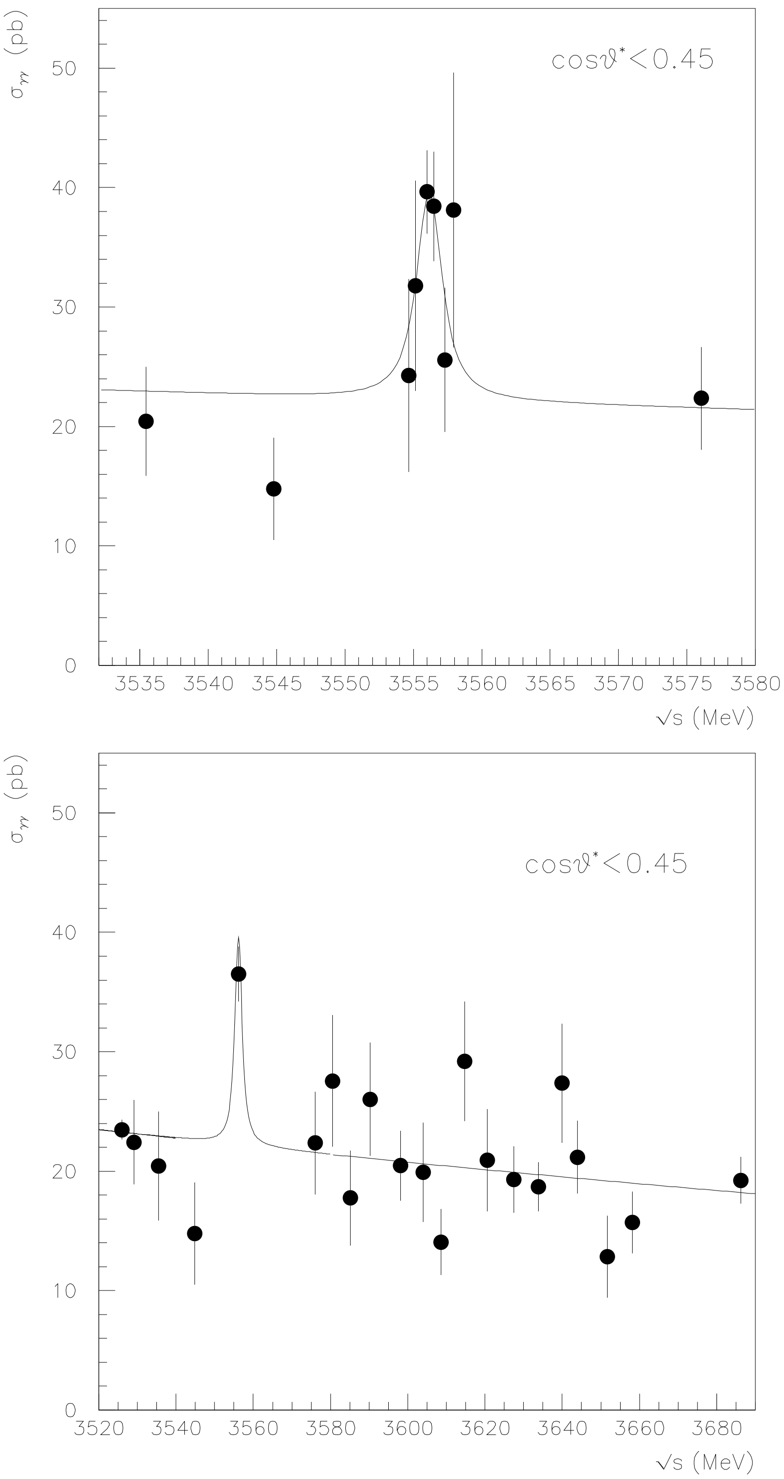

Figure 6.1: Data used to determine $\Gamma(\chi_2 \to \gamma\gamma)$. The upper plot has data bins in $\sqrt{s}$ of 0.75 MeV to show the detail near the χ_2 resonance. The lower plot has data bins in $\sqrt{s}$ of 5.0 MeV and shows the shape of the background.

$\cos\theta^*$	0.40	0.45	0.50
$B_{\overline{p}p} \times B_{\gamma\gamma} \times 10^8$	$1.33\pm^{0.22}_{0.21}$	$1.26\pm^{0.21}_{0.20}$	$1.30\pm^{0.21}_{0.21}$
$\Gamma_{\gamma\gamma}$ (KeV)	$0.266\pm^{0.044}_{0.042}$	$0.252\pm^{0.042}_{0.041}$	$0.261\pm^{0.043}_{0.041}$
A (pb)	$18.21\pm^{0.55}_{0.54}$	$22.19\pm^{0.60}_{0.59}$	$29.53\pm^{0.69}_{0.68}$
B	$4.77\pm^{1.88}_{1.86}$	$5.51\pm^{1.71}_{1.70}$	$8.76\pm^{1.52}_{1.51}$
χ^2/N_{DF}	81.69 / 76	78.69 / 76	71.52 / 76
λ	51.5	49.1	49.8
α	0.50	0.56	0.62
Events	216	249	312

Table 6.1: The results of the maximum likelihood fit to the χ_2 resonance for three different acceptance cuts. The mass and total width of the χ_2 are fixed to the values $M_{\chi_2} = 3556.17$ MeV and $\Gamma_{\chi_2} = 2.0$ MeV respectively. $\Gamma_{\gamma\gamma}$ is calculated using the value $BR(\chi_2 \to \overline{p}p) = 1.0 \pm 0.1 \times 10^4$. [52]

ratio of the two branching ratios, defined as follows

$$R \equiv \frac{B(\chi_2 \to \gamma\gamma)}{B(\chi_2 \to J/\psi\gamma \to e^+e^-\gamma)} = \frac{\sigma(\overline{p}p \to \chi_2 \to \gamma\gamma)}{\sigma(\overline{p}p \to \chi_2 \to J/\psi\gamma \to e^+e^-\gamma)} \tag{6.9}$$

The details of the $J/\psi\gamma$ event selection can be found in reference [67]. Written in terms of number of events, the ratio for a single data-point, is as follows

$$R_i = \frac{\frac{1}{a_{\gamma\gamma}\epsilon_{\gamma\gamma}}\left[N_{\gamma\gamma} - N_{bkgd,\gamma\gamma}\right]}{\frac{1}{a_{\psi\gamma}\epsilon_{\psi\gamma}}\left[N_{\psi\gamma} - N_{bkgd,\psi\gamma}\right]} \tag{6.10}$$

N is the number of events, a is the geometrical acceptance, and ϵ is the combined analysis and trigger efficiency. N_{bkgd} is the number of background events in each channel. The background cross section is a parameter of the resonance fit in the previous section. To simplify the calculation of R, it is assumed that the background cross section is constant underneath the resonance in both final states. The number of background events is then given by the equations:

$$N_{bkgd,\gamma\gamma} = \epsilon_{\gamma\gamma}\sigma_{bkgd,\gamma\gamma}\int Ldt \tag{6.11}$$

$$N_{bkgd,\psi\gamma} = \sigma_{bkgd,\psi\gamma}\epsilon_{\psi\gamma}a_{\psi\gamma}\int Ldt \tag{6.12}$$

$\sqrt{s}$ (MeV)	$\int Ldt(pb^{-1})$	$N_{\psi\gamma}$	$N_{\gamma\gamma}$	$\epsilon_{\gamma\gamma}$
3557.302	0.908680	349	18	0.7855
3556.761	0.400580	143	11	0.7576
3556.645	0.810300	401	28	0.7289
3556.326	0.752350	462	18	0.7536
3556.180	0.512270	348	14	0.7794
3556.078	0.413360	254	10	0.7541
3555.989	0.994190	550	34	0.7418
3555.922	0.516410	298	16	0.7424
3555.575	0.411000	192	12	0.7570
3555.164	0.519350	232	13	0.7880
total	6.24	3347	183	

Table 6.2: The individual data points used to calculate R.

$\sigma_{bkgd,\psi\gamma}$	6.06 ± 0.86 pb
$\sigma_{bkgd,\gamma\gamma}$	22.2 ± 0.6 pb
$a_{\psi\gamma}\epsilon_{\psi\gamma}$	0.35 ± 0.01
$a_{\gamma\gamma}$	0.56 ± 0.02

Table 6.3: Parameters used to calculate R.

The two formulae differ slightly since σ_{bkgd} is defined differently in the two cases; the acceptance term is included in the definition σ_{bkgd} for the $\psi\gamma$ analysis and not included in the definition of σ_{bkgd} for the $\gamma\gamma$ analysis . The values of σ_{bkgd}, a, and ϵ are given in table 6.3. The values of $\epsilon_{\gamma\gamma}$ depend upon the instantaneous luminosity, while the value of $\epsilon_{\psi\gamma}$ varies less than 1% for the data-points considered[69], and is assumed constant when calculating R.

The individual R_i are useful for studying possible systematic effects. Figures 6.2 and 6.3 show R_i as a function of instantaneous luminosity and center of mass energy respectively. A variation with instantaneous luminosity suggests an error in $\epsilon_{\gamma\gamma,i}$, while a variation with center-of-mass energy suggests an error in the background determination. A variation is not seen in either case.

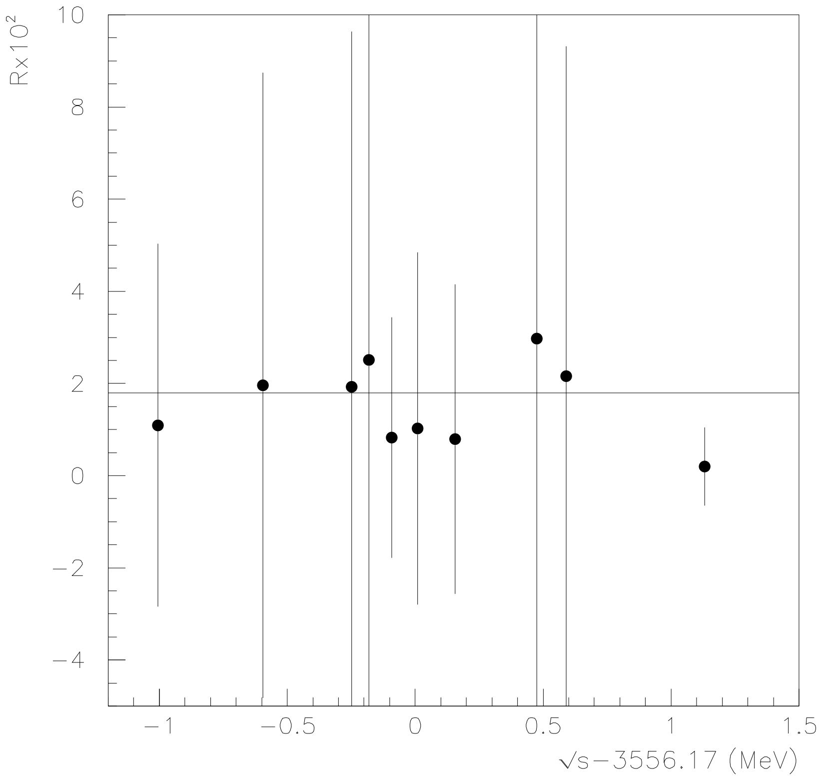

Figure 6.2: The ratio R for each data-point is plotted against the instantaneous luminosity.

The information from all the points can be combined into a single value of R as follows

$$R = \frac{\frac{1}{a_{\gamma\gamma}}\left[\sum_i \left(\frac{1}{\epsilon_{\gamma\gamma}}\right)_i \left(N_{\gamma\gamma} - N_{bkgd,\gamma\gamma}\right)_i\right]}{\frac{1}{\epsilon_{\psi\gamma} a_{\psi\gamma}}\left[\sum_i \left(N_{\psi\gamma} - N_{bkgd,\psi\gamma}\right)_i\right]} \tag{6.13}$$

Using the numbers from tables 6.2 and 6.3, the branching ratio and partial width are calculated from equation 6.9.

$$R = (1.79 \pm 0.36) \times 10^{-2} \tag{6.14}$$

$$B(\chi_2 \to \gamma\gamma) = (1.45 \pm 0.29 \pm 0.13) \times 10^{-4} \tag{6.15}$$

$$\Gamma(\chi_2 \to \gamma\gamma) = 0.290 \pm 0.058 \pm 0.025 \pm 0.026 \text{ keV} \tag{6.16}$$

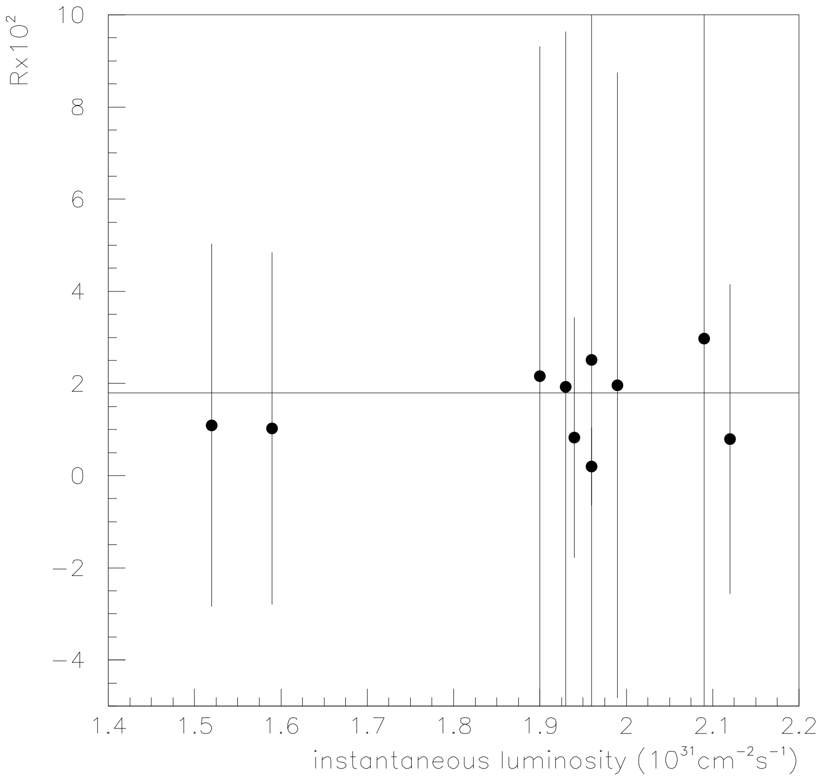

Figure 6.3: The ratio R for each data-point is plotted against $\sqrt{s}$.

The error on R is dominated by the low statistics of the $\gamma\gamma$ analysis. The uncertainties in $a_{\gamma\gamma}$ and $a_{\psi\gamma}\epsilon_{\psi\gamma}$ contribute less than 3% each to the total error, and the uncertainty in $\sigma_{bkgd,\gamma\gamma}$ less than 5%. The first error on the partial width is statistical, the second and third are systematic and come from the branching ratio $B(\chi_2 \rightarrow J/\psi\gamma) \times B(J/\psi \rightarrow e^+e^-) = (0.81 \pm 0.07) \times 10^{-2}$ and the error on the width of the χ_2, $\Gamma = 2.00 \pm 0.18$ MeV[52].

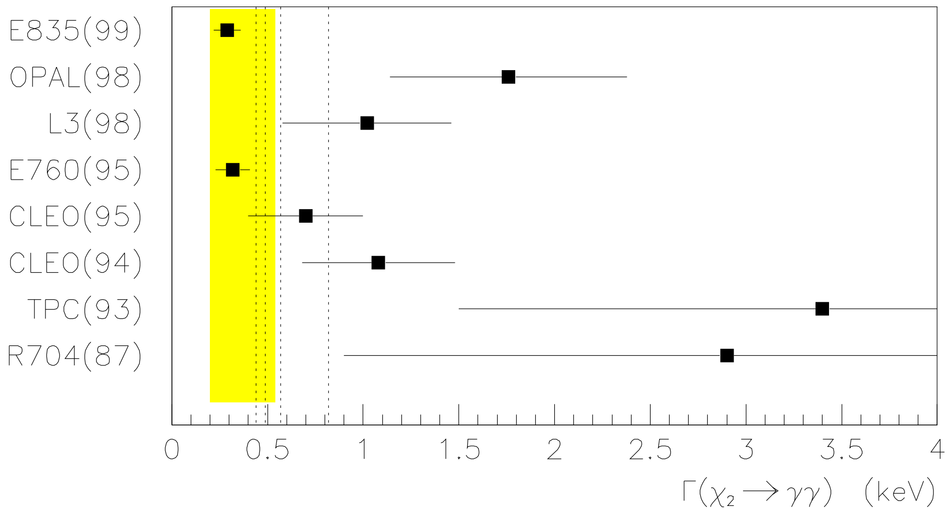

Figure 6.4: Current measurements of the two-photon partial width of the χ_2.

This result can be compared with the result of the resonance fit discussed previously.

$$B(\chi_2 \to \gamma\gamma) = (1.26 \pm 0.21 \pm 0.08) \times 10^{-4} \tag{6.17}$$

$$\Gamma(\chi_2 \to \gamma\gamma) = 0.252 \pm^{0.042}_{0.041} \pm^{0.028}_{0.023} \pm 0.017 \text{ keV} \tag{6.18}$$

The two results are in agreement. The systematics involved with each approach are independent, thus the agreement between the results indicates that the systematics are reasonably understood. The result of the second method is chosen as the final result because the first method is sensitive to the measured beam energy. The previous measurements of the partial width are shown in figure 6.4, with the E835 measurement included. Although consistent with theoretical predictions, the χ_2 partial width is somewhat lower than other measurements using $\gamma\gamma$ production. The measurements of the process $\gamma\gamma \to \chi_2 \to J/\psi\gamma \to l^+l^-\gamma$ from three different experiments employ similar analysis cuts, and perhaps have a common systematic error. The measurement labeled CLEO(95), using a hadronic final state, is in agreement with out result.

6.4 η_c results

A strong signal is seen from the $\eta_c \to \gamma\gamma$ decay, however the background is much larger at these lower values of s. Also, the possibility of a non-negligible continuum signal must be considered. The results are presented in three steps. First, the data listed in appendix A are fit by finding the maximum of the likelihood function in equation 6.1. The free parameters in the fit are $M_R, \Gamma, \sigma_{peak}, A, B$. Second, the background calculated for each data-point is included using the likelihood function in equation 6.5 with $\sigma_{bkgd} = \sigma_{feed}$, parameterized as equation 6.4, neglecting any contribution from the continuum.

Third, a different parameterization of σ_{bkgd} is used, that explicitly includes a contribution from the continuum

$$\begin{aligned} \sigma_{bkgd} &\equiv \sigma_{feed} + \sigma_{continuum} \\ &\equiv A\left(\frac{\sqrt{s_0}}{\sqrt{s}}\right)^B + C\left(\frac{\sqrt{s_0}}{\sqrt{s}}\right)^D \end{aligned} \tag{6.19}$$

where $\sqrt{s_0} = 2990$ MeV. The data and feeddown points are fit to find the values of the parameters $M_R, \Gamma, \sigma_{peak}, A, B, C$ that maximize the likelihood function. The value of D is fixed to give the fitter a necessary additional constraint. Two values are considered. $D = 12$ is suggested by dimensional counting[38], and $D = 10$ is suggested by more recent papers [46][60].

The results of each fit are displayed in tables 6.4 and 6.5. for three different acceptance cuts and each of the three background treatments. Figure 6.5 shows the $\gamma\gamma$ signal, the feeddown calculation, and the curve that best fits the data and the feeddown, neglecting any contribution from the continuum.

The first and third treatments yield very similar results for the resonance parameters, not surprisingly since the third treatment essentially divides the background

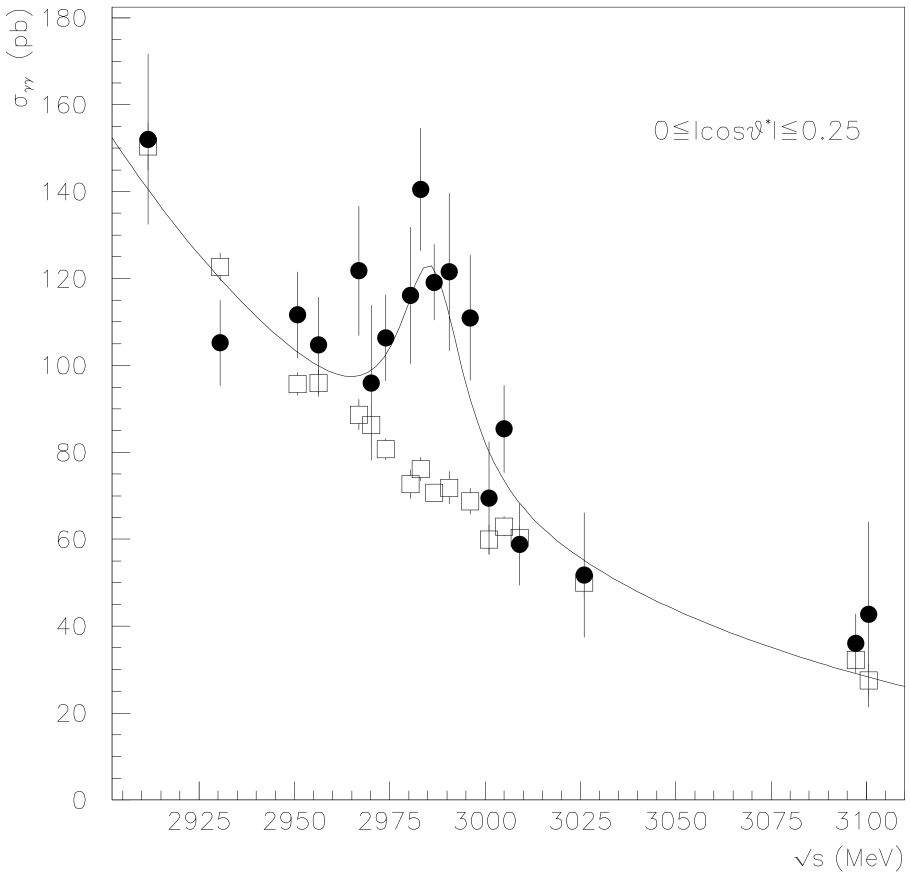

Figure 6.5: The data (circles) and feeddown calculation (squares) at the η_c.

$\cos\theta^*$	0.15	0.20	0.25	0.30
M_{η_c} (MeV)	$2985.01\pm^{2.24}_{2.20}$	$2984.99\pm^{1.90}_{1.92}$	$2985.44\pm^{2.08}_{2.00}$	$2985.10\pm^{2.16}_{1.94}$
Γ_{η_c} (MeV)	$19.45\pm^{7.60}_{6.36}$	$18.42\pm^{7.42}_{6.50}$	$21.15\pm^{7.47}_{6.20}$	$19.22\pm^{7.30}_{6.39}$
$B_{\overline{p}p} \times B_{\gamma\gamma} \times 10^8$	$23.35\pm^{4.14}_{4.01}$	$22.72\pm^{3.69}_{3.59}$	$21.83\pm^{3.36}_{3.31}$	$20.45\pm^{3.39}_{3.33}$
$\Gamma_{\gamma\gamma}$ (KeV)	$3.78\pm^{1.56}_{1.34}$	$3.49\pm^{1.46}_{1.29}$	$3.85\pm^{1.46}_{1.25}$	$3.28\pm^{1.33}_{1.18}$
A (pb)	$35.11\pm^{3.23}_{3.32}$	$49.43\pm^{4.04}_{4.16}$	$71.02\pm^{4.82}_{5.05}$	$110.89\pm^{5.77}_{6.03}$
B	$22.35\pm^{4.12}_{3.89}$	$23.40\pm^{3.57}_{3.37}$	$22.84\pm^{2.98}_{2.83}$	$24.52\pm^{2.39}_{2.29}$
χ^2/N_{DF}	34.47 / 35	32.85 / 35	30.65 / 35	30.45 / 35
λ	205.5	220.0	234.2	249.6
Events	716	969	1370	2038

$\cos\theta^*$	0.15	0.20	0.25	0.30
M_{η_c} (MeV)	$2985.23\pm^{2.19}_{2.08}$	$2985.04\pm^{1.90}_{1.87}$	$2985.88\pm^{2.05}_{1.96}$	$2985.08\pm^{2.23}_{1.72}$
Γ_{η_c} (MeV)	$17.85\pm^{5.70}_{4.66}$	$19.56\pm^{5.53}_{4.56}$	$20.70\pm^{5.30}_{4.36}$	$14.88\pm^{5.30}_{4.68}$
$B_{\overline{p}p} \times B_{\gamma\gamma} \times 10^8$	$22.79\pm^{3.91}_{3.54}$	$23.19\pm^{3.39}_{3.11}$	$21.97\pm^{2.97}_{2.79}$	$18.94\pm^{3.81}_{3.06}$
$\Gamma_{\gamma\gamma}$ (KeV)	$3.39\pm^{0.90}_{0.74}$	$3.78\pm^{0.88}_{0.72}$	$3.79\pm^{0.81}_{0.67}$	$2.35\pm^{0.67}_{0.59}$
A (pb)	$36.08\pm^{0.49}_{0.50}$	$48.19\pm^{0.54}_{0.55}$	$70.65\pm^{0.65}_{0.65}$	$116.16\pm^{0.87}_{0.88}$
B	$23.19\pm^{1.02}_{1.01}$	$24.94\pm^{0.85}_{0.84}$	$25.63\pm^{0.68}_{0.67}$	$25.40\pm^{0.54}_{0.54}$
χ^2/N_{DF}	75.89 / 75	88.53 / 75	82.33 / 75	75.73 / 75
λ	313.4	349.4	374.3	409.7
Events	678	969	1370	1912

Table 6.4: The numbers in the top table are the results to the fit using only the data. The bottom table contains the fit results when the feeddown calculation is included, and the continuum contribution to the background is neglected.

into a “known” contribution, constrained by the feeddown data, and an “unknown”, unconstrained, contribution from the continuum. There is no significant contribution from the continuum, which is consistent with the 20 ± 20 pb estimated from the VENUS measurement discussed in section 4.6.

Contrasting the first and second analyses illustrates the advantages of knowing the background shape and magnitude. When the continuum is neglected, the errors on the fit parameters are significantly reduced with the inclusion of the feeddown calculation in the fit, since the feeddown points constrain the background. However, without any *a priori* knowledge of the angular distribution or magnitude of the continuum process, the calculation of the feeddown contribution to the background

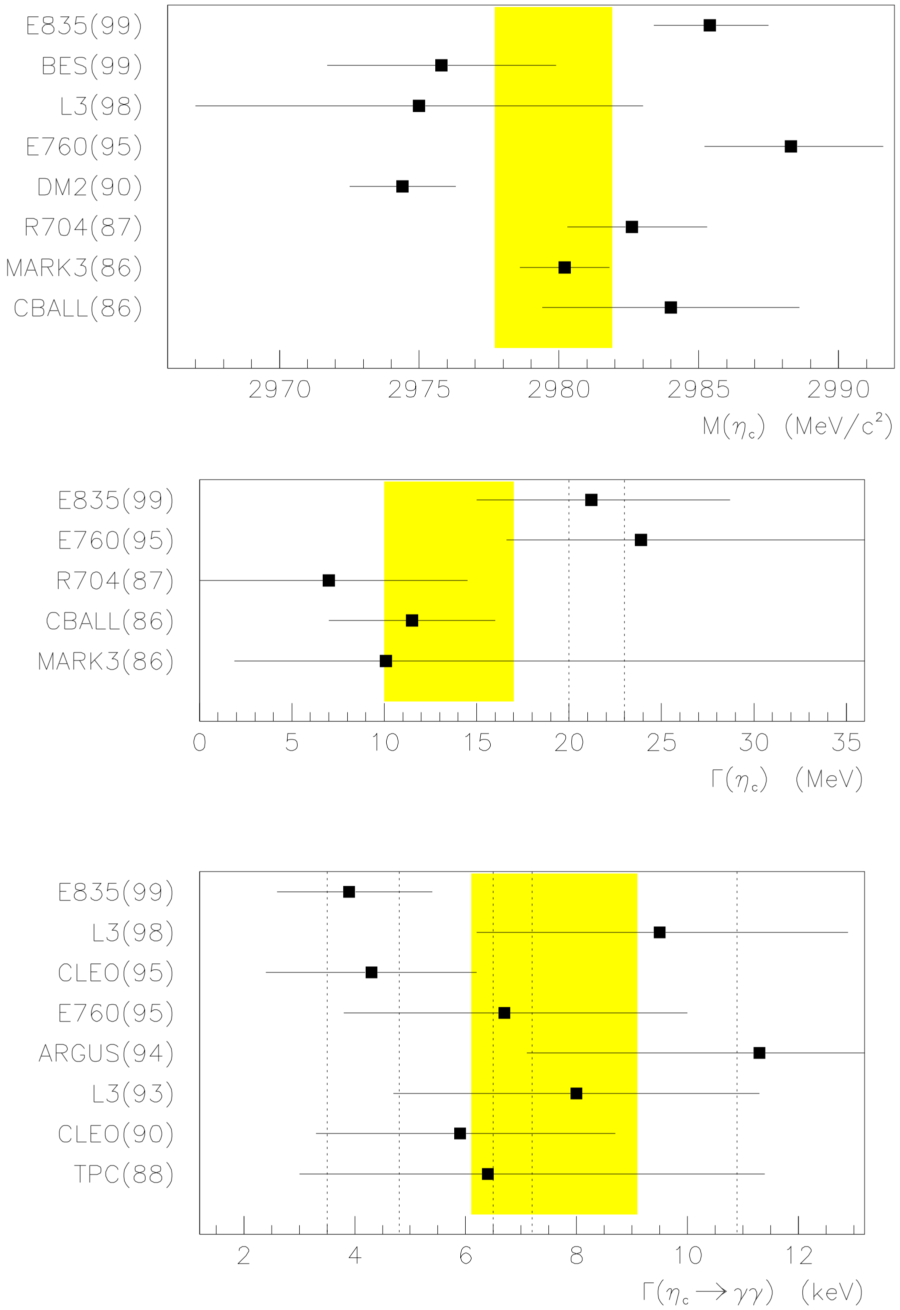

Figure 6.6: Current measurements of the η_c resonance parameters.

$\cos\theta^*$	0.15	0.20	0.25	0.30
M_{η_c} (MeV)	$2985.13\pm^{2.21}_{2.16}$	$2985.10\pm^{1.89}_{1.89}$	$2985.86\pm^{2.04}_{1.98}$	$2985.40\pm^{2.15}_{1.95}$
Γ_{η_c} (MeV)	$19.53\pm^{7.37}_{6.15}$	$18.68\pm^{7.15}_{6.20}$	$21.86\pm^{6.99}_{5.76}$	$19.68\pm^{6.91}_{6.00}$
$B_{\overline{p}p} \times B_{\gamma\gamma} \times 10^8$	$23.48\pm^{4.07}_{3.91}$	$22.92\pm^{3.62}_{3.50}$	$22.43\pm^{3.25}_{3.20}$	$20.71\pm^{3.27}_{3.21}$
$\Gamma_{\gamma\gamma}$ (keV)	$3.82\pm^{1.50}_{1.28}$	$3.57\pm^{1.40}_{1.23}$	$4.09\pm^{1.39}_{1.18}$	$3.40\pm^{1.26}_{1.11}$
A (pb)	$36.11\pm^{0.50}_{0.50}$	$48.17\pm^{0.55}_{0.55}$	$70.67\pm^{0.65}_{0.65}$	$116.32\pm^{0.88}_{0.88}$
B	$23.21\pm^{1.02}_{1.01}$	$24.93\pm^{0.85}_{0.84}$	$25.64\pm^{0.68}_{0.67}$	$25.42\pm^{0.54}_{0.54}$
C (pb)	$-1.25\pm^{2.95}_{3.01}$	$0.75\pm^{3.65}_{3.72}$	$-1.32\pm^{4.29}_{4.43}$	$-6.58\pm^{5.12}_{5.28}$
D	12.00	12.00	12.00	12.00
χ^2/N_{DF}	76.74 / 74	88.13 / 74	82.64 / 74	75.26 / 74
λ	313.2	349.3	374.2	408.0
Events	716	969	1370	2038

$\cos\theta^*$	0.15	0.20	0.25	0.30
M_{η_c} (MeV)	$2985.14\pm^{2.21}_{2.15}$	$2985.10\pm^{1.88}_{1.88}$	$2985.87\pm^{2.04}_{1.97}$	$2985.42\pm^{2.15}_{1.95}$
Γ_{η_c} (MeV)	$19.40\pm^{7.33}_{6.11}$	$18.56\pm^{7.10}_{6.18}$	$21.60\pm^{6.88}_{5.71}$	$19.44\pm^{6.81}_{5.99}$
$B_{\overline{p}p} \times B_{\gamma\gamma} \times 10^8$	$23.45\pm^{4.05}_{3.93}$	$22.88\pm^{3.62}_{3.50}$	$22.32\pm^{3.26}_{3.20}$	$20.62\pm^{3.27}_{3.22}$
$\Gamma_{\gamma\gamma}$ (keV)	$3.79\pm^{1.48}_{1.27}$	$3.54\pm^{1.38}_{1.22}$	$4.02\pm^{1.36}_{1.16}$	$3.34\pm^{1.23}_{1.10}$
A (pb)	$36.11\pm^{0.50}_{0.50}$	$48.17\pm^{0.55}_{0.55}$	$70.67\pm^{0.65}_{0.65}$	$116.32\pm^{0.88}_{0.88}$
B	$23.20\pm^{1.02}_{1.01}$	$24.93\pm^{0.85}_{0.84}$	$25.64\pm^{0.68}_{0.67}$	$25.41\pm^{0.54}_{0.54}$
C (pb)	$-1.17\pm^{2.95}_{2.99}$	$0.85\pm^{3.65}_{3.70}$	$-1.02\pm^{4.26}_{4.38}$	$-6.29\pm^{5.10}_{5.21}$
D	10.00	10.00	10.00	10.00
χ^2/N_{DF}	76.76 / 74	88.05 / 74	82.59 / 74	75.40 / 74
λ	313.2	349.3	374.2	408.1
Events	716	969	1370	2038

Table 6.5: The fit results for the η_c resonance when the continuum process is included in the fit, using equation 6.19 for two different values: $D = 12$ (upper) and $D = 10$ (lower).

can only be used as a lower limit of the total background, and does not significantly improve our measurement of the η_c resonance parameters.

These results are compared with other measurements of the η_c resonance parameters in figure 6.6. The shaded bands indicate the world average from the PDG [52]. The dotted lines on the partial width plot are the theoretical predictions listed in table 1.2. In the width plot, the dotted lines are the predictions of Gupta et al.(23 MeV)[53] and Chao et al.(20 MeV)[41].

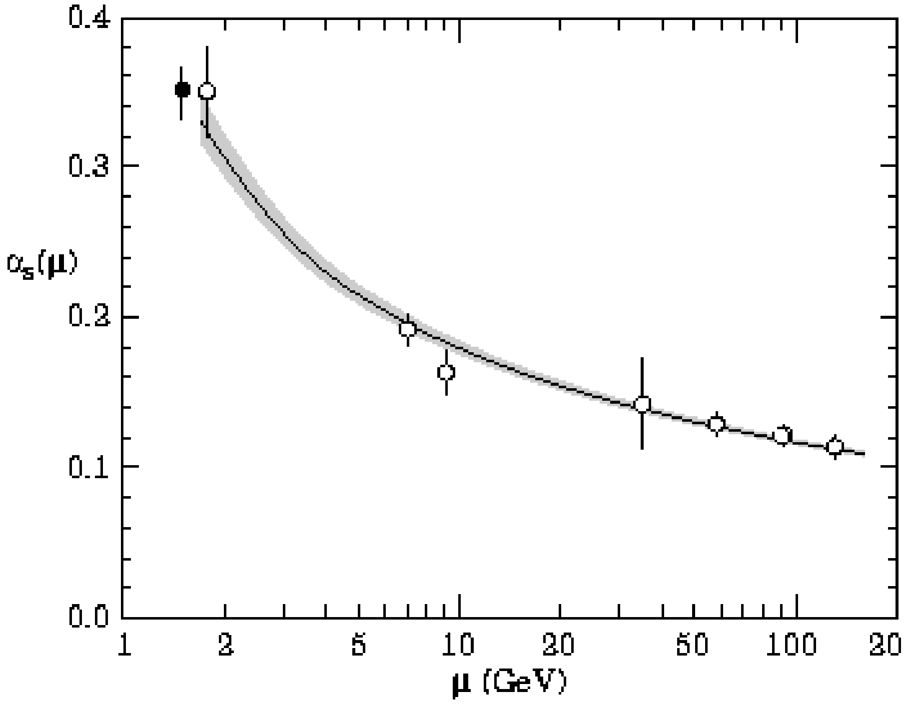

Figure 6.7: Extrapolation of α_s to the charm quark mass. The solid circle is the E835 measurement, superimposed on the figure from reference [52]. The curve is an extrapolation from the world average value of $\alpha_s(M_Z)$, the shaded regions the 1σ errors.

6.5 Calculation of α_s

Our data for $\Gamma(\eta_c \to \gamma\gamma)$ and $\Gamma(\chi_2 \to \gamma\gamma)$ provide two separate measurements of $\alpha_s(m_c)$, the strong coupling constant. Kwong et al.[62], calculate perturbative QCD formulae with first order radiative corrections for the electromagnetic and gluonic decay widths of the charmonium states. In the ratio of the two widths for a single resonance, unknown factors involving the wavefunctions and charmed quark mass cancel, and the prediction for the ratio depends only on α_s. The predictions involving E835 measured quantities are

$$\begin{aligned}
\frac{\Gamma(\eta_c \to \gamma\gamma)}{\Gamma(\eta_c \to \mathrm{gg})} &= \frac{8\alpha^2}{9\alpha_s^2}\frac{[1-\frac{3.4}{\pi}\alpha_s]}{[1+\frac{4.8}{\pi}\alpha_s]} && (6.20)\\
&\Rightarrow \alpha_s = 0.33 \pm^{0.06}_{0.03} \\
\frac{\Gamma(\chi_2 \to \gamma\gamma)}{\Gamma(\chi_2 \to \mathrm{gg})} &= \frac{8\alpha^2}{9\alpha_s^2}\frac{[1-\frac{16}{3\pi}\alpha_s]}{[1-\frac{2.2}{\pi}\alpha_s]} && (6.21)\\
&\Rightarrow \alpha_s = 0.39 \pm 0.02
\end{aligned}$$

where the approximations

$$\begin{aligned}
\frac{\Gamma(\eta_c \to \gamma\gamma)}{\Gamma(\eta_c \to \mathrm{gg})} &\approx B(\eta_c \to \gamma\gamma) \\
\frac{\Gamma(\chi_2 \to \gamma\gamma)}{\Gamma(\chi_2 \to gg)} &\approx \frac{B(\chi_2 \to \gamma\gamma)}{1 - B(\chi_2 \to \psi\gamma)}
\end{aligned}$$

are used to calculate α_s.

The combined result, 0.35 ± 0.02, is shown in figure 6.7, superimposed on the PDG compilation of α_s measurements. This result is compatible with the measured values in E760 of 0.36 ± 0.04[15] from $\chi_2 \to \gamma\gamma$ and $0.29\pm^{0.05}_{0.04}$[16] from $\eta_c \to \gamma\gamma$.

6.6 η_c' results

E835 took data in the center-of-momentum energy range 3575 MeV to 3665 MeV, searching for the η_c' in the $\gamma\gamma$ and $J/\psi\gamma$ channels. No signal is present in either channel. Instead, an upper limit is reported for the product of the branching ratios, $B(\eta_c' \to \overline{p}p) \times B(\eta_c' \to \gamma\gamma)$.

6.6.1 Background Determination

For the η_c' analysis, the data are separated into a background sample and a resonance sample. The background sample consists of the data taken at the ${}^1P_1$ ($\sqrt{s} = 3526$ MeV) and the ψ'($\sqrt{s} = 3686$ MeV). The background data are fit to the function

$$\sigma_{bkgd} = A\left(\frac{3556.2\ MeV}{\sqrt{s}}\right)^B \tag{6.22}$$

The results of the background fit are in table 6.6. The combined data sample is shown in figure 6.8, with the the background curve that results from fitting the background sample alone.

A (pb)	17.9 ± 0.7
B	6.2 ± 2.7
cov(A,B)	-0.47

Table 6.6: Results of the maximum likelihood fit to the data used to determine the background.

6.6.2 Determination of Upper Limits

For the E835 data at the η_c', a likelihood function is constructed as described in section 6.1. The values of the mass and width of the resonance, as well as the background cross section, are fixed in the likelihood function. The value of σ_{peak} that

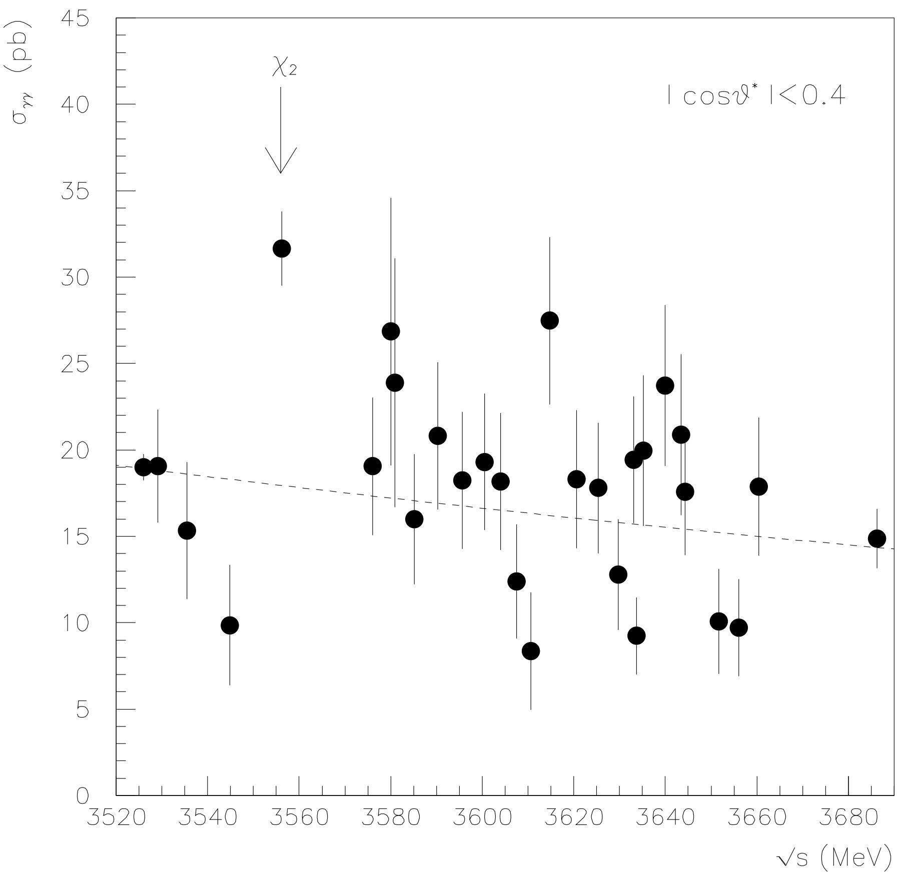

Figure 6.8: The $\gamma\gamma$ signal in the $\sqrt{s}$ region between the ${}^1P_1$ and the ψ'. The dashed line is the background level determined from the points at the ${}^1P_1$ ($\sqrt{s} = 3526$ MeV) and the ψ' ($\sqrt{s} = 3686$ MeV). The excess at $\sqrt{s} = 3556.2$ MeV is the $\gamma\gamma$ decay of the χ_2 resonance.

best fits the data is that which maximizes the likelihood function. This maximization is repeated for different values of the resonance mass and width, covering a range $3576 \leq M_R \leq 3662$ MeV in 0.5 MeV steps and $\Gamma = 5, 10, 15$ MeV, giving a set of values $\{\sigma_{peak,best}(M_R, \Gamma)\}$ The fact that the background is fixed in the fit implies that it is known exactly. In reality, there are errors in the background parameters and this uncertainty must be included in the final results. These errors are temporarily ignored during the discussion of how the upper limits are determined, and reintroduced in the next section.

There is controversy in the literature about how to translate the fit results into confidence intervals. The intervals presented in this section and the following one have been calculated with the unified approach, developed by Feldman and Cousins[48]. A summary of their method, and a comparison of it with other possible methods is the focus of appendix G. Feldman and Cousins present a new method for constructing frequentist confidence intervals. The method differs from earlier frequentist ones in special cases for which there is a physical boundary on the parameter. In these cases, the intervals calculated with the unified method never include the non-physical region, while having the proper coverage.

To construct frequentist confidence intervals by any method, the distribution $\mathrm{P}(\mathrm{x}|\mu)$ is needed. $\mathrm{P}(\mathrm{x}|\mu)$ is the probability of obtaining a measurement x for a true value of μ. Often $\mathrm{P}(\mathrm{x}|\mu)$ is calculated with a series of Monte Carlo experiments. For the special case for which $\mathrm{P}(\mathrm{x}|\mu)$ is Gaussian, with non-negative μ, Feldman and Cousins have tabulated these confidence intervals near the physical boundary $\mu = 0$ (Table X in reference [48]). It is convenient to use this table to translate the η_c' fit results into upper limits. This is possible if $\mathrm{P}(\sigma_{peak,best} \mid \sigma_{peak,true})$, the probability of obtaining the best estimate $\sigma_{peak,best}(M_R, \Gamma)$ if the actual value is $\sigma_{peak,true}$, is Gaussian with variance independent of $\sigma_{peak,true}$.

In the case of the E835 data at the η_c', with the mass, width, and background all "known", the only free parameter is σ_{peak}. σ_{peak} is estimated with a linear least squares fit The likelihood function is denoted $\mathrm{L}(\sigma_{peak} \mid \sigma_i, \mathrm{V}_i; M_R, \Gamma, \sigma_{bkgd})$ to emphasize that the measured value of σ_{peak} depends upon the individual measurements σ_i, each with variance V_i, as well as the values of the fixed parameters $M_R, \Gamma,$ and σ_{bkgd}. The quantity measured is σ_i, which is fit to $\sigma_{bkgd}(s_i) + \sigma_{peak}W(s_i)$, where the function W is the remainder of the Breit-Wigner resonance expression, equation 2.1, after factoring out the peak cross section.

The log of the likelihood function is written

$$\chi^2 = -2\ln L + constant = \sum_{i=1}^{N} \frac{\left[\sigma_i - (\sigma_{bkgd}(s_i) + \sigma_{peak}W(s_i))\right]^2}{V_i} \tag{6.23}$$

and the estimate $\sigma_{peak,best}(M_R, \Gamma)$ is the value which maximizes L. An estimator obtained by a linear least squares fit is guaranteed to be efficient and normally distributed around the true value. Furthermore, the variance of this distribution, V_{peak}, is given by

$$\frac{1}{V_{peak}} \quad = \quad - \left.\frac{d^2(lnL)}{d\sigma_{peak}^2}\right|_{\sigma_{peak}=\sigma_{peak,best}} = \sum_i \frac{W(s_i)^2}{V_i} \tag{6.24}$$

and is independent of the true value of σ_{peak}. Thus, the tables in Feldman and Cousins can be used to construct the confidence intervals since the shape of $\mathrm{P}(\mathrm{x}|\mu)$ is known. To obtain the variance of the measurement, the individual points are combined by weighting each with its proximity to the resonance peak, supporting the intuitive notion that data far away from the resonance does not improve the estimate of the resonance parameters once the background is known.

The probability distribution is also shown to be Gaussian distributed, with a variance independent of σ_{peak}, using a series of Monte Carlo experiments, generated with the E835 running conditions (luminosity, analysis efficiency, etc.). Two values

M_R (MeV)	Γ_R (MeV)	σ_{peak} (pb)	μ_{lik}	σ_μ	$\sqrt{V_\sigma}$	$\sigma_{\sqrt{V}}$
3649.0	5.0	1.0	1.0	18.0	18.1	1.5
3649.0	5.0	10.0	10.0	18.6	18.8	1.5
3649.0	5.0	30.0	30.0	20.2	20.2	1.4
3633.5	5.0	1.0	1.0	5.8	5.8	0.3
3633.5	5.0	10.0	10.0	6.3	6.3	0.3
3633.5	5.0	30.0	30.0	7.2	7.2	0.3
3633.5	10.0	10.0	10.0	5.5	5.5	0.3
3633.5	15.0	10.0	10.0	4.9	4.9	0.2

Table 6.7: A study of the probability distributions using Monte Carlo generated experiments.

of M_R are chosen to examine the probability distribution, the ones with the least and most amount of data. The values $\Gamma = 5, 10, 15$ MeV, and $\sigma_{peak,true} = 1, 10, 30$ pb are considered for each M_R, and 100,000 MC experiments are generated for each. A likelihood fit is performed on the results of each Monte Carlo experiment, and the distributions of $\sigma_{peak,best} (= \mu_{lik})$ and $\sigma_{\sigma_{peak,best}}$ examined. The results are in table 6.7, and it can be seen that the *r.m.s.* of likelihood function, $\sqrt{V_{peak}}$, is a reasonable estimate of the width of the probability distribution, $\sigma_{\sigma peak,best}$. Example distributions are shown in figure 6.9.

6.6.3 Incorporating the Error on the Background

Because the effective background cross section was fixed in the likelihood fits for the η_c' resonance, the value of V_{peak} from the likelihood function, and hence the width of the distribution $\mathrm{P}(\sigma_{peak,best} \mid \sigma_{peak,true})$, does not include the uncertainty in the background level. The confidence intervals are constructed with a modified value of V_{peak} that includes the error on the background determination.

The likelihood function separates the observed signal, $\sigma = \frac{N}{\epsilon L}$, into the sum of two pieces, $\sigma = \sigma_{bkgd} + a\sigma_{res}$. The factor $a = 0.4$ is the geometrical acceptance

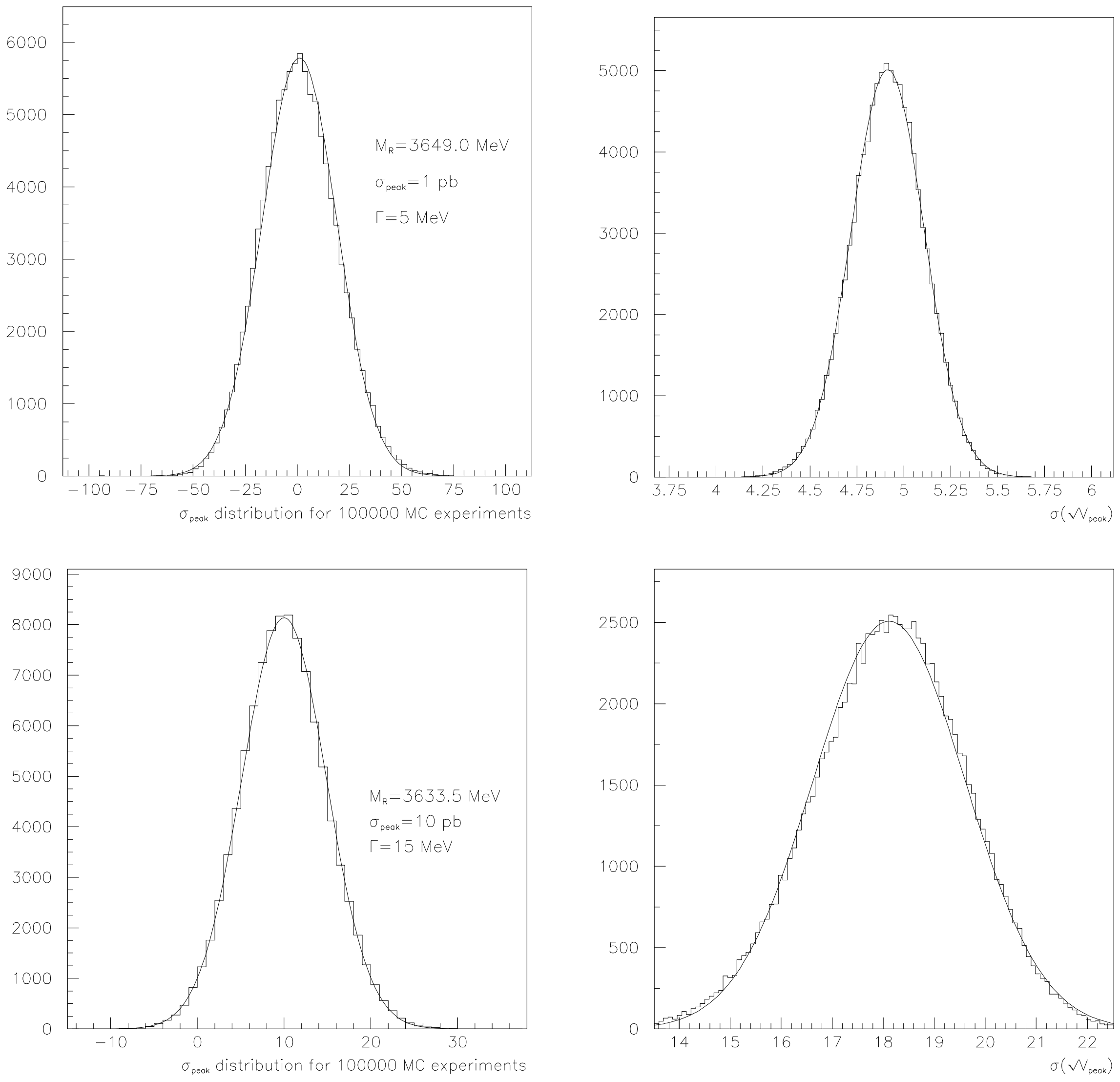

Figure 6.9: The distribution of $\sigma_{peak,best}$ (left) and the r.m.s. of the likelihood function (right) for two different sets of Monte Carlo experiments.

of the $|\cos\theta^*|$ analysis cut. σ_{bkgd} is defined in the likelihood function without the acceptance term, so it must be explicitly (and awkwardly) included here. The details of the likelihood function are in section 6.1. The error on σ depends upon the observed number of events near the hypothetical value for M_R. If σ_{peak} is the only free resonance parameter in the fit, then we find the error on σ_{peak}, $\sqrt{V'_{peak}}$, from

$$a^2 V'_{peak} = V + V_{bkgd} \tag{6.25}$$

where $\sqrt{V}$ and $\sqrt{V_{bkgd}}$ are the uncertainties in σ and σ_{bkgd} respectively. σ_{bkgd} is calculated with a linear least squares fit, whose results are in table 6.6.

The variance on $B_{in}B_{out}$ is obtained from equation 6.3,

$$V_{BB} = \left(\frac{{M_R}^2 - 4m_p^2}{(2J+1)4\pi\hbar^2}\right)^2 \times \left(\frac{1}{a}\right)^2 \times \left(V + V_{bkgd}\right) \tag{6.26}$$

The contribution of the background uncertainty to the error in $B_{in}B_{out}$ as a function of s is shown in figure 6.10 with the dashed line. V is estimated with the value of V_{peak} obtained from the likelihood function maximization with the background parameters fixed. These values are shown with the symbols in Figure 6.10. The minimum in the error contribution from the data is at $\sqrt{s} = 3633$ MeV, where the most integrated luminosity was accumulated (over 4.5 pb). The maxima of the error contribution from the data occur at mass values at the center of large gaps (in $\sqrt{s}$) between data-points.

The construction of V'_{peak} in equation 6.25 neglects any correlations in the variables σ_{peak} and σ_{bkgd}. This method was checked with a second likelihood fit in which the background parameters are free. The variables σ_{peak} and σ_{bkgd} in this fit are only slightly correlated($\rho \sim 0.1$), and the variance of σ_{peak} calculated in the fit agrees with the variance calculated from equation 6.25. The values of $\sigma_{peak,best}$ from the two fits are converted to values for $B_{in}B_{out}$ and plotted in figure 6.11 as the solid (background

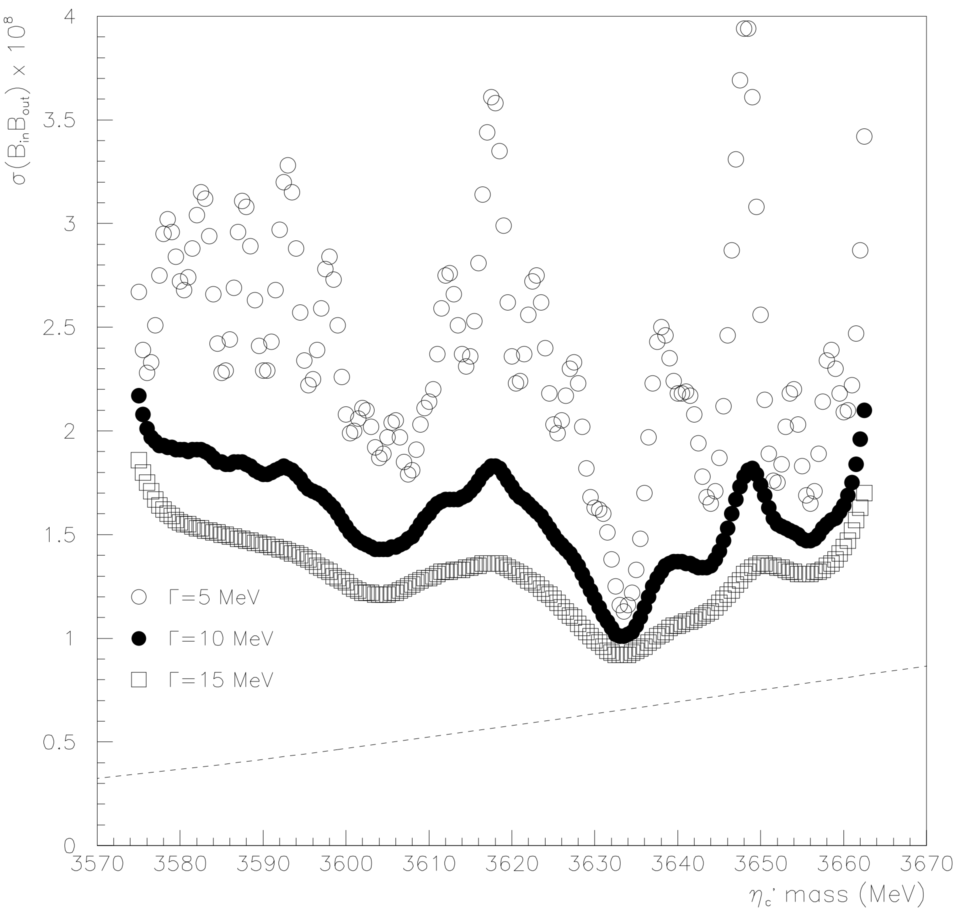

Figure 6.10: The contribution to the error on $B_{in}B_{out}$ from the error in the background determination is shown as the dashed line. The contribution from the data is shown with the symbols.

fixed) and empty cicles (background free). The bands represent $\pm\sqrt{V_{peak}}$; the lighter band is associated with the open circles. The upper plot is $\Gamma = 5$ MeV and the lower one is $\Gamma = 15$ MeV. The largest difference between the bands is where the uncertainty in the in the background is greatest. The global upper limit, chosen as the maximum upper limit in the mass range considered, is the same for the two methods. The first method, using a fixed background in the fit and the background variance added in quadrature is chosen, since it gives more conservative upper limit in the case of a low background fluctuation (for example at $\sqrt{s} = 3650$ MeV).

The values of V'_{peak} and $\sigma_{peak,best}$ are used to construct confidence intervals as described in section 6.6.2. The 90% confidence intervals are reported in terms of $B(\eta'_c \to \overline{p}p)B(\eta'_c \to \gamma\gamma)$ in figure 6.12 for three different values of the η'_c width. The global upper limits are

$$B(\eta'_c \to \overline{p}p) \times B(\eta'_c \to \gamma\gamma) < 12 \times 10^{-8} \quad \text{for} \quad \Gamma_{\eta'_c} = 5 \text{ MeV}$$
$$B(\eta'_c \to \overline{p}p) \times B(\eta'_c \to \gamma\gamma) < 6 \times 10^{-8} \quad \text{for} \quad \Gamma_{\eta'_c} = 10 \text{ MeV}$$
$$B(\eta'_c \to \overline{p}p) \times B(\eta'_c \to \gamma\gamma) < 6 \times 10^{-8} \quad \text{for} \quad \Gamma_{\eta'_c} = 15 \text{ MeV}.$$

These upper limits can be compared to the value measured for the η_c,
$B(\eta'_c \to \overline{p}p) \times B(\eta'_c \to \gamma\gamma) = (21.9\pm^{7.0}_{5.8}) \times 10^{-8}$.

6.7 χ_0 results

The χ_0 mass corresponds to a beam momentum difficult to obtain with the Antiproton Accumulator. As a result, E835 accumulated only 3.5 pb^{-1} of integrated luminosity at the χ_0. The measurement is complicated by small branching ratios and a background shape is changing rapidly near the peak. Figures 6.13 and 6.14 show the $\pi^0\pi^0$ and $\pi^0\gamma$ cross sections for several acceptance cuts. The "elbow" observed

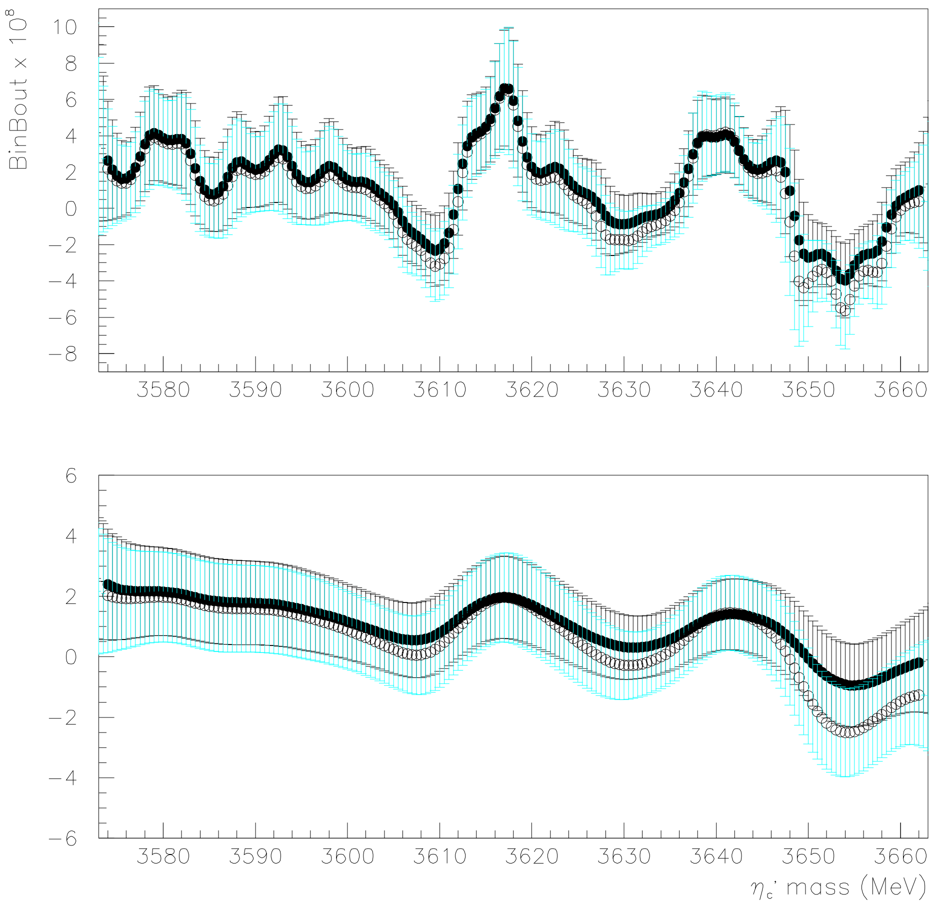

Figure 6.11: A comparison between two estimates of $B_{in}B_{out}$.

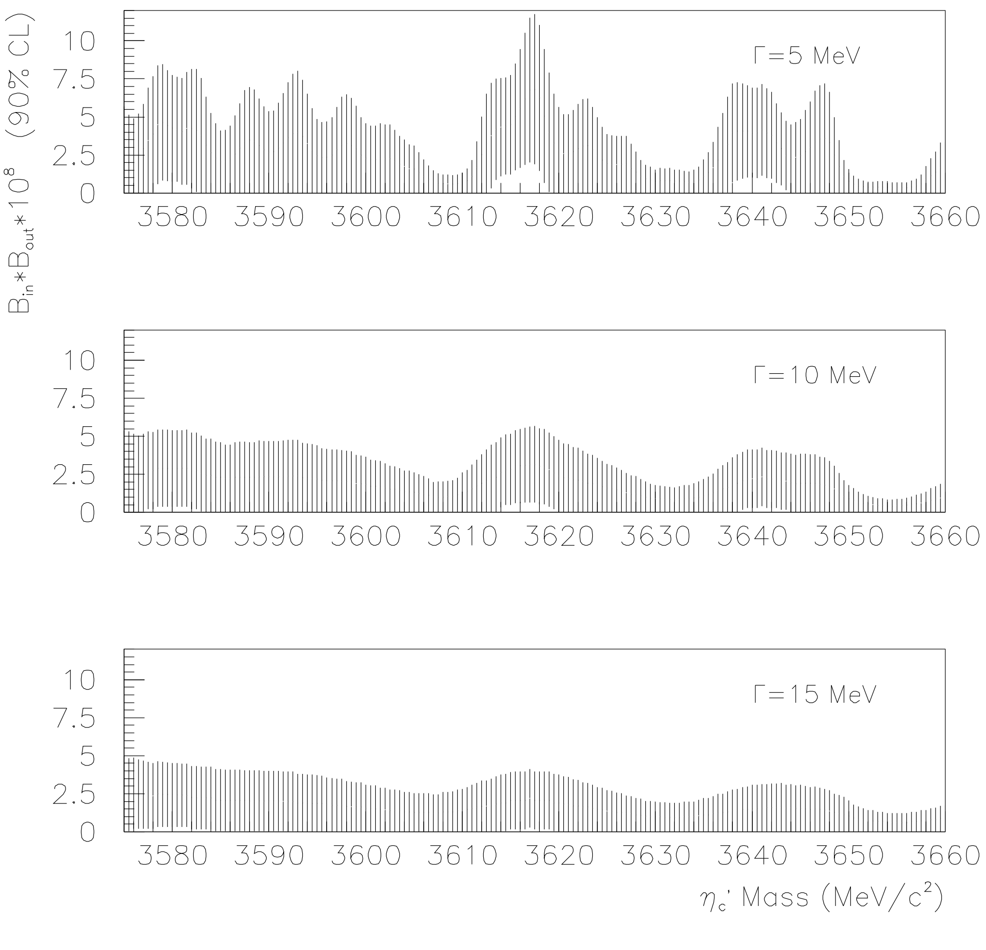

Figure 6.12: The 90% confidence region obtained using the E835 data and the statistical methods of Feldman and Cousins [48]. Three different values for the total width of the η_c' are considered.

near $\sqrt{s} = 3.2$ GeV in the $\pi^0\pi^0$ cross section is a result of the changing angular distribution, which can be seen in figure 4.5. A similar elbow at $\sqrt{s} \sim 3.4$ GeV is suggested in the $\pi^0\gamma$ data. Away from this region, $3.1 < \sqrt{s} < 3.5$ GeV, the parameterization $\sigma_{bkgd} = A \times (\frac{\sqrt{s_0}}{\sqrt{s}})^B$ fits the data well, as seen in the analysis of the η_c and χ_2 resonances, but with quite different values for the exponent B. For this reason, the simple parameterization of the background in equation 6.4 is not adequate for the region considered in the χ_0 analysis, 3200 MeV $< \sqrt{s} <$ 3500 MeV.

Figure 6.15 shows the data and the feeddown calculation for a large $\sqrt{s}$ range that includes the χ_0. Two curves are drawn on the plot. The first curve (a) is the best fit to the resonance plus the simple background parameterization of equation 6.4. A modified parameterization of the background

$$\sigma_{bkgd} = A \times e^{-0.001*B*(\sqrt{s}-3200)} + C \tag{6.27}$$

gives the second curve (b) which better accommodates the background. The fit results are shown in table 6.8. The mass and width of the χ_0 are fixed to the values $M_{\chi_0} = 3417.7 \pm 1.9$ MeV and $\Gamma_{\chi_0} = 16.6 \pm^{5.2}_{3.7}$ MeV. These are obtained from an analysis of the $J/\psi + X$ decay mode[9], along with the branching ratio $B(\chi_0 \to \overline{p}p) = (4.8 \pm^{0.9}_{0.8} \pm^{2.1}_{1.1}) \times 10^{-4}$.

With the systematic errors included, the E835 measurement is $\Gamma(\chi_0 \to \gamma\gamma) = 1.2 \pm 0.7 \pm 0.3 \pm^{0.5}_{0.4}$ keV. The first systematic error comes from the uncertainty in the fixed width of the resonance, and is estimated by the change in the partial width as the resonance width is varied within its errors. The second systematic error comes from the uncertainty in the $\overline{p}p$ branching ratio. Using the same technique as the η_c', the shape of the likelihood function is used to estimate the variance of the probability distribution The statistical and systematic errors are added in quadrature to give the combined variance of $\sqrt{V} = 0.9$ keV, and the intervals $[0.3, 2.1]$ keV (68% CL) and

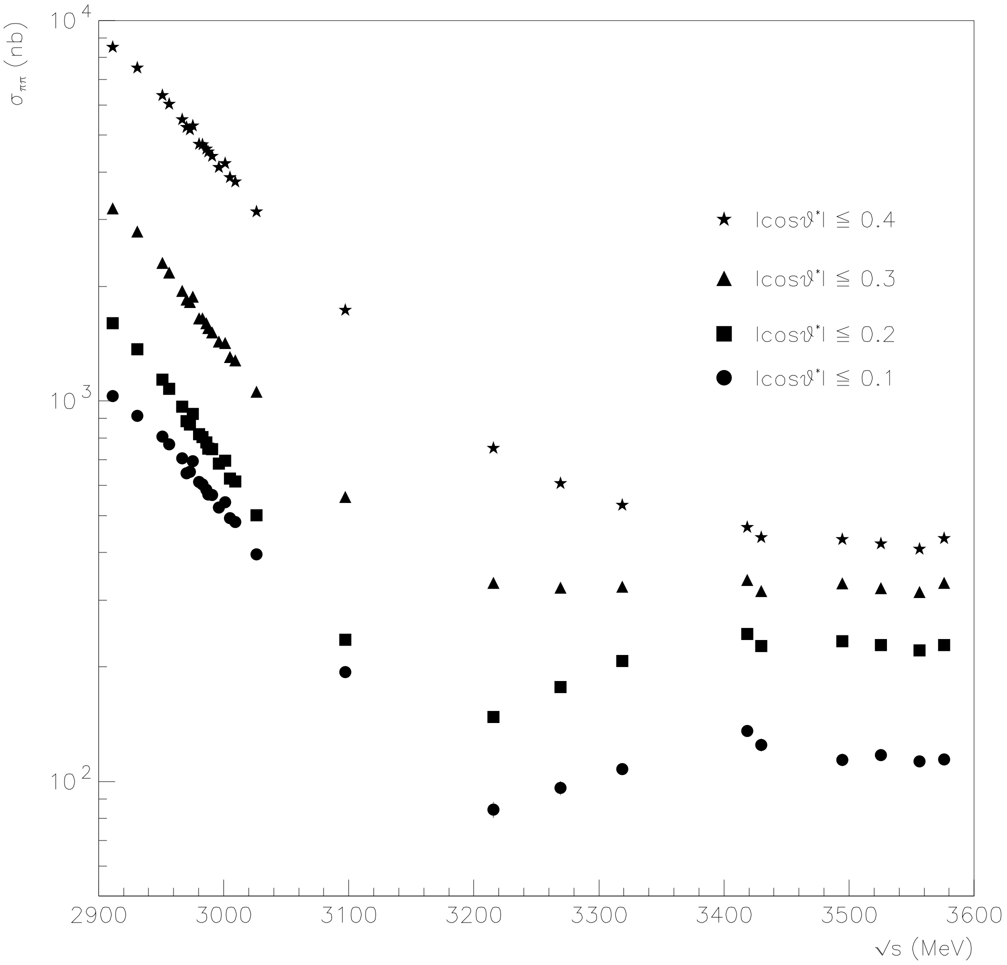

Figure 6.13: The $\pi^0\pi^0$ cross section over a large range of $\sqrt{s}$ for increasing acceptance.

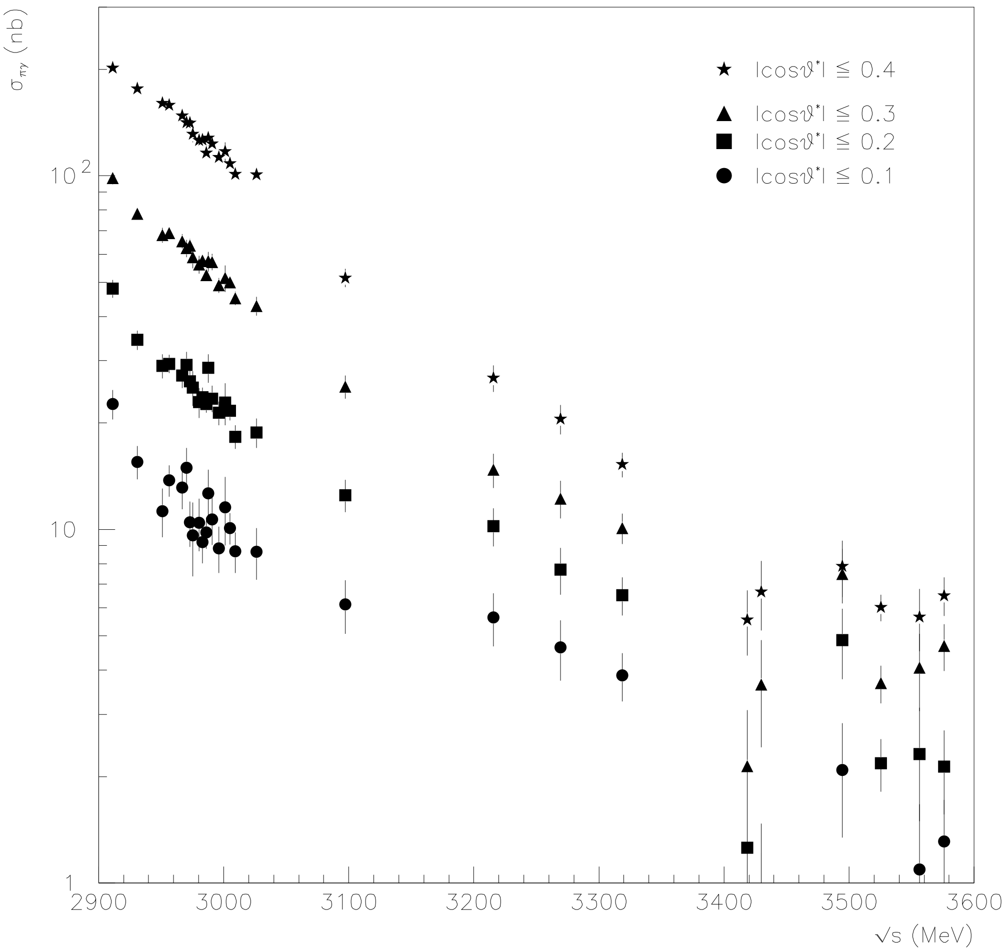

Figure 6.14: The $\pi^0\gamma$ cross section over a large range of $\sqrt{s}$ for increasing acceptance.

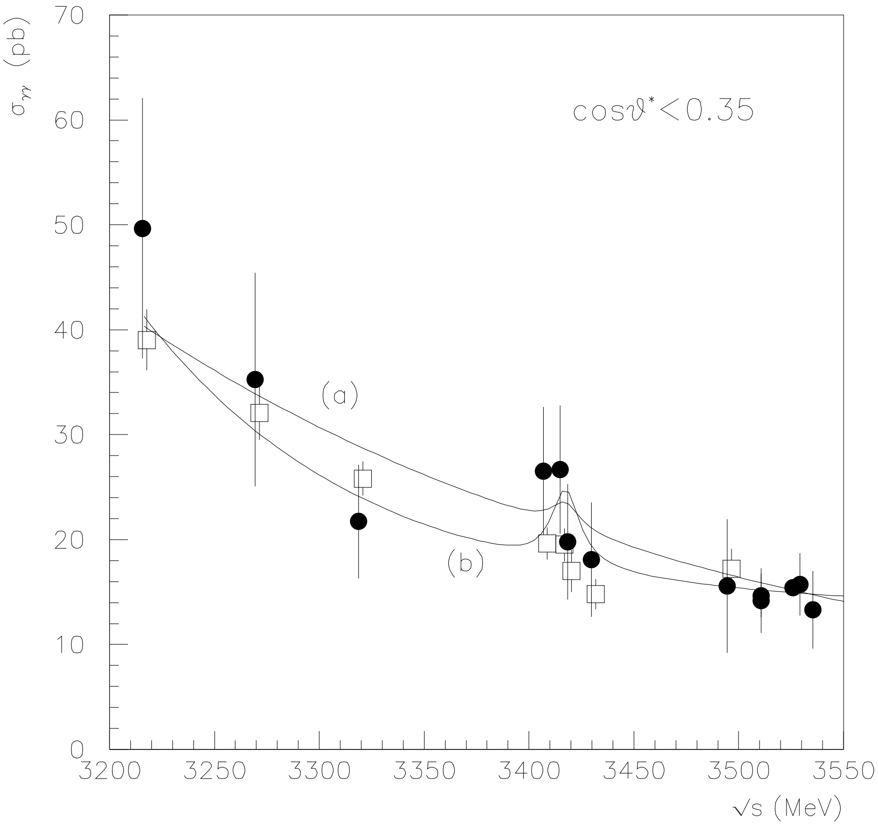

Figure 6.15: The data (circles) and feeddown calculation (squares) at the χ_0 for the acceptance cut $|\cos\theta^*| \leq 0.35$. The curve labeled (a) is a fit to the data using the background parameterization of equation 6.4. Curve (b) is the modified background parametization of equation 6.27.

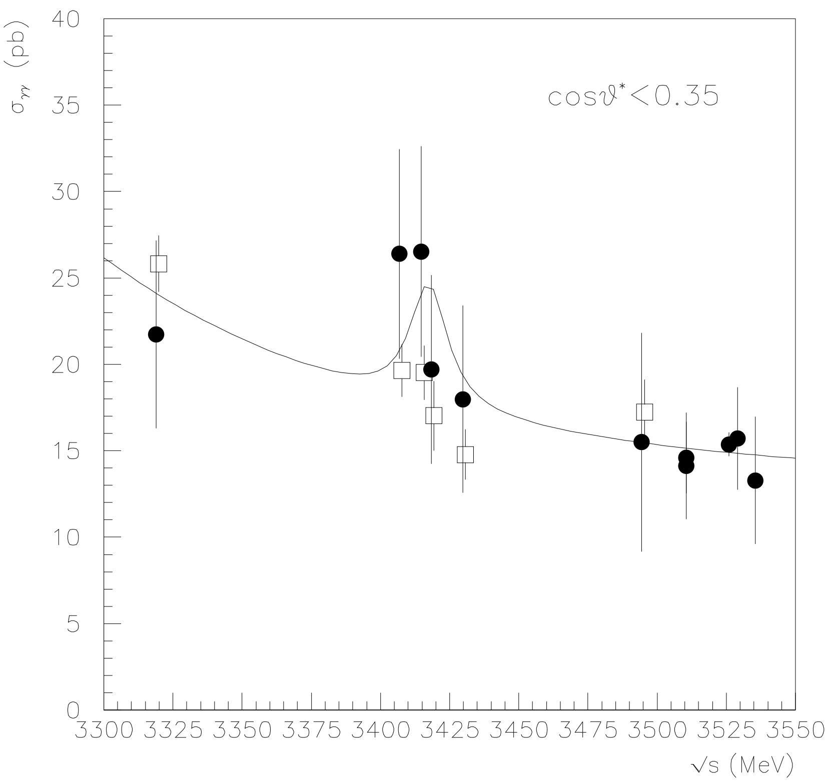

Figure 6.16: The data (circles) and feeddown calculation (squares) at the χ_0 for the acceptance cut $|\cos\theta^*| \leq 0.35$. The data are binned in 3 MeV bins.

$\cos\theta^*$	0.30	0.35	0.40
$B_{\overline{p}p} \times B_{\gamma\gamma} \times 10^8$	$30.42 \pm^{20.85}_{18.77}$	$30.94 \pm^{19.48}_{17.67}$	$23.71 \pm^{18.42}_{16.85}$
$\Gamma_{\gamma\gamma}$ (keV)	$1.15 \pm^{0.79}_{0.71}$	$1.17 \pm^{0.74}_{0.67}$	$0.90 \pm^{0.70}_{0.64}$
A (pb)	$20.66 \pm^{2.54}_{2.45}$	$32.59 \pm^{3.09}_{2.97}$	$49.78 \pm^{3.92}_{3.78}$
B	$8.81 \pm^{2.21}_{2.05}$	$9.30 \pm^{1.70}_{1.60}$	$9.58 \pm^{1.37}_{1.30}$
C (pb)	$11.21 \pm^{0.96}_{1.37}$	$13.28 \pm^{1.06}_{1.36}$	$16.10 \pm^{1.21}_{1.46}$
χ^2/N_{DF}	74.18 / 42	66.68 / 42	61.06 / 42
λ	2.8	3.3	2.1
Events	52	62	74

Table 6.8: Results of the maximum likelihood fit at the χ_0, for the modified background parameterization of equation 6.27. $\Gamma_{\gamma\gamma}$ has been calculated using the value $BR(\chi_0 \to \overline{p}p) = 4.8 \pm^{0.9}_{0.8} \pm^{2.1}_{1.1} \times 10^{-4}$. [9]

$[0.00, 2.7]$ keV (95% CL) are obtained using table X in reference [48]. This result is compared with other measurements of the two-photon partial width of the χ_0 in figure 6.17. The only value quoted in the PDG is that of Crystal Ball. The dashed lines are the theoretical predictions listed in table 1.2.

6.8 Conclusions

E835 has measured the resonance parameters of the η_c resonance. Our mass is consistent with other measurements, which vary substantially. Our width is larger than previous measurements, but consistent within errors. The partial width to two photons has been measured for both the η_c and the χ_2. Our η_c results are consistent with the measurements from e^+e^- colliders, however our χ_2 partial width is somewhat lower than other measurements, but consistent with theoretical predictions. Upper limits are placed on the product of branching ratios $B(\eta_c' \to \overline{p}p) \times B(\eta_c' \to \gamma\gamma)$ over a large energy range. The limits are surprisingly lower than the same product for the η_c resonance. A hint of the decay $\chi_0 \to \gamma\gamma$ is seen, and E835 plans to take more data at the χ_0 during the next run.

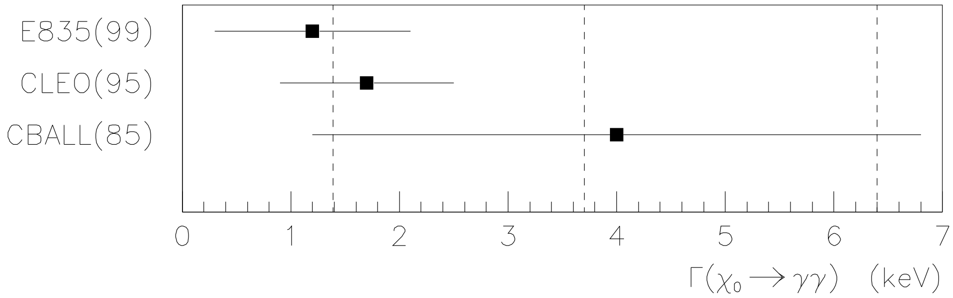

Figure 6.17: Current measurements of the two-photon partial width of the χ_0.

CBALL(85) [63] $*$	$\psi' \to \chi_0\gamma, \chi_0 \to \gamma\gamma$
MARK3(86) [29]	$J/\psi \to \eta_c\gamma, \eta_c \to$ hadrons
CBALL(86) [49]	$e^+e^- \to J/\psi \to \eta_c\gamma, \eta_c \to$ hadrons $e^+e^- \to \psi' \to \eta_c\gamma, \eta_c \to$ hadrons
R704(87) [21]	$\overline{p}p \to \eta_c \to \gamma\gamma$ $\overline{p}p \to \chi_2 \to \gamma\gamma$
TPC(88) [5]	$\gamma\gamma \to \eta_c \to$ hadrons
DM2(91) [33]	$e^+e^- \to J/\psi \to \eta_c\gamma, \eta_c \to$ hadrons
TPC(93) [31]	$\gamma\gamma \to \chi_2 \to J/\psi\gamma, J/\psi \to l^+l^-$
E760(93) [15]	$\overline{p}p \to \chi_2 \to \gamma\gamma$
ARGUS(94) [6]	$\gamma\gamma \to \eta_c \to$ hadrons
CLEO(94) [77]	$\gamma\gamma \to \chi_2 \to J/\psi\gamma, J/\psi \to l^+l^-$
E760(95) [16]	$\overline{p}p \to \eta_c \to \gamma\gamma$
CLEO(95) [75] $*$	$\gamma\gamma \to \chi_2 \to$ hadrons $\gamma\gamma \to \chi_0 \to$ hadrons $\gamma\gamma \to \eta_c \to$ hadrons
L3(98) [1]	$\gamma\gamma \to \eta_c \to$ hadrons
OPAL(98) [3]	$\gamma\gamma \to \chi_2 \to J/\psi\gamma, J/\psi \to l^+l^-$
BES(99) [25]	$\psi' \to \gamma\eta_c, \eta_c \to$ hadrons
L3(99) [2]	$\gamma\gamma \to \chi_2 \to J/\psi\gamma, J/\psi \to l^+l^-$

Table 6.9: Table of other measurements compared to those of E835 reported. $*$ indicates that result has not yet been published in a journal.

Appendix A

Data Summary Table

The table below summarizes the data taken take in E835. The number of $\gamma\gamma$ candidates is given after applying the analysis cuts detailed in chapter 5. Where the feeddown has been calculated, the number of expected feeddown events is included, along with the statistical error.

η_c data ($\lvert\cos\theta^*\rvert < 0.25$)						
$\sqrt{s}$ (MeV)	stack	$\int Ldt$ (pb^{-1})	inst. lum. ($10^{31}cm^{-2}s^{-1}$)	$N_{\gamma\gamma}$	N_{feed}	ϵ_{total}
2911.36	46.1	0.515	0.84	49	59.8 ± 2.2	0.768
2912.26	42.2	0.190	0.50	25	22.6 ± 1.4	0.795
2930.11	28.1	0.318	0.67	19	30.4 ± 1.7	0.779
2930.48	23.2	0.372	0.75	38	38.6 ± 1.9	0.790
2930.62	29.1	0.224	0.57	14	21.4 ± 1.3	0.782
2930.75	47.1	0.768	0.93	67	67.7 ± 2.4	0.768
2950.18	12.3	0.262	0.93	20	19.7 ± 1.3	0.776
2950.71	27.1	0.406	0.75	36	27.8 ± 1.6	0.768
continued on next page						

$\sqrt{s}$ (MeV)	stack	$\int Ldt$ (pb^{-1})	inst. lum. ($10^{31}\mathrm{cm}^{-2}\mathrm{s}^{-1}$)	$N_{\gamma\gamma}$	N_{feed}	ϵ_{total}
continued from previous page						
2950.77	35.1	0.373	0.60	29	29.0 ± 1.6	0.788
2951.13	39.3	0.605	1.16	49	44.5 ± 2.0	0.747
2956.26	44.1	0.398	0.67	29	30.3 ± 1.6	0.783
2956.29	45.1	0.979	0.96	79	70.8 ± 2.5	0.764
2966.87	40.8	0.588	0.93	47	38.8 ± 1.8	0.765
2966.94	15.4	0.286	0.81	28	20.3 ± 1.3	0.782
2970.14	26.1	0.402	0.74	29	27.6 ± 1.5	0.796
2973.14	41.1	0.668	0.90	50	41.1 ± 1.8	0.763
2973.97	24.1	0.620	0.83	53	37.3 ± 1.8	0.765
2975.39	32.1	0.345	0.68	23	22.2 ± 1.4	0.778
2980.48	18.1	0.441	0.77	37	25.8 ± 1.4	0.789
2980.51	17.4	0.250	0.79	22	14.0 ± 1.1	0.788
2983.05	49.1	1.004	0.91	99	58.8 ± 2.1	0.768
2985.99	31.1	0.468	0.79	45	25.5 ± 1.4	0.776
2986.09	48.1	1.410	1.13	136	73.4 ± 2.4	0.753
2987.58	16.1	0.341	0.84	26	21.1 ± 1.3	0.785
2987.75	9.4	0.250	0.72	18	14.3 ± 1.0	0.797
2988.00	37.1	0.371	0.71	36	18.5 ± 1.2	0.780
2990.66	34.1	0.499	0.76	45	28.0 ± 1.5	0.780
2996.15	25.1	0.743	1.04	59	39.1 ± 1.7	0.765
3000.86	33.1	0.347	0.77	22	14.0 ± 1.0	0.776
3001.31	36.1	0.210	0.72	8	11.1 ± 0.9	0.778
3004.92	43.1	1.169	0.98	72	56.6 ± 2.1	0.769
3009.09	30.1	0.929	0.88	39	42.9 ± 1.9	0.766
3025.17	13.3	0.104	0.91	4	3.6 ± 0.5	0.784
3026.10	14.2	0.489	0.99	18	21.6 ± 1.3	0.786
3096.68	60.3	0.152	0.43	2	3.3 ± 0.4	0.681
3097.07	5.3	0.168	0.41	7	4.4 ± 0.5	0.676
3097.14	7.4	0.285	0.57	2	5.8 ± 0.6	0.678
3097.26	19.3	0.492	0.79	12	9.8 ± 0.7	0.670
3097.30	42.1	0.328	1.03	10	6.4 ± 0.6	0.648
3100.61	73.1	0.143	0.55	4	2.7 ± 0.4	0.676
χ_0 data ($\lvert\cos\theta^*\rvert < 0.35$)						
continued on next page						

$\sqrt{s}$ (MeV)	stack	$\int Ldt$ (pb^{-1})	inst. lum. ($10^{31}cm^{-2}s^{-1}$)	$N_{\gamma\gamma}$	N_{feed}	ϵ_{total}
continued from previous page						
3215.71	66.1	0.420	1.27	16	12.7 ± 0.9	0.772
3269.43	79.7	0.412	0.56	12	10.9 ± 0.9	0.827
3318.82	76.1	0.951	1.36	16	19.0 ± 1.2	0.774
3406.76	72.1	0.926	1.33	19	14.1 ± 1.1	0.777
3414.78	70.1	0.585	1.81	13	7.9 ± 0.9	0.736
3414.82	69.2	0.353	0.85	6	5.4 ± 0.7	0.809
3418.14	60.2	0.146	0.92	5	2.6 ± 0.4	0.810
3418.46	68.2	0.692	1.36	8	6.4 ± 0.8	0.783
3429.53	77.2	0.349	0.79	5	4.8 ± 0.6	0.824
3429.87	78.1	0.390	0.70	6	4.2 ± 0.6	0.831
3494.43	79.6	0.503	1.57	6	6.7 ± 0.7	0.769
3510.41	19.2	1.125	1.53	13		0.779
3511.17	20.7	0.218	1.11	1		0.815
3509.80	20.8	0.235	1.21	2		0.806
3511.75	21.3	0.320	1.56	4		0.784
3510.54	21.4	0.315	1.37	3		0.795
3509.22	21.5	0.304	1.13	4		0.812
3510.78	74.1	0.780	1.52	6		0.773
3510.83	75.1	1.148	2.32	17		0.721
3513.00	65.1	0.301	2.08	2		0.736
3511.45	65.2	0.315	2.09	4		0.733
3511.05	65.3	0.071	2.08	4		0.732
3510.75	65.4	0.319	2.09	1		0.731
3510.36	65.5	0.315	1.95	5		0.740
3509.93	65.6	0.317	1.91	1		0.747
3508.59	65.7	0.376	1.93	4		0.743
3524.64	61.1	3.717	1.87	50		0.751
3525.16	58.1	2.903	1.78	32		0.754
3525.51	62.1	3.532	1.94	43		0.747
3525.64	21.2	1.801	1.92	18		0.763
3525.68	55.1	3.478	1.73	43		0.750
3525.78	60.1	2.976	1.88	32		0.750
3525.80	63.1	3.934	2.04	48		0.736
						continued on next page

$\sqrt{s}$ (MeV)	stack	$\int Ldt$ (pb^{-1})	inst. lum. ($10^{31}cm^{-2}s^{-1}$)	$N_{\gamma\gamma}$	N_{feed}	ϵ_{total}
continued from previous page						
3525.86	59.1	1.196	1.96	16		0.743
3526.09	19.1	1.986	1.94	16		0.756
3525.68	56.1	2.291	1.90	32		0.748
3526.13	20.6	1.865	1.91	21		0.761
3526.16	57.1	3.309	2.01	33		0.741
3526.51	64.1	3.234	2.00	42		0.740
3526.52	51.1	0.976	1.84	10		0.748
3526.61	54.1	0.649	1.89	7		0.746
3526.84	21.1	1.984	1.99	20		0.751
3526.89	52.1	3.094	1.80	30		0.741
3527.49	53.1	1.396	1.53	17		0.777
3529.10	50.2	2.328	1.63	28		0.766
3535.45	15.3	1.304	1.95	13		0.751

Table A.1: Summary of the $\gamma\gamma$ data taken near the η_c and χ_0 resonances.

χ_2 and η_c' data						
$\sqrt{s}$ (MeV)	stack	$\int Ldt$ (pb^{-1})	inst. lum. ($10^{31}cm^{-2}s^{-1}$)	$N_{\gamma\gamma}$ $\alpha = 0.40$	$N_{\gamma\gamma}$ $\alpha = 0.45$	ϵ_{total}
3524.64	61.1	3.717	1.87	58	77	0.751
3525.16	58.1	2.903	1.78	38	50	0.754
3525.51	62.1	3.532	1.94	50	65	0.747
3525.64	21.2	1.801	1.92	27	31	0.763
3525.68	55.1	3.478	1.73	55	67	0.750
3525.78	60.1	2.976	1.88	38	47	0.750
3525.80	63.1	3.934	2.04	56	66	0.736
3525.86	59.1	1.196	1.96	21	26	0.743
3526.09	19.1	1.986	1.94	24	27	0.756
3525.68	56.1	2.291	1.90	38	45	0.748
3526.13	20.6	1.865	1.91	25	29	0.761
3526.16	57.1	3.309	2.01	41	55	0.741
3526.51	64.1	3.234	2.00	55	68	0.740
3526.52	51.1	0.976	1.84	12	14	0.748
3526.61	54.1	0.649	1.89	10	12	0.746
3526.84	21.1	1.984	1.99	24	29	0.751
3526.89	52.1	3.094	1.80	37	47	0.741
3527.49	53.1	1.396	1.53	21	24	0.777
						continued on next page

$\sqrt{s}$ (MeV)	stack	$\int Ldt$ (pb^{-1})	inst. lum. ($10^{31}cm^{-2}s^{-1}$)	$N_{\gamma\gamma}$ $\alpha = 0.40$	$N_{\gamma\gamma}$ $\alpha = 0.45$	ϵ_{total}
continued from previous page						
3529.10	50.2	2.328	1.63	34	40	0.766
3535.45	15.3	1.304	1.95	15	20	0.751
3544.79	4.4	0.998	1.23	8	12	0.814
3554.66	20.5	0.490	1.96	8	9	0.757
3555.16	4.3	0.519	1.52	11	13	0.788
3555.57	20.4	0.411	1.99	10	12	0.757
3555.92	38.3	0.516	1.93	14	16	0.742
3555.99	50.1	0.994	1.96	30	34	0.742
3556.03	9.2	0.605	2.47	12	16	0.719
3556.06	9.3	0.778	1.00	23	26	0.827
3556.08	20.3	0.413	1.94	9	10	0.754
3556.18	4.2	0.521	1.59	11	14	0.780
3556.26	79.5	0.501	1.84	12	13	0.753
3556.33	38.2	0.752	2.12	15	18	0.731
3556.65	38.1	0.810	2.09	27	28	0.729
3556.76	20.2	0.401	1.90	11	11	0.758
3557.30	4.1	0.896	1.48	14	18	0.785
3557.93	20.1	0.383	1.96	9	11	0.754
3576.05	17.3	1.606	2.01	23	27	0.752
3580.09	12.2	0.583	1.85	12	13	0.767
3580.87	11.2	0.627	2.41	11	12	0.734
3585.19	13.2	1.506	2.07	18	20	0.748
3590.25	11.1	1.484	1.79	24	30	0.777
3595.62	12.1	1.507	1.92	21	22	0.764
3600.50	9.1	1.594	1.58	24	27	0.780
3604.00	6.4	1.479	1.63	21	23	0.781
3607.53	15.2	1.524	2.17	14	17	0.741
3610.58	8.2	0.922	1.55	6	9	0.779
3614.71	6.3	1.538	1.97	32	34	0.757
3620.59	7.3	1.472	1.65	21	24	0.780
3625.30	5.2	1.637	1.90	22	29	0.755
3629.75	7.2	1.619	1.64	16	19	0.773
3633.14	77.1	2.014	2.30	28	32	0.715
						continued on next page

$\sqrt{s}$ (MeV)	stack	$\int Ldt$ (pb^{-1})	inst. lum. ($10^{31}\mathrm{cm}^{-2}\mathrm{s}^{-1}$)	$N_{\gamma\gamma}$ $\alpha = 0.40$	$N_{\gamma\gamma}$ $\alpha = 0.45$	ϵ_{total}
continued from previous page						
3633.65	69.1	2.573	2.31	17	23	0.715
3635.17	6.2	1.408	1.99	21	26	0.747
3639.98	15.1	1.498	2.24	26	30	0.732
3643.46	10.2	1.233	1.67	20	20	0.776
3644.30	5.1	1.723	1.86	23	28	0.760
3651.63	14.1	1.456	2.02	11	14	0.749
3656.07	10.1	1.646	2.04	12	16	0.751
3660.48	13.1	1.486	1.94	20	21	0.752
3685.67	6.1	1.436	2.10	13	16	0.613
3686.21	7.1	1.085	1.67	18	21	0.646
3686.24	8.1	1.101	1.68	4	7	0.648
3686.20	17.2	0.310	1.59	2	2	0.652
3687.03	39.1	0.319	2.04	1	1	0.614
3686.81	39.2	0.477	2.02	5	6	0.624
3686.65	40.1	0.272	1.53	4	5	0.638
3686.61	40.2	0.199	1.45	3	3	0.643
3686.38	40.3	0.308	1.51	5	7	0.643
3686.34	40.4	0.260	2.09	3	4	0.612
3686.19	40.5	0.116	1.95	0	1	0.626
3686.04	40.6	0.183	1.87	2	3	0.624
3685.80	40.7	0.120	1.85	1	2	0.627
3687.29	67.1	0.320	2.03	1	1	0.614
3686.78	67.2	0.326	2.04	7	8	0.613
3686.51	67.3	0.307	1.85	3	4	0.627
3686.24	67.4	0.213	1.96	1	1	0.619
3685.98	67.5	0.213	1.96	1	2	0.618
3685.70	67.6	0.111	1.89	1	2	0.632
3685.25	67.7	0.335	1.88	0	1	0.627

Table A.2: Summary of the $\gamma\gamma$ data taken between the ${}^1P_1$ and ψ' resonances.

Appendix B

$\pi^0\pi^0$ event selection

With $\approx 7,500$ events per pb^{-1} at the ψ', and over 150,000 per pb^{-1} below the η_c, $\pi^0\pi^0$ events are plentiful and convenient for many detector studies. The selection criteria are described here, because these events are used frequently, each time with slightly different values for the cuts, depending mostly upon differing personal preferences. The specific cut values are listed in table B.1.

Each possible combination of the four photons into π^0s is considered and the combination with the smallest value of the quantity $\sqrt{(2\Delta\theta)^2 + (\Delta\phi)^2}$ is chosen. $\Delta\theta$, $\Delta\phi$, and the other variables used to select the events are defined below.

- Number of CCAL clusters.
- Energy and seed threshold used to form CCAL clusters.
- *acoplanarity* $\equiv \Delta\phi \equiv \pi - \mid \phi_1 - \phi_2 \mid$
- *akinematics* $\equiv \Delta\theta \equiv \theta_{1pred}(\theta_{2meas}) - \theta_{1meas}$, where $\theta_1 \leq \theta_2$.
- *invarient mass* $\equiv M_\pi = 2E_{\gamma_1}E_{\gamma_2}(1 - \cos\Theta_{open})$, where Θ_{open} is the angle between the two photons in the lab frame. This cut is applied unless the clusters forming the π^0 are the two halves of a split cluster.

- *fiducial volume* Requiring all four photons to be within a restricted θ region.

All angles mentioned are the angles of the π^0s in the lab frame. The distributions of these variables can be seen in figure B.1.

	CCAL calibration	vertex determination	CCAL timing
CCAL clusters	Exactly 4	Exactly 4	Exactly 4
seed/cluster threshold	25/50	25/50	5/20
$\mid \Delta\theta \mid$ (mrad)	10	10	15
$\mid \Delta\phi \mid$ (mrad)	32	32	30
$\mid M_\pi - 135 \mid$ (MeV)	40	35	35
fiducial volume	none	none	rings 2-18
reference	section 3.5	section 3.6	section 3.7
	neutral DST efficiency	monte carlo testing	$\pi^0\pi^0$ cross section
CCAL clusters	4 i.o.u.	Exactly 4	4 i.o.u.
seed/cluster threshold	25/50	5/20	25/50
$\mid \Delta\theta \mid$ (mrad)	15	15	2σ
$\mid \Delta\phi \mid$ (mrad)	32	30	30
$\mid M_{\gamma\gamma} - 135 \mid$ (MeV)	35	35	35
fiducial volume	rings 2-18	rings 2-18	rings 2-18
reference	appendix E	section 4.1	section 4.2

Table B.1: Cuts used in $\pi^0\pi^0$ event selections. "i.o.u." stands for "in-time or undetermined" clusters.

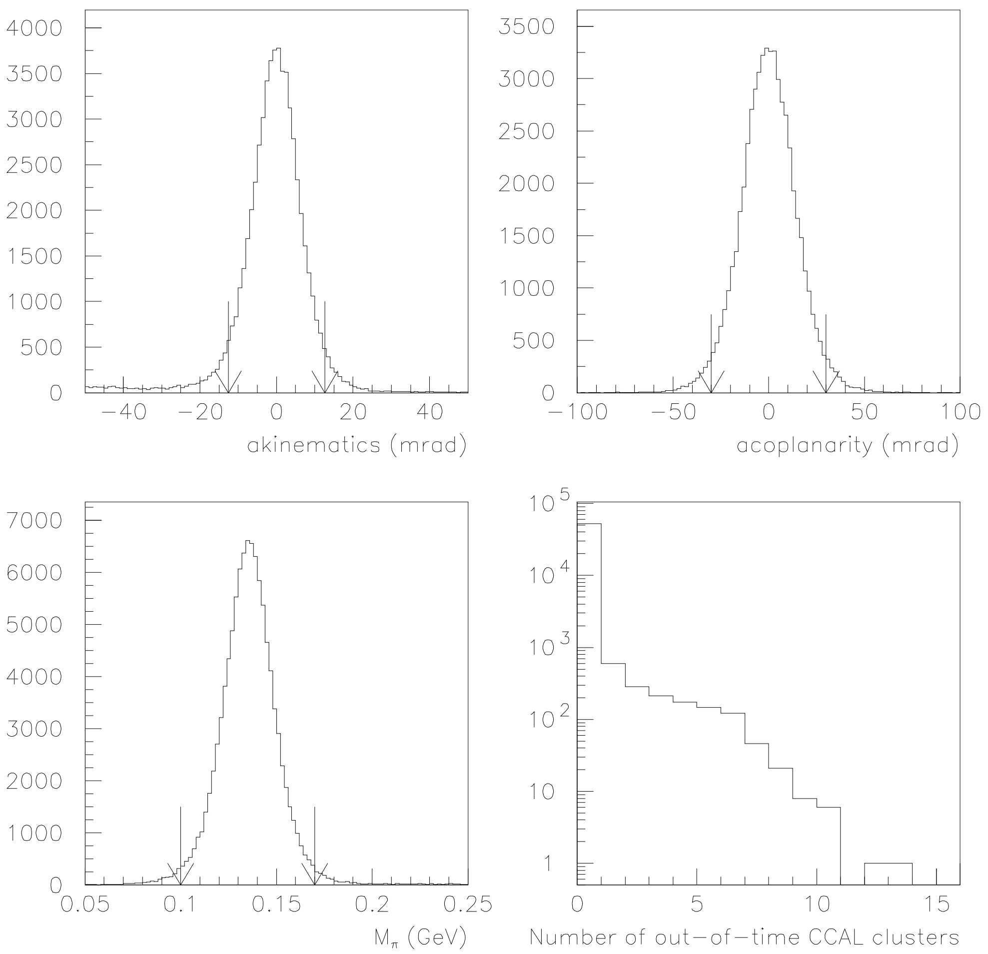

Figure B.1: The variables used to select clean $\pi^0\pi^0$ events, plotted after applying all cuts expect the variable shown.

.

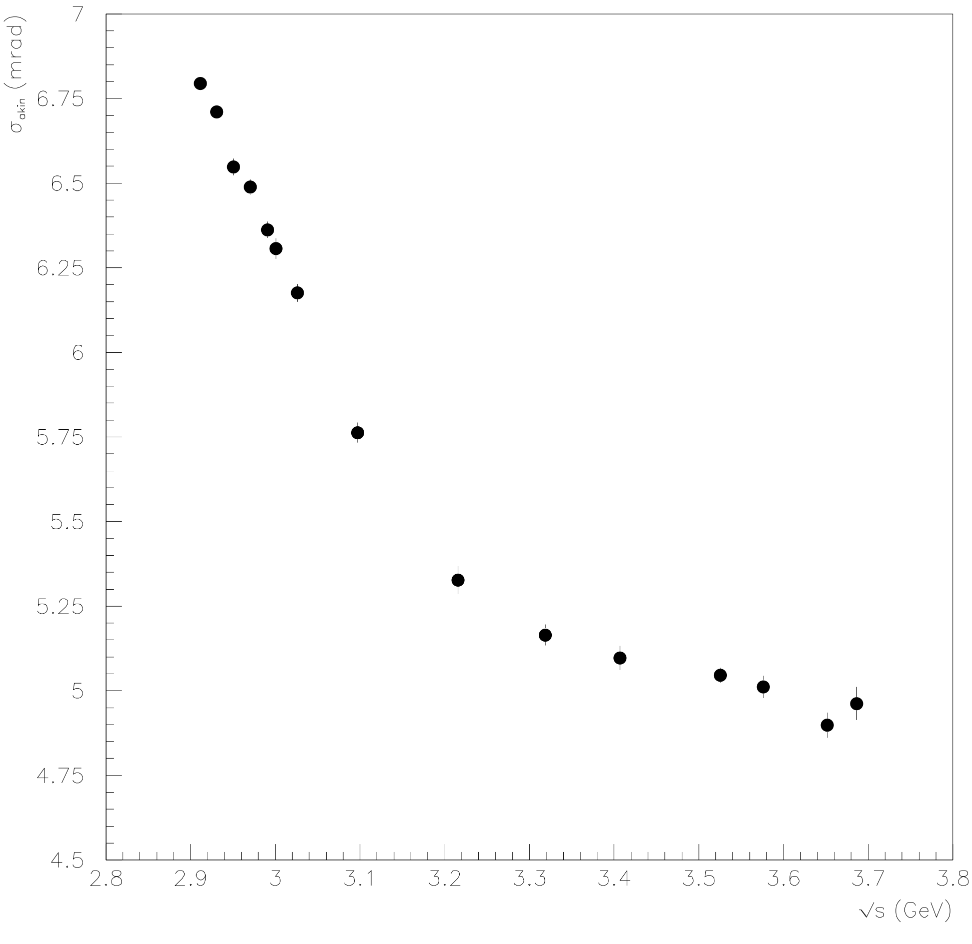

Figure B.2: The width of the akinematics distribution as a function of $\sqrt{s}$.

Appendix C

Photon Conversion Probability

If a photon converts into a e^+e^- pair in the beampipe, and is within the CCAL acceptance, it will turn on the neutral veto and prevent the event from satisfying the GM4 or GM5 trigger (see section 2.6). Understanding how frequently this occurs is an important factor in calculating the efficiency of the $\pi^0\pi^0$, $\pi^0\gamma$, and $\gamma\gamma$ event selection.

A selection of $\pi^0\pi^0$ events from the "ETOT-no-veto" data set (see section 2.5) are ideal for studying this. These events were separated from the rest of the data during the production of the neutral DSTs (see Appendix E), but were subject to an additional prescale factor of 5. A total of 3014 events satisfied the $\pi^0\pi^0$ cuts defined in appendix B providing 12056 photons to study.

First, the hodoscope signals are used to identify charged tracks that could be associated with one of the four clusters in the CCAL. A track is defined as a signal, intime and above 0.5 mips, in H1 and a signal, intime and above 1.0 mips, in either H2 or H2', where only the counters corresponding to the the ϕ coordinate of the associated cluster in the CCAL are considered. Finally, the charged component of the neutral veto is also required to be on. The two photons from a π^0 decay often traverse the same counter in the hodoscopes, so when necessary the signals in the fibers and the straws are used to determine which photon from the π^0 converted.

Since a photon that converts in the beampipe material and one from a π^0 that Dalitz decays are indistinguishable, the fraction of photons associated with a track, P_{track}, is related to $P_{\gamma\ conv}$ by the equation

$$P_{track} = \epsilon_{track} \times [P_{\gamma\ conv} + 0.5 * P_{\pi^0\,Dalitz}] \tag{C.1}$$

where ϵ_{track} is the probability that an e^+e^- pair is identified as a track and the quantity $P_{\pi^0\,Dalitz} = 0.012$ is already well-measured[52].

The fraction of photons associated with a track is plotted as a function of θ and ϕ in figure C.1. Both H1 and the beampipe itself were designed so that a particle incident from the gas jet traverses the same amount of material at any θ. Thus, we do not expect to see any θ dependence in the conversion probability. The data are consistent with a flat distribution in both θ and ϕ .

Out of the original 12,056 photons, 198 are associated with tracks. Since ϵ_{track} is dominated by the efficiency of the neutral veto, $\epsilon_{track} \approx \epsilon_{veto} = 0.85 \pm 0.05$[26]. Finally, $\epsilon_{veto} \times P_{\gamma\ conv} = 1.13 \pm 0.12(stat) \pm 0.03(syst)\%$ emerges as the probability, per photon in the event, that a good neutral event would be lost because of a photon conversion in the beampipe or H1.

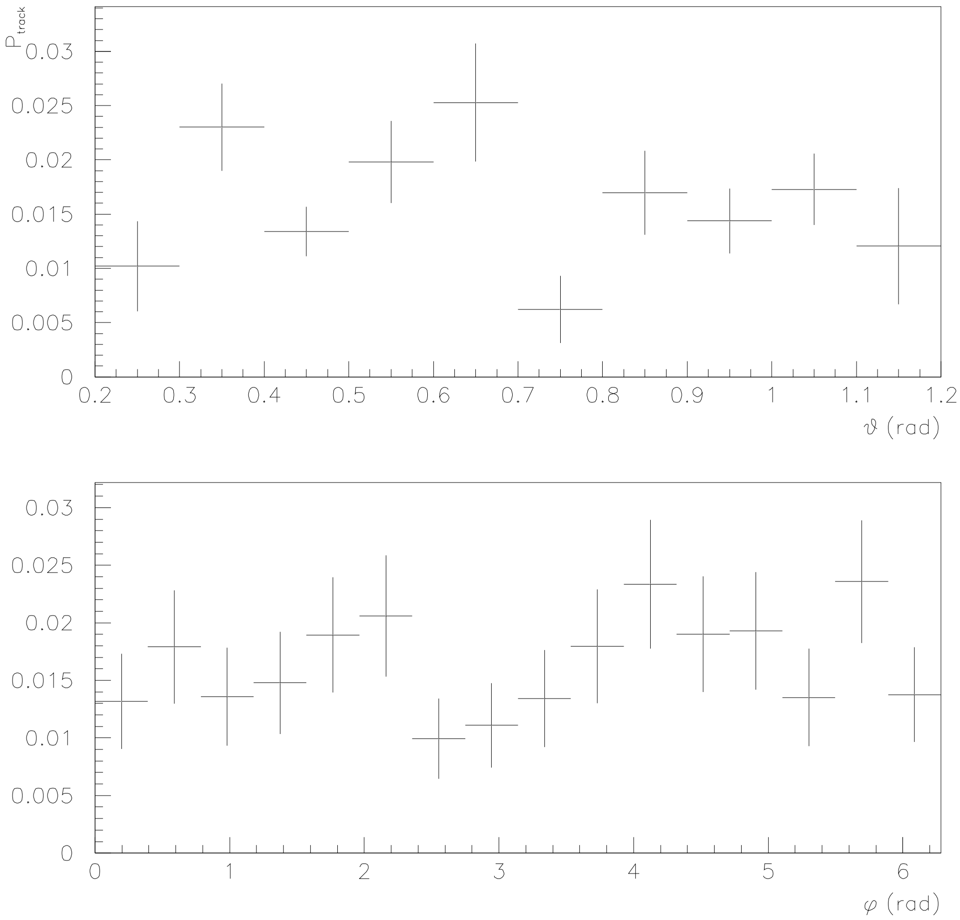

Figure C.1: The probablity that an e^+e^- signal was seen when a photon was expected is plotted as a function of θ and ϕ. The vertical error bars are statistical and the horizontal error bars indicate the bin width.

Appendix D

Neutral Trigger Efficiency

There are two branches of the neutral hardware trigger: PBG1 and ETOT. PBG1 looks for two large energy deposits in the CCAL consistent with two-body kinematics and ETOT requires 90% of the total available energy to be deposited into the CCAL. The ETOT trigger can be inefficient when more than 10% of the total cluster energy is lost in the cracks in the CCAL. For $\pi^0\pi^0$ events, the PBG1 trigger is inefficient when the two photons of the π^0 are not within the same superblock. However, the analyses combine the data from the two triggers, and the efficiency of the combined trigger has been shown to be 100% for the $\pi^0\pi^0$ data sample, and thus 100% for the $\pi^0\gamma$ and $\gamma\gamma$ data as well[59].

Assuming that any inefficiencies in one branch of the trigger is incorrelated with inefficiencies in the other branch, the trigger efficiency can be monitored by counting the fraction of ETOT events which did not pass the PBG1 trigger, and the fraction of PBG1 not passing ETOT. For the $\pi^0\pi^0$ data, the product was checked for every stack and always found to be $<< 0.01$.

The inefficiency of the combined trigger due to the three dead channels in the CCAL is less than 1%. It is not included here since it is already included in the analysis efficiency calculated with the Monte Carlo.

One categorization (PRUDE ID 51) of the online filter was prescaled with a factor of 2(4) above(below) transition. Only a few of the $\pi^0\pi^0$ events and none of the $\gamma\gamma$ events were in this category. The $\pi^0\pi^0$ events categorized this way were counted twice above transition, and counted four times below transition. Multiple counting of events means that the same event was entered n times into the angular distribution histogram, while using the original number of events (without multiple counting) for the statsistical errors of each bin. The same technique is used to monitor the efficiency of the online filter, which treats each branch of the trigger separately. The product of the inefficiencies for each branch of the filter is also negligible.

Finally, there is a set of data-points for which a discriminator in the PBG1 trigger (super-ring 4) was not functioning properly (data-points 20.3-29.1, runs 1370-2107). The trigger efficiency as a function of angle has been calculated as the fraction of ETOT triggers that did not satisy PBG1, and an angular dependent correction made to the $\pi^0\pi^0$ and $\pi^0\gamma$ data. The efficiency of ETOT alone is above 95% for the $\pi^0\pi^0$ data and 100% for the $\gamma\gamma$ data, so this is a small correction. However, for a small subset of this data (data-points 23.2-29.1 runs 2042-2106), the ETOT trigger was unintentionally prescaled by a factor of 5. For these runs, events with the ETOT trigger ON and the PBG1 trigger OFF were counted five times.

Appendix E

Neutral DST production and efficiency

Data summary tapes, or DSTS, are created to facilitate analyses on large amounts of data. The neutral DSTs in particular are a subset of the original data set that have no strong charged signal and satisfy loose momentum conservation requirements. The events are stored in a more compact form, retaining the cluster information from the detectors instead of the electronic readout of each channel.

The cuts imposed to create the neutral DSTs are:

- Exactly four intime or undetermined clusters
- No more than 10 clusters found by PRUDE
- $|P_z - P_{beam}| \leq 0.15 * P_{beam}$
- $P_t \equiv \sqrt{P_x^2 + P_y^2} \leq 350 MeV$

where P_x (P_y, P_z) is the sum of the x(y,z) component of momentum for all particles associated with a CCAL cluster and P_{beam} is the measured momentum of the antiproton beam.

The efficiency of these cuts on the $\pi^0\pi^0$ data was calculated using a clean $\pi^0\pi^0$ sample extracted from the raw data of 15 runs, with a large range of both $\sqrt{s}$ values and instantaneous luminosity. The fraction of events surviving the above cuts is plotted as a function of $\sqrt{s}$ in figure E.1. The results were fit to a second degree polynomial and this function used to correct the data. No dependence upon the instantaneous luminosity was found.

Since a small amount of background is present in the $\pi^0\pi^0$ sample, it is possible that the neutral DST production cuts are reducing the percentage of background in the data in addition to, or instead of, actually discarding good $\pi^0\pi^0$ events. As a check, the fraction of background events in the sample was calculated, using the method of section 4.2, before and after applying the cuts. Since the percentage of background events in the data sample did not change, the efficiency shown in figure E.1 is used to correct the $\pi^0\pi^0$ cross section after subtracting the background.

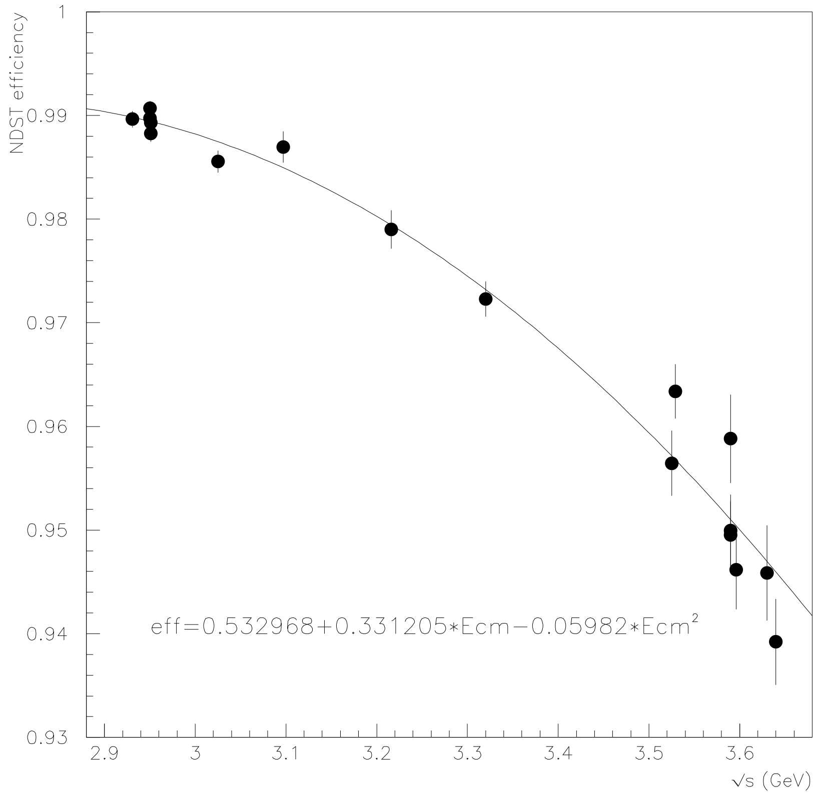

Figure E.1: Efficiency of the neutral DST production cuts as a function of $\sqrt{s}$. The line is the best fit to the data.

Appendix F

Angular Distribution of $\overline{p}p \to \chi_2 \to \gamma\gamma$

Calculation of angular distributions for relativistic scattering processes is complicated by the fact that the orbital angular momentum operator ($\vec{L}$) and the spin angular momentum operator ($\vec{S}$) are no longer defined in the same rest frame once the particles are relativistic. The helicity formalism developed by Jacob and Wick[57] is widely used for relativistic problems. The helicity operator $h = \vec{S} \cdot \hat{p}$ is invariant under both rotations and boosts along $\hat{p}$, thus one can find a set of basis vectors that are eigenstates of total angular momentum and helicity (spherical wave states), or eigenstates of linear momentum and helicity (plane wave states). This derivation uses the notations and conventions of references [74] and [65].

F.1 General two-body decay

The decay of a particle at rest to a two-body final state, $\alpha \to 1+2$, is characterized by the mass m_α, spin J, and spin projection M along an arbitrary z-axis of the initial state particle and the momenta $\vec{p}_1 = \vec{p}_f, \vec{p}_2 = -\vec{p}_f$ and helicities λ_1, λ_2 of the final state particles. Working in the rest frame of the particle α, the amplitude for particles

1 and 2 to emerge with angles θ, ϕ.

$$A(\alpha \to f) = < \theta_f \phi_f \lambda_1 \lambda_2 | U | JM > \tag{F.1}$$

where θ_f, ϕ_f are the polar angles of $\vec{p}_f$ and U is the time-evolution operator.

Insertion of a complete set of two-particle spherical helicity eigenstates allows angular momentum conservation to simplify the matrix element.

$$\begin{aligned} A(\alpha \to f) &= < \theta_f \phi_f \lambda_1 \lambda_2 | \left[\sum_{J_f, M_f} \sum_{\lambda_1' \lambda_2'} | J_f M_f \lambda_1' \lambda_2' >< J_f M_f \lambda_1' \lambda_2' | \right] U | JM > \\ &= \sum_{J_f, M_f} \sum_{\lambda_1' \lambda_2'} < \theta_f \phi_f \lambda_1 \lambda_2 | J_f M_f \lambda_1' \lambda_2' > \delta_{J_F, J} \delta_{M_f, M} < \lambda_1' \lambda_2' | U | M > \end{aligned}$$

The first matrix element can be simplified using the $D^J_{M,\lambda}$ functions found in reference [52]

$$< \theta \phi \lambda_1 \lambda_2 | JM \lambda_1' \lambda_2' >= \delta_{\lambda_1 \lambda_1'} \delta_{\lambda_2 \lambda_2'} \left[\frac{2J+1}{4\pi} \right]^{1/2} D^J_{M\lambda}(\phi, \theta, -\phi) \tag{F.2}$$

whre $\lambda = \lambda_1 - \lambda_2$. The amplitude becomes

$$A(\alpha \to f) = \left[\frac{2J+1}{4\pi} \right]^{1/2} D^J_{M\lambda}(\phi, \theta, -\phi) < \lambda_1 \lambda_2 | U | M > \tag{F.3}$$

Furthermore, the amplitude must be symmetric in ϕ, so it can be simplified by setting $\phi = 0$.

$$A(\alpha \to f) = \left[\frac{2J+1}{4\pi} \right]^{1/2} d^J_{M,\lambda}(\theta) C_{\lambda_1, \lambda_2} \tag{F.4}$$

where $C_{\lambda_1, \lambda_2} \equiv < \lambda_1 \lambda_2 | U | M >$.

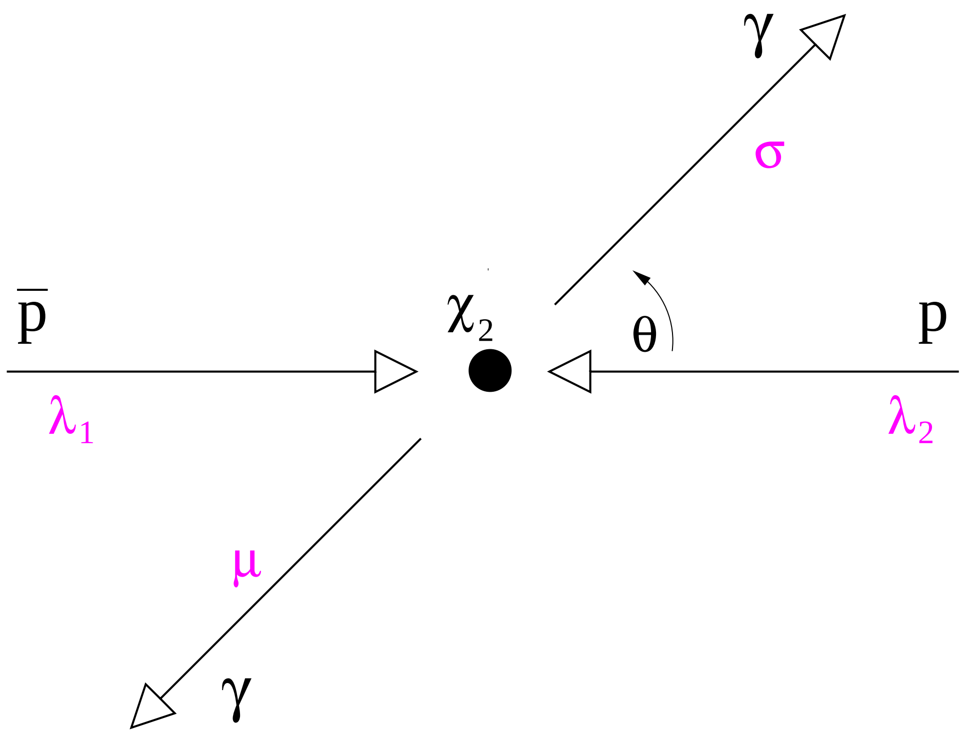

Figure F.1: Diagram of the process $\overline{p}p \to \chi_2 \to \gamma\gamma$

F.2 χ_2 amplitudes

Now the details specific to the χ_2 are added to the previous discussion. Figure F.1 labels the initial and final state particles with helicity indeces in grey. Using B to denote production amplitudes and A to denote decay amplitudes and substituting J=2 into equation F.4 yields

$$A(\overline{p}p \to \chi_2) = \sqrt{\frac{5}{4\pi}} B_{\lambda_1,\lambda_2} d^2_{M,\lambda}(\theta) \tag{F.5}$$

$$A(\chi_2 \to \gamma\gamma) = \sqrt{\frac{5}{4\pi}} A_{\sigma,\mu} \delta_{M,\nu} \tag{F.6}$$

where $\theta = 0$ in the decay amplitude by convienent choice of the spin quantization axis, giving $D^J_{M,\nu=\sigma-\mu}(\phi, 0, -\phi) = \delta_{M,\nu}$.

The total angular distribution combines the previous amplitudes

$$\begin{aligned}\frac{d\sigma}{d\Omega} &\propto \frac{1}{4}\sum_{\sigma,\mu}\sum_{\lambda_1,\lambda_2}|A(\overline{p}p \to \chi_2)A(\chi_2 \to \gamma\gamma)|^2 \\ &= \frac{1}{4}\left(\frac{5}{4\pi}\right)^2\sum_{\sigma,\mu}\sum_{\lambda_1,\lambda_2}|A_{\sigma,\mu}|^2|B_{\lambda_1,\lambda_2}|^2|d^2_{\lambda,\nu}(\theta)|^2 \end{aligned} \tag{F.7}$$

where the initial states have been averaged over and the final states summed over.

The proton and antiproton in the initial state can have helicity of +1/2,-1/2, and the two photons in the final state can each have helicity +1,-1. Therefore, there are four amplitudes ($B_{+1/2,+1/2}, B_{-1/2,+1/2}, B_{+1/2,-1/2}, B_{-1/2,-1/2}$) for the formation process and four amplitudes for the ($A_{+1,+1}, A_{-1,+1}, A_{+1,-1}, A_{-1,-1}$) decay process which can contribute to the sums in equation F.7. We can relate some of the amplitudes $A_{\sigma,\mu}, B_{\lambda_1,\lambda_2}$ with conservation of parity and charge conjugation. In general, these relations are written

$$C_{\lambda_1,\lambda_2} = (\mathrm{P})(-1)^J C_{-\lambda_1,-\lambda_2} \qquad \text{(Parity)} \tag{F.8}$$

$$C_{\lambda_1,\lambda_2} = (\mathrm{C})(-1)^J C_{\lambda_2,\lambda_1} \qquad \text{(Charge Conjugation)} \tag{F.9}$$

After substituting the quantum numbers of the χ_2, $J^{PC} = 2^{++}$, equations F.8 and F.9 reveal that there are only two independent amplitudes each for the formation and decay processes.

$$B_{\lambda_1,\lambda_2} = B_{-\lambda_1,-\lambda_2} \quad ; \quad B_{\lambda_1,\lambda_2} = B_{\lambda_2,\lambda_1} \tag{F.10}$$

$$A_{\sigma,\mu} = A_{-\sigma,-\mu} \quad ; \quad A_{\sigma,\mu} = A_{\mu,\sigma} \tag{F.11}$$

Each amplitudes is relabeled with the absolute value of the total helicity, $\lambda = \lambda_1 - \lambda_2$ for formation and $\nu = \sigma - \mu$ for decay as defined below

$$
\begin{aligned}
\frac{1}{2}B_0^2 &\equiv B^2_{\frac{1}{2},\frac{1}{2}} = B^2_{-\frac{1}{2},-\frac{1}{2}} \qquad (|\lambda| = 0) \\
B_1^2 &\equiv B^2_{\frac{1}{2},-\frac{1}{2}} = B^2_{-\frac{1}{2},\frac{1}{2}} \qquad (|\lambda| = 1) \\
\frac{1}{2}A_0^2 &\equiv A^2_{1,1} = A^2_{-1,-1} \qquad (|\nu| = 0) \\
\frac{1}{2}A_2^2 &\equiv A^2_{1,-1} = A^2_{-1,1} \qquad (|\nu| = 2)
\end{aligned}
$$

Evaluating the sums in equation F.7, using the variable definitions in equations F.12, the angular distribution for the reaction can be written as

$$
\begin{aligned}
\frac{d\sigma}{d\Omega} \propto\ & A_0^2 B_0^2 (d^2_{0,0}(\theta))^2 + 2A_0^2 B_1^2 (d^2_{0,1}(\theta))^2 + \\
& A_2^2 B_0^2 (d^2_{2,0}(\theta))^2 + A_2^2 B_1^2 (d^2_{2,1}(\theta)^2 + d^2_{2,-1}(\theta)^2)
\end{aligned}
\tag{F.12}
$$

Finally, the angular dependence is explicitly shown by inserting the d-functions

$$
\frac{d\sigma(\overline{p}p \to \chi_2 \to \gamma\gamma)}{d\Omega} \propto \left[K_1 + K_2 \cos^2\theta + K_3 \cos^4\theta\right] \tag{F.13}
$$

where

$$
\begin{aligned}
K_1 &\equiv (2A_2^2)R + (2A_0^2 + 3A_2^2)(1 - R) \\
K_2 &\equiv (12A_0^2)R + (-12A_0^2 - 6A_2^2)(1 - R) \\
K_3 &\equiv (-12A_0^2 - 2A_2^2)R + (18A_0^2 + 3A_2^2)(1 - R) \\
R &\equiv \frac{2B_1^2}{B_0^2 + 2B_1^2}
\end{aligned}
$$

In addition, the normalization conventions that have been used are $A_0^2 + A_2^2 = 1$ and $B_0^2 + 2B_1^2 = 1$.

Appendix G

Statistical Interpretation of Data

There are two approaches to determining confidence intervals in statistical theory, *Bayesian* and *frequentist*. The two approaches differ in their treatment of the function P(x|μ) the probability distribution for a random variable x which depends upon a parameter μ.

Under the conditions that the probability distribution P(x|μ) is Gaussian, that the parameter μ is far from any physical boundary (*far* being defined by the experimental resolution), and that the number of events in the experiment is large, the two approaches result in identical confidence intervals even though the underlying theories are quite different.

The E835 data are near the boundary $\sigma_{peak} = 0$, and the resulting confidence intervals depend upon the method used. The unified frequentist approach presented by Feldman and Cousins in a recent paper[48] was chosen to present the results in section 6.6. In this appendix, the confidence intervals are calculated with two other methods: the Bayesian approach and the standard frequentist approach, both of which are outlined in the 1994 version of the PDG[52]. The results of all three approaches are compared.

G.1 Frequentist Confidence Intervals

The frequentist approach requires that P(x$|\mu$) be known or calculated with a series of Monte Carlo experiments. An interval $[x_1, x_2]$ is constructed for every μ such that

$$\int_{x_1}^{x_2} \mathrm{P}(x \mid \mu) dx = 1 - \epsilon \tag{G.1}$$

where $1 - \epsilon$ is the desired coverage. There are many values for x_1, x_2 that satisfy this equation. There is a convention among experimenters that either the symmetric confidence interval or an upper limit be quoted. The symmetric interval satisfies the equations

$$\int_{-\infty}^{x_1} \mathrm{P(x}|\mu) dx = \frac{\epsilon}{2} \quad , \quad \int_{x_2}^{+\infty} \mathrm{P(x}|\mu) dx = \frac{\epsilon}{2} \tag{G.2}$$

Once a method for choosing the interval $[x_1, x_2]$ is decided, equation G.1 gives two curves, $x_1(\mu)$ and $x_2(\mu)$. These curves can be inverted to give $\mu_2(x)$ and $\mu_1(x)$ respectively. For a given measurement x, the confidence interval is $[\mu_1, \mu_2]$.

The unified approach by Feldman and Cousins uses a likelihood ratio to specify the choice of the interval $[x_1, x_2]$. The interval is the region with the largest values of the ratio

$$R(x) \equiv \frac{\mathrm{P(x}|\mu)}{\mathrm{P}(x \mid \mu_{best})} \tag{G.3}$$

where μ_{best} is redefined as the value of μ that maximizes P(x$|\mu$) AND is in the physical region. For example, if $\mu = -1.3$ is the value that maximizes P(x$|\mu$) and μ is constrained to be non-negative, then $\mu_{best} = 0$. When the probability distribution is Gaussian and the measurement is far from a physical boundary, the unified approach produces symmetric intervals. Near the boundary, the lower limit of the interval becomes the boundary, i.e. $\mu_1 = 0$ in the example above, and there is a smooth transition from a two-sided interval to an upper limit.

G.2 Bayesian Confidence Intervals

The Bayesian approach asserts that the confidence intervals can be obtained from the likelihood function, L(μ |x), which is constructed from experimental measurements. For an efficient estimator, x, the two distributions are related by Bayes' theorem,

$$\mathrm{L}(\mu \mid x) = \mathrm{P}(x \mid \mu)\frac{\mathrm{P}(\mu)}{\mathrm{P}(x)} \tag{G.4}$$

where P(x) serves to normalize the likelihood function and P(μ) is called the *prior* function for μ. The prior is often assumed to be constant. The same definition of coverage applies as before: given an observed value x for the estimator, the confidence interval is given by

$$\int_{\mu_1}^{\mu_2} \mathrm{L}(\mu \mid x) = 1 - \epsilon \tag{G.5}$$

If the likelihood function is Gaussian and far from a physical boundary, the confidence interval is the same as that obtained with the frequentist approach.

In the 1994 edition of the PDG, a Bayesian method for handling limits near a physical boundary is outlined that assumes a constant prior distribution for the probability of the true value, and restricts the true value to be non-negative. The upper limits on the true value are obtained by renormalizing the likelihood function. The upper limit is the value $\mu = \mu_0$ for which the fraction $1 - \epsilon$ of the area underneath the likelihood function from 0 to ∞ is contained between 0 and μ_0. If the likelihood function is Gaussian, i.e.

$$\frac{L}{L_{\max}} \propto e^{\frac{-(\mu-\mu_{best})^2}{2\sigma_{\mu}^2}} \tag{G.6}$$

then the upper limit μ_0 is given by

$$\frac{erfc\,(\ln L_{\max} - \ln L(\mu = \mu_0))}{erfc\,(\ln L_{max} - \ln L(\mu = 0))} = \epsilon \tag{G.7}$$

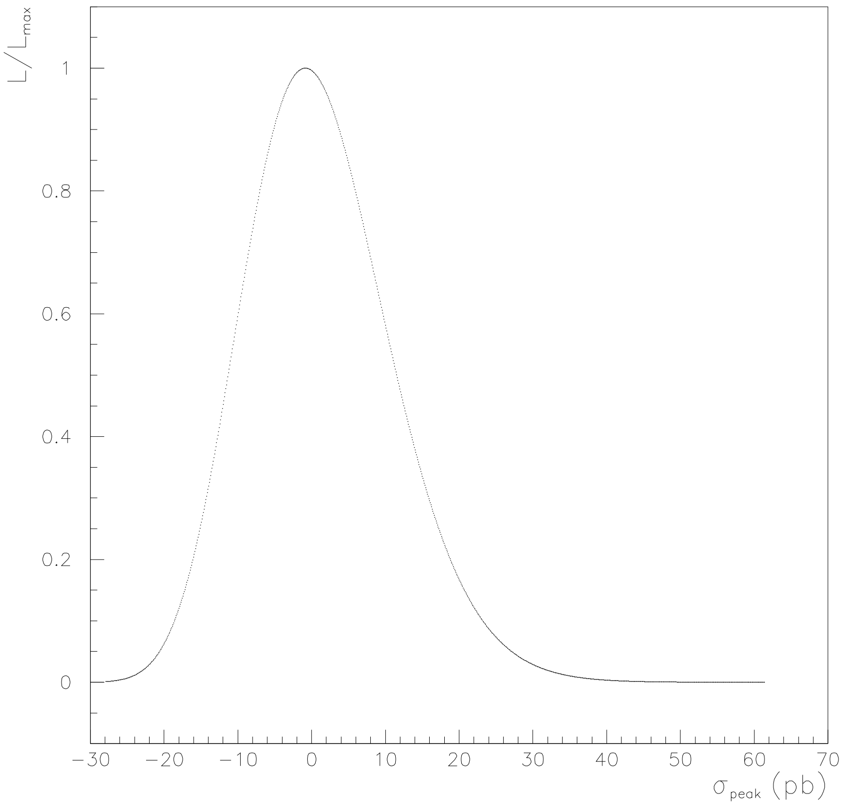

Figure G.1: The likelihood function is plotted as a function of the peak cross section for the fixed values $M_{\eta_c'} = 3660$ MeV and $\Gamma_{\eta_c'} = 5$ MeV.

where $1-\epsilon$ is the desired coverage of the limit and μ_{best} is the value of μ that maximizes the likelihood function.

G.3 E835 data and comparisons

The likelihood function calculated for the E835 data is shown as a function of σ_{peak} in figure G.1. In section 6.6, it is shown that the variance of the probability distribution P(x|μ) is given by the negative inverse second derivative of the likelihood function, evaluated at its maximum. When the physical boundary is ignored, the frequentist confidence intervals are equivalent to the Bayesian ones. These are shown in figure G.3 for three different values of the resonance mass.

These limits can be compared with the two different methods for handling the physical boundary. Figure G.3 compares the upper limits in the three cases for a width $\Gamma = 5$ MeV. For larger values of the upper limit, the three methods have similar results. However, they begin to differ for $B_{in}B_{out} < 3 \times 10^{-8}$.

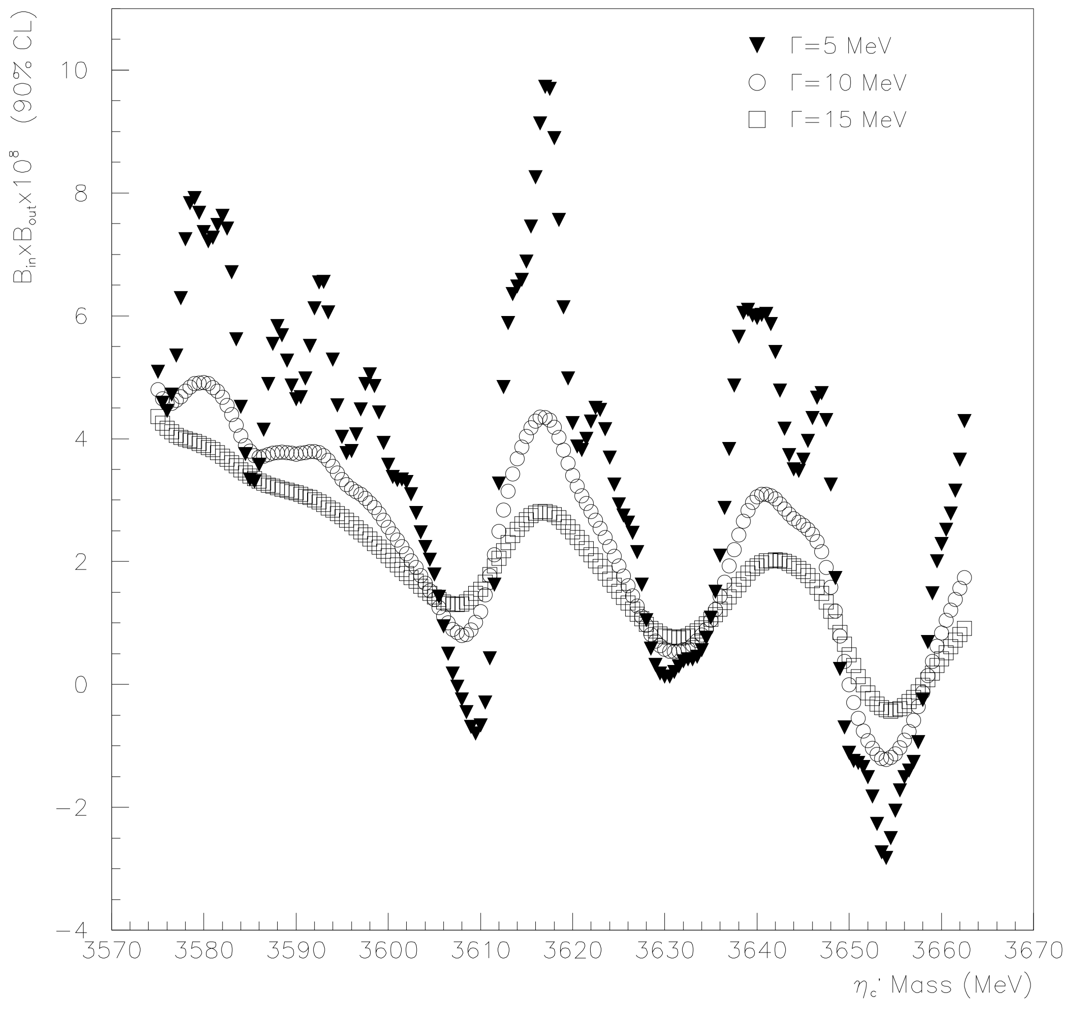

Figure G.2: The upper limits (90% confidence) calculated with the frequentist method, ignoring the physical boundary at $\sigma_{peak} = 0$, for three different values of the η_c' width.

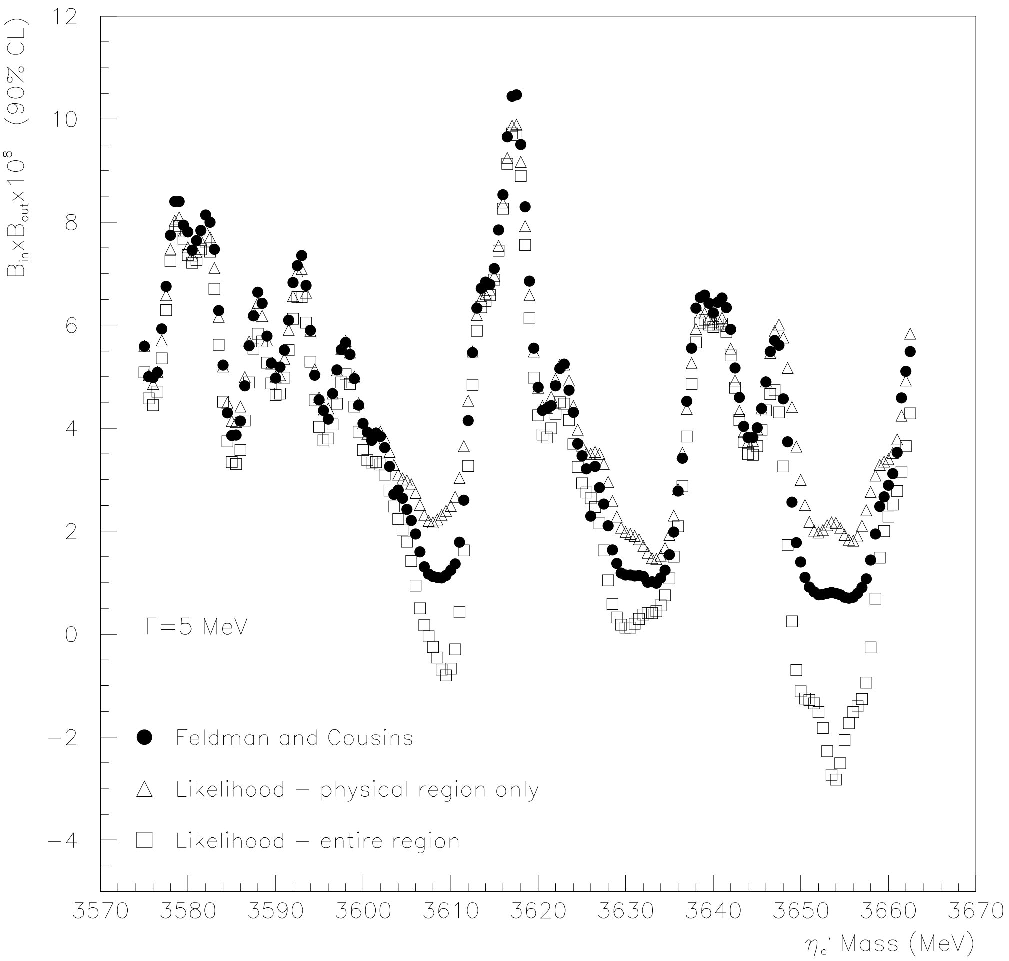

Figure G.3: The upper limit for $\Gamma(\eta_c') = 5$ MeV calculated for fixed mass values in 0.5 MeV steps, with three different methods.

Bibliography

[1] M. Acciarri et al. η_c formation in two-photon collisions at LEP. CERN-EP-99-072, submitted to Physics Letters B.

[2] M. Acciarri et al. χ_{c2} formation in two-photon collisions at LEP. *Physics Letters*, B453:83–93, 1999.

[3] K. Ackerstaff et al. Production of χ_2 mesons in photon-photon collisions at LEP. *Physics Letters*, B439:197, 1998.

[4] E.S. Ackleh and T. Barnes. Two-photon widths of singlet positronium and quarkonium with arbitrary total angular momentum. *Physical Review*, D45:232–240, 1992.

[5] H. Aihara et al. Charmonium production in photon-photon collisions. *Physical Review Letters*, 60:2355–2358, 1988.

[6] H. Albrecht et al. Determination of the radiative decay width of the η_c meson. *Physics Letters*, B338:390–396, 1994.

[7] D. Allspach et al. The variable density gas jet internal target for experiment 835 at Fermilab. *Nuclear Instruments and Methods*, A410:195–205, 1998.

[8] M. Ambrogiani et al. Results from the E835 scintillating fiber detector. *Nuclear Instruments and Methods*, A419:632–636, 1998.

[9] M. Ambrogiani et al. Study of the χ_0 state of charmonium formed in $\overline{p}p$ annihilations. *Physical Review*, 1999. submitted.

[10] Marta Ambrogiani et al. Measurements of the magnetic form factor in the time-like region at large momentum transfer. *Physical Review*, D60:032002, 1999.

[11] Thomas Applequist and H. David Politzer. Heavy quarks and e^+e^- annihilation. *Physical Review Letters*, 34:43–45, 1975.

[12] T. A. Armstrong et al. Observation of the P-wave singlet state of charmonium. *Physical Review Letters*, 69:2337–2340, 1992.

[13] T. A. Armstrong et al. Study of the angular distribution of the reaction $\overline{p}p \to \chi_2 \to J/\psi\ \gamma \to e^+e^-\ \gamma$. *Physical Review*, D48:3037–3044, 1993.

[14] T.A. Armstrong et al. Study of the χ_1 and χ_2 charmonium states formed in $\overline{p}p$ annihilations. *Nuclear Physics*, B373:35–54, 1992.

[15] T.A. Armstrong et al. Measurement of the $\gamma\gamma$ partial width of the χ_2 charmonium resonance. *Physical Review Letters*, 70:2988–2991, 1993.

[16] T.A. Armstrong et al. Study of the $\eta_c(1^1S_0)$ state of charmonium formed in $\overline{p}p$ annihilations and a search for the $\eta_c'(1^1S_0)$. *Physical Review*, D52:4839–4854, 1995.

[17] T.A. Armstrong et al. Two-body neutral final states produced in antiproton-proton annihilations at $2.911 \leq \sqrt{s} \leq 3.686$ GeV. *Physical Review*, D56:2509–2531, 1997.

[18] M Artuso et al. Measurement of the cross section for $\gamma\gamma \to \overline{p}p$. *Physical Review*, D50:5484–5490, 1994.

[19] J. J. Aubert et al. Experimental observation of a heavy particle J. *Physical Review Letters*, 33:1404–1406, 1974.

[20] J. E. Augustin et al. Discovery of a narrow resonance in e^+e^- annihilation. *Physical Review Letters*, 33:1406–1408, 1974.

[21] C. Baglin et al. Direct observation and partial width measurement of $\gamma\gamma$ decay of charmonium states. *Physics Letters*, B187:191–197, 1987.

[22] S. Bagnasco et al. FCAL II: Design and construction. E835 internal memo.

[23] S. Bagnasco et al. A straw chamber tracker for the high rate experiment 835 at the Fermilab Accumulator. *Nuclear Instruments and Methods*, A409:75–78, 1998.

[24] S. Bagnasco et al. The threshold gas cherenkov counter of charmonium experiment 835 at Fermilab. *Nuclear Instruments and Methods*, A424:304–329, 1999.

[25] J. Z. Bai et al. Study of the hadronic decays of χ_c states. 1998.

[26] Wander Baldini. private communication.

[27] Wander Baldini. *Studio del decadimento in due mesoni ϕ della stato η_c del Charmonio formato in annichilazioni protone-antiprotone e ricerca dello stato η_c'*. PhD thesis, Universita degli Studi di Ferrara, Italia, 1999.

[28] Wander Baldini and Flavio Marchetto. Charged trigger efficiency for inclusive J/ψ. E835 Internal Memo.

[29] R. M. Baltrusaitis et al. Hadronic decay of the $\eta_c(2980)$. *Physical Review*, D33:629–638, 1986.

[30] L. Bartoszek et al. The E760 lead-glass central calorimeter: design and initial test results. *Nuclear Instruments and Methods*, A301:47–60, 1991.

[31] D. Bauer et al. Study of χ_{c2} production in photon-photon collisions. *Physics Letters*, B302:345–350, 1993.

[32] V.B. Berestetskii, E.M. Lifshitz, and L.P. Pitaevskii. *Quantum Electrodynamics*. Pergamon Press, 1980. pages 336-347.

[33] D. Bisello et al. Study of the η_c decays. *Nuclear Physics*, B350:1–24, 1991.

[34] J.D. Bjorken and S.L. Glashow. Elementary particles and su(4). *Physics Letters*, 11:255, 1964.

[35] E. D. Bloom and C. Peck. Physics with the Crystal Ball detector. *Annual Review of Nuclear and Particle Science*, 33:143–197, 1983.

[36] Geoffrey Bodwin, Eric Braaten, and G. Peter Lepage. Rigorous QCD analysis of inclusive annihilation and production of heavy quarkonium. *Physical Review*, D51:1125–1171, 1995.

[37] Eric Braaten. Radiative corrections to quarkonium decays. Technical Report NUHEP-TH-94-22, Northwestern University, September 1994.

[38] Stanley J. Brodsky and Glennys R. Farrar. Scaling laws at large transverse momentum. *Physical Review Letters*, 31:1153–1156, 1973.

[39] W. Buchmüller and S.H.H. Tye. Quarkonia and quantum chromodynamics. *Physical Review*, D24:132–156, 1981.

[40] A. Buzzo et al. A silicon pad detector for E835 experiment at Fermilab. *Nuclear Instruments and Methods*, A391:443–451, 1997.

[41] Kuang-Ta Chao, Han-Wen Huang, Jing-Hua Liu, and Jian Tang. Pseudoscaler heavy quarkonium decays with both relativistic and QCD radiative corrections. *Physical Review*, D56:368–376, 1997.

[42] O.I. Dahl, T.B. Day, and F.T. Solmitz. SQUAW: Kinematic fitting program. Technical Report P-126, University of California Lawrence Radiation Laboratory, 1965.

[43] Fermilab Computing Division DART collaboration. DYC3 write-up v1.0. http://fnphyx-www.fnal.gov/elec/dyc3/dyc3nov.html.

[44] D.A. Edwards and M.J. Syphers. *An Introduction to the Physics of High Energy Accelerators*. Wiley Series in Beam Physics and Accelerator Technology. John Wiley and Sons, Inc., 1993.

[45] E. Eichten et al. Charmonium: Comparison with experiment. *Physical Review*, D21:203, 1980.

[46] Glennys R. Farrar, Ezio Maina, and Filippo Neri. QCD predictions for $\gamma\gamma$ annihilations to baryons. *Nuclear Physics*, B259:702–720, 1985.

[47] James E. Fast. *Two Photon Decays of Charmonium States Produced in Proton-Antiproton Annihilations*. PhD thesis, University of California, Irvine, 1992.

[48] Gary J. Feldman and Robert D. Cousins. Unified approach to the classical statistical analysis of small signals. *Physical Review*, 57:3873–3889, 1998.

[49] J. E. Gaiser et al. Charmonium spectroscopy from inclusive ψ' and J/ψ radiative decays. *Physical Review*, D34:711–721, 1986.

[50] Gabriele Garzoglio. Antiproton beam energy calculation for E835. E835 Internal Memo.

[51] S.L. Glashow, J. Iliopoulos, and L. Maiani. Weak interactions with lepton-hadron symmetry. *Physical Review*, D2:1285–1292, 1970.

[52] Particle Data group, D. Haidt, et al. Review of particle physics. *The European Physics Journal C*, 3, 1998.

[53] Suraj N. Gupta, James M. Johnson, and Wayne W. Repko. Relativistic two-photon and two-gluon decay rates of heavy quarkonia. *Physical Review*, D54:2075–2080, 1996.

[54] H. Hamasaki et al. Measurement of the proton-antiproton pair production from two-photon collisions at TRISTAN. *Physics Letters*, B407:185–192, 1997.

[55] M. A. Hasan et al. The Fermilab E760 forward electromagnetic calorimeter. *Nuclear Instruments and Methods*, A295:73–80, 1990.

[56] Han-Wen Huang and Kuang-Ta Chao. QCD predictions for annihilation decays of P-wave quarkonia to next-to-leading order in α_s. *Physical Review*, D54:6850–6854, 1996. errata D56 page 1821.

[57] M. Jacob and G. C. Wick. On general theory of collisions for particles with spin. *Annals of Physics*, 7:404–428, 1959.

[58] Sheng Jin and Jerry Rosen. E835 neutral trigger. E835 Internal Memo.

[59] Jason Kasper. Efficiency of the E835 neutral trigger. E835 Internal Memo, http://www-e835.fnal.gov/ jkasper/ntreff.html.

[60] P. Kroll et al. On exclusive reactions in the time-like region. *Physics Letters*, B316:546–554, 1993.

[61] Andreas S. Kronfeld and Paul B. Mackenzie. Progress in quantum chromodynamics with lattice gauge theory. *Annual Review of Nuclear and Particle Science*, 43:793–828, 1993.

[62] Waikwok Kwong, Paul B. Mackenzie, Rogerio Rosenfeld, and Jonathan L. Rosner. Quarkonium annihilation rates. *Physical Review*, D37:3210–3215, 1988.

[63] Roger A. Lee. *Radiative Decays of the ψ' to all photon final states.* PhD thesis, Stanford University, 1985. SLAC-0282.

[64] Z. P. Li, F. E. Close, and T. Barnes. Relativistic effects in gamma gamma decays of P-wave positronium and q anti-q systems. *Physical Review*, D43:2161–2170, 1991.

[65] A.D. Martin et al. Production and decay of P-wave charmonium states in $\overline{p}p$ collisions. *Physics Letters*, B147:203–206, 1984.

[66] Claus R. Münz. Two-photon decays of mesons in a relativistic quark model. *Nuclear Physics*, A609:364–376, 1996.

[67] Margherita Obertino. Studio del decadimento radiativo degli stati χ_1 e χ_2 nell'esperimento e835 a fnal e utilizzo di questi dati nella calibrazione del nuovo calorimetro elettromagnetico in avanti. Undergraduate thesis, 1997. Universita degli Studi di Torino, Italia.

[68] S. Okubo. *Physics Letters*, 5:1975, 1963.

[69] Nadia Pastrone. private communication.

[70] Claudia Patrignani. J/ψ inclusive selection using the electron weight. E835 Internal Memo.

[71] Todd Pedlar. Elements of precision: Luminosity measurement in E835. E835 Internal Memo.

[72] J. Pumplin et al. Fine-structure corrections and electromagnetic decays of charmonium. *Physical Review Letters*, 35:1538–1540, 1975.

[73] Ron Ray et al. A trigger for the Fermilab E760 lead-glass calorimeter. *Nuclear Instruments and Methods*, A307:254, 1991.

[74] J. Richman. An experimenter's guide to the helicity formalism. Technical Report CALT-68-1148, California Institute of Technology, 1984.

[75] Vladimir Savinov and Roger Fulton. Measurements of the two photon widths of the charmonium states η_c, χ_0, and χ_2. 1995. hep-ex/9507006.

[76] H.J. Schnitzer. P states of charmonium and the forces that confine quarks. *Physical Review Letters*, 35:1540–1543, 1975.

[77] V. Shelkov et al. Measurement of two photon production of the χ_{c2}. *Physical Review*, D50:4265–4271, 1994.

[78] S. Trokenheim et al. A $\overline{p}p$ luminosity monitor for Fermilab experiment E760. *Nuclear Instruments and Methods*, A355:308–319, 1995.